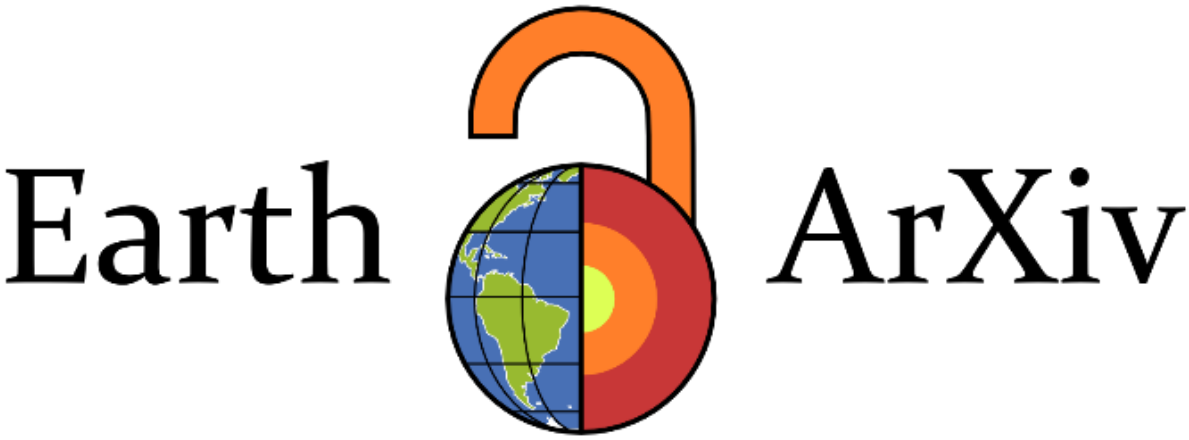

# Two decades of kilometer-scale daily $PM_{2.5}$ from satellite observations and machine learning reveal geographically diverging exposure in Ghana

Abhishek Anand[a*], Joe A. Amooli[a,b], Selina Amoah[c], Esi Nerquaye Tetteh[c], Nana Ama Browne Klutse[c], Clement Mensah Ackaah[c], Benjamin Essien[c], Kingsley Mawuli Amegah[c], Daniel M. Westervelt[a,b]

[a]Lamont-Doherty Earth Observatory, Columbia University, Palisades, NY, USA

[b]Department of Earth and Environmental Sciences, Columbia University, New York, NY, USA

[c]Ghana Environmental Protection Authority, Accra, Ghana

*Corresponding author: Abhishek Anand (abhishek.anand@columbia.edu)

ORCID ID: https://orcid.org/0000-0001-8263-192X

## Abstract

Exposure to fine particulate matter ($PM_{2.5}$) is a major contributor to global burden of disease, yet air quality data remain sparse in many low- and middle-income countries, limiting nationwide monitoring and effective policy development. We address this gap by developing a high-resolution gridded (1 km × 1 km) dataset for daily surface $PM_{2.5}$ concentrations in Ghana from 2005 to 2025 by training multiple machine learning (ML) models built on ground-based monitoring, satellite observations, and reanalysis products for atmospheric composition and meteorological parameters. Estimates from these models were evaluated with measurements from reference-grade monitors and a large network of calibrated low-cost sensors deployed across Ghana. XGBoost showed the strongest performance among all ML algorithms and best captured spatial and temporal variability in $PM_{2.5}$ levels. SHapley Additive exPlanations (SHAP) analysis for model predictors indicates that both meteorological variables and aerosol optical properties are key contributors to model performance. The long-term gridded $PM_{2.5}$ dataset reveals a unique north-south exposure disparity in Ghana, with northern regions of the country experiencing substantially higher $PM_{2.5}$ concentrations compared to the South, that may be widening over the 21-year period by over 0.2 $\mu g\ m^{-3}\ yr^{-1}$. This study provides the first long-term high-resolution $PM_{2.5}$ exposure levels for Ghana and presents a scalable framework for generating air quality information in data-sparse regions to support air pollution relevant health impact assessment and evidence-based mitigation policies.



## Keywords

Air quality, fine particulate matter ($PM_{2.5}$), satellite-remote sensing, low-cost sensors, geospatial machine learning, sub-Saharan Africa, exposure disparity

# 1 INTRODUCTION

Air pollution is the second leading risk factor of deaths globally after high blood pressure (Health Effects Institute, 2024). In 2021, exposure to air pollution was associated with around 1.1 million premature annual deaths in Africa (Amooli et al., 2025; Fisher et al., 2021). This risk is dominated by exposure to fine particulate matter ($PM_{2.5}$), which is associated with ischemic heart disease, stroke, respiratory and neurodegenerative diseases (Hayes et al., 2020; Shi et al., 2020). This burden is particularly severe in low- and middle-income countries (LMICs), including many African nations, where ambient $PM_{2.5}$ concentrations frequently exceed World Health Organization (WHO) guidelines. However, long-term air quality observations in these regions remain sparse, constraining accurate exposure assessment, epidemiological analysis, and consequently, evidence-based mitigation policies.

The high capital cost and technical skills needed for establishing and operating a network of regulatory instruments present a significant barrier for continuous air quality monitoring. African countries contain an average of only ~3 sensors per 100 million people compared with 379 in Europe (Gualtieri et al., 2024). Beta attenuation monitors (BAMs) deployed by the US Department of State at the US Embassies have been one of the major sources of reliable open access $PM_{2.5}$ measurements around the world. Multi-year hourly $PM_{2.5}$ levels from these monitors have provided important insights into $PM_{2.5}$ trends across the African continent, including the first long-term observations in some countries (Anand et al., 2024; Li et al., 2024). However, these deployments are typically limited to just one to two monitors per country capital and hence are unable to capture spatial variability of $PM_{2.5}$ even within the cities. Recent efforts to address these monitoring gaps include using networks of consumer-grade air sensors for city-scale monitoring of particulate matter through fixed-duration campaigns (Owusu-Tawiah et al., 2025; Raheja et al., 2022; Westervelt et al., 2023). However, these sensors are primarily suited for point-location measurements and therefore deploying dense networks over large geographic regions remains prohibitively expensive, limiting their use for long-term nationwide air quality monitoring.

Satellite-based air quality products have emerged as a promising solution for long-term spatiotemporal monitoring in data-sparse regions. These products often provide near-global spatial coverage, with several satellite instruments offering multi-decadal records of daily observations for air pollution parameters extending back to the early 2000s. Aerosol optical depth (AOD) retrieved from satellites has been widely used for estimating ground level $PM_{2.5}$. Liu et al. (2004) used a scaling factor calculated as the ratio of surface $PM_{2.5}$ mass concentration to satellite-measured column-integrated AOD to estimate spatial $PM_{2.5}$ concentrations across the United States (Liu et al., 2004). Other studies derived $PM_{2.5}$-to-AOD ratios simulated by the GEOS-Chem chemical transport model and applied to satellite-based AOD to generate global maps of annual (Hammer et al., 2020; Van Donkelaar et al., 2016) and monthly (Van Donkelaar et al., 2021) $PM_{2.5}$ concentrations. However, the relationship between $PM_{2.5}$ and AOD varies substantially across the globe, largely due to geographical differences in vertical distribution of aerosol loading (Van Donkelaar et al., 2006). As a result, the accuracy of these estimates heavily relies on the availability of reliable ground-based measurements for constraining models and capturing these regional variations between columnar AOD and surface $PM_{2.5}$. Several studies have therefore emphasized the urgent need for expanding surface monitoring infrastructure in the Global South, particularly in Africa, to improve satellite-based $PM_{2.5}$ estimates (Anand et al., 2024; Bachwenkizi et al., 2021;

Di et al., 2016; Hammer et al., 2020; Philip et al., 2014; Van Donkelaar et al., 2016; Vohra et al., 2021; Weagle et al., 2018).

Recent advances in African air quality monitoring provide an opportunity for regionally-refined satellite-based surface $PM_{2.5}$ datasets trained and tested on local measurements. Zhang et al. (2021) used satellite AOD, meteorological features, land use variables and socioeconomic parameters to develop daily 1 km × 1 km $PM_{2.5}$ concentration maps for 2014–2018 in South Africa, validated by measurements from a network of 20 surface monitors in South Africa. Amooli et al. (2024) developed an AOD to $PM_{2.5}$ conversion framework to generate 1 km × 1 km spatial $PM_{2.5}$ for Ouagadougou, the capital of Burkina Faso, using surface measurements at the US Embassy in the capital. Furthermore, the spatial resolutions of existing global $PM_{2.5}$ products based on Modern-Era Retrospective analysis for Research and Applications, Version 2 (MERRA-2) data remain too coarse (>50 km) to capture intra-city $PM_{2.5}$ variations across most cities in Africa (Sayeed et al., 2022).

Gaseous pollutants, such as nitrogen dioxide ($NO_2$), sulfur dioxide ($SO_2$) and volatile organic compounds, act as precursors to $PM_{2.5}$ formation (Pye et al., 2022) and can help improve the accuracy of surface-level $PM_{2.5}$ estimates (Zheng et al., 2023). In this study, we propose a multi-model machine learning approach to estimate 21 years (2005–2025) of daily $PM_{2.5}$ concentrations for Ghana at 1 km × 1 km spatial resolution. In addition to AOD, this modeling approach incorporates satellite-derived information on gaseous precursors to $PM_{2.5}$ formation and other aerosol indicators. We also include meteorological parameters to account for weather-induced variability in $PM_{2.5}$ concentrations. A large network of ~98 well-calibrated surface $PM_{2.5}$ monitors (~275 monitors per 100 million people) were deployed across Ghana, and the measurements were used to capture the geographic distribution of $PM_{2.5}$ concentration in Ghana. These additions collectively mitigate large uncertainties in satellite-derived surface $PM_{2.5}$, conventionally observed due to a limited representation of input variables as well as from the lack of surface measurements of $PM_{2.5}$ in regions like sub-Saharan Africa. We further augment missing $PM_{2.5}$ information due to occasional unavailability of satellite-derived predictors by developing a MERRA-2-based $PM_{2.5}$ model. To our knowledge, this is among the first efforts to generate long-term gap-filled $PM_{2.5}$ estimates at 1 km × 1 km grid resolution trained and evaluated using robust local observations in Africa, while also providing insights into spatiotemporal trends of $PM_{2.5}$ across Ghana.

## 2 MATERIALS AND METHODS

### 2.1 Study area

Ghana is located in West Africa and lies between latitudes ~ 4.5°N and 11.5°N and longitudes 3.5°W and 1.5°E, covering an area of about 238,535 $km^2$. The country is characterized by diverse geographic features, including coastal plains along the Gulf of Guinea, forested regions in the south, and savanna landscapes in the north. Major urban centers include Accra, Kumasi, Tamale, Sekondi-Takoradi, Cape Coast, Sunyani and the industrial port of Tema, representing important population and economic hubs with diverse emission characteristics.

Ghana has a typical tropical climate with distinct wet and dry seasons. Southern Ghana typically exhibits bimodal rainfall patterns due to its proximity to the Gulf of Guinea and the progression of the Intertropical Convergence Zone (ITCZ), with major and minor wet seasons occurring between

April–June and September–October, respectively. In contrast, Northern Ghana has a unimodal wet season between April and October, peaking during August–September. Ghana experiences a major meteorological phenomenon during mid-November to mid-March, known as the Harmattan, which overlaps with the dry season. During this period, dry northeasterly winds transport large amounts of mineral dust from the Sahara Desert across West African countries, including Ghana. This results in extremely high concentrations of particulate matter across the country, leading to severely degraded air quality and reduced visibility, with impacts more pronounced in northern Ghana than in the south.

## 2.2 Surface $PM_{2.5}$ measurements

Ground-level measurements for $PM_{2.5}$ were collected from a network of 98 ground sensors spread across Ghana. The network consisted of 96 low-cost sensors, including 10 Airnote v2.0 (Blues Inc., Boston, MA), 21 Clarity Node-S Generation II (Clarity Movement Co., Berkeley, CA), 15 PurpleAir PA-II SD monitors (PurpleAir Inc., Draper, UT), 6 MODULAIR™ (QuantAQ Inc., Somerville, MA), and 44 MODULAIR$^{TM}$-PM monitors (QuantAQ Inc., Somerville, MA). $PM_{2.5}$ measurements from two Beta Attenuation Monitors (BAMs; BAM-1020, Met One Instruments Inc., Grants Pass, Oregon) were also obtained, one deployed in Techiman and another located at the U.S. Embassy in Accra, Ghana. BAM is certified by the U.S. EPA as a Federal Equivalent Method and hence served as the reference monitor for calibrating raw $PM_{2.5}$ measurements from the low-cost sensors in the network. Table S1 of the Supporting Materials details the technical specifications of each monitor type and Fig. S1 illustrates the deployment locations of all sensors used in this study. $PM_{2.5}$ measurements collected from this sensor network between August 2018 and October 2024 were used as ground-truth for model development. Fig. S2 shows deployment periods of each surface instrument included in the study.

These sensors were strategically deployed across Ghana, with a significantly higher density in urban areas where population is largely concentrated, to capture high spatial variability in $PM_{2.5}$ concentrations arising from diverse sources, including vehicular emissions, open burning, cooking activities and industrial emissions. Air quality monitors were also deployed in suburban and rural regions of Ghana, where local air quality is strongly influenced by emissions from solid biomass fuel use for cooking, agricultural residue burning and dust from unpaved roads. This sensor network architecture helps inform the model about the spatial distribution of $PM_{2.5}$ in Ghana during the Harmattan period by using measurements from northern, middle and southern belts of Ghana. Fig. S1 depicts the locations of every monitor against a population count map retrieved from the LandScan project at Oak Ridge National Laboratory (Lebakula et al., 2025). Additional deployment details are available in Tables S2–S3.

Raw $PM_{2.5}$ measurements from each low-cost sensor, available at sub-hourly time resolution, were aggregated to hourly concentrations and subjected to custom-designed calibration models unique to each sensor type to derive QA/QC-corrected exposure levels. The calibration procedures are further explained in Supplementary Text S1.

## 2.3 Satellite and reanalysis datasets

### 2.3.1 MODIS Level 2 aerosol optical depth

Moderate Resolution Imaging Spectroradiometer (MODIS) is an optical sensor aboard NASA's sun-synchronous low-Earth orbit (LEO) Terra (launched in 1999) and Aqua (launched in 2002) satellites, passing over the equator at 10:30 am and 1:30 pm local time, respectively. In this study, we used MODIS AOD at 550 nm derived through the Multi-Angle Implementation of Atmospheric Correction (MAIAC) algorithm (Lyapustin et al., 2018), specifically from the MCD19A2 product. It is a Level 2 (L2) product, produced by combining measurements from MODIS instruments aboard both Aqua and Terra satellites, that provides daily global coverage in multiple spectral bands and has been widely used for monitoring land, ocean, and atmospheric parameters for over two decades. The MAIAC algorithm combines time series analysis and multi-angle radiative transfer modeling to produce atmospherically corrected surface reflectance and high-quality AOD retrievals at a 1 km × 1 km spatial resolution beginning from February 2000. The enhanced spatial resolution, improved cloud screening, and robust performance over complex surfaces make MCD19A2 particularly valuable for estimating ground-level $PM_{2.5}$ in data-sparse regions, such as Ghana.

The AOD from the MCD19A2 product is available in sinusoidal projection tiles. Tiles h17v07, h17v08, h18v07, and h18v08 were combined to gather AOD information for Ghana. For each day, the *Optical_Depth_055* product and corresponding *AOD_QA* layers were extracted and used for further analysis. The *AOD_QA* layer contains 16-bit unsigned integers, with bits 8-11 embedding the QA information. QA-based filtering was applied to retain *Optical_Depth_055* retrievals with QA flags {0000, 0011, 1011}, classified as best-quality observations over land for research applications, while excluding pixels affected by cloud contamination, snow, sun glint, coastline artifacts, or missing retrieval conditions, to ensure AOD retrievals considered suitable for scientific analysis in air quality applications. The AOD values were then calibrated using the scale factor and offset from the product attributes to obtain physically meaningful retrievals. All valid orbit-level retrievals within each day were aggregated for each cell, and measurements for duplicate grid cells were averaged to generate daily mean AOD values.

### 2.3.2 OMI Level 2 air quality products

Ozone Monitoring Instrument (OMI) has been continuously measuring air quality parameters onboard NASA's Aura spacecraft since July 2004. Similar to Terra and Aqua, Aura is a sun-synchronous LEO satellite and crosses the equator at 1:45 PM local time. We used OMI L2 Collection 3 measurements for ultraviolet aerosol index (UVAI) and column number density for ozone ($O_3$), tropospheric $NO_2$, $SO_2$ and formaldehyde (HCHO). These air quality features are available at a spatial resolution of 13 km × 24 km. UVAI is a unitless quantity derived from top-of-atmosphere radiances at 354 nm and 388 nm, which allows distinction between UV-absorbing aerosols (e.g., dust, biomass burning smoke, haze) and non-absorbing particles such as clouds (Torres et al., 2020). HCHO and $NO_2$ are measured in molecules $cm^{-2}$, whereas $O_3$ and $SO_2$ are expressed in Dobson Unit (DU), where 1 DU = $2.69 \times 10^{16}$ molecules $cm^{-2}$. The Level 2 OMI data occasionally contain multiple retrievals for a given grid cell within a single day due to multiple orbital overpasses. These intra-day measurements were aggregated to generate a single daily-averaged retrieval for each grid cell.

Quality control was applied individually to each OMI product to account for differences in retrieval sensitivity, signal strength, and known instrumental artifacts. For the UV Aerosol Index, pixels were retained only when *CloudFraction* ≤ 0.3, *SolarZenithAngle* ≤ 75°, and *XTrackQualityFlag*s = 0. The *XTrackQualityFlags* filter is particularly useful in excluding cross-track (row) anomalies and geometries associated with increased radiative transfer uncertainty. HCHO is more sensitive to cloud contamination and retrieval noise, and hence strict filtering criteria were applied by requiring *AMFCloudFraction* ≤ 0.3, *SolarZenithAngle* ≤ 75°, *XTrackQualityFlags* = 0, and *MainDataQualityFlag* = 0 to ensure successful spectral fitting and reliable air mass factor calculations. Total column ozone, a comparatively high signal-to-noise product, was screened using *RadiativeCloudFraction* ≤ 0.3, *SolarZenithAngle* ≤ 85°, and *QualityFlags* ≤ 1, thereby retaining only good or glint-corrected retrievals. For tropospheric $NO_2$, pixels were restricted to *CloudFraction* ≤ 0.3, *SolarZenithAngle* ≤ 75°, and *VcdQualityFlags* = 0 to remove cloud-affected scenes and retrievals with known fitting or cross-track issues. $SO_2$ retrievals, which are particularly sensitive to instrumental artifacts and weak signal conditions, were subjected to the most stringent screening: *CloudRadiationFraction* ≤ 0.3, *SolarZenithAngle* ≤ 65°, *Flag_RowAnomaly* ≠ 1, *Flag_SAA* ≠ 1, and *AlgorithmFlag_SnowIce* ≠ 2, excluding scenes affected by the OMI row anomaly, South Atlantic Anomaly interference, or uncertain cloud detection over snow and ice. The *ColumnAmountSO2_PBL* dataset from the OMI L2 $SO_2$ product was specifically selected because it represents $SO_2$ VCD within the planetary boundary layer and is commonly used as an indicator of anthropogenic $SO_2$ emissions (Li et al., 2013). These species-specific filtering criteria are consistent with OMI Collection 3 product documentation and widely adopted validation studies, ensuring that only physically meaningful and robust retrievals were included in the analysis. More details on quality screening of OMI and other satellite-derived products are summarized in Table S4.

### 2.3.3 TROPOMI Level 2 air quality features

TROPOspheric Monitoring Instrument (TROPOMI) is onboard the Copernicus Sentinel-5 Precursor (S5P), another sun-synchronous LEO satellite that passes over the equator at 1:30 PM local time and was launched in October 2017. We used L2 Version 2 UVAI (unitless) and column number density measurements (in mol $m^{-2}$) for $O_3$, tropospheric $NO_2$, $SO_2$, and tropospheric HCHO, which are similar to the parameters used from OMI and are consistently available from May 7, 2018. In addition, carbon monoxide (CO) retrievals from TROPOMI were also used as it is one of the primary combustion products from any combustion activity and hence a strong tracer for combustion-related emission sources in Ghana (Griffin et al., 2024). The spatial resolution for $O_3$, $NO_2$, $SO_2$, HCHO and UVAI products was 7 km × 3.5 km (across × along track) until August 5, 2019 and improved to 5.5 km × 3.5 km from August 6, 2019 onward due to reduced across-track detector binning. This corresponds to approximately a 16-fold improvement in spatial resolution compared to OMI. In contrast, CO retrievals from the short wavelength infrared channel were provided at 7 km × 7 km (across × along track) prior to August 6, 2019 and at 7 km × 5.5 km thereafter. TROPOMI provides tropospheric column density for HCHO which differs from Level 2 total column HCHO density retrievals from OMI. In most cases, particularly over polluted areas, the amount of HCHO in the stratosphere is negligible and almost all HCHO resides in the troposphere due to its short lifetime (Ayazpour et al., 2025; De Smedt et al., 2008). Therefore, tropospheric HCHO is typically approximated as total column HCHO. The reprocessed dataset (RPRO) covers April 30, 2018 until July 25, 2022 and is fully compatible with the current offline dataset (OFFL), which covers July 26, 2022 onwards. TROPOMI provides UVAI at three

wavelength pairs: 335/367 nm, 340/380 nm, and 354/388 nm but only UVAI calculated at 354 nm and 388 nm wavelengths was used as it is an indicator of dust and biomass burning smoke (Torres et al., 2020). Following the quality screening criteria provided in the official product documentation, only pixels with *qa_value* ≥ 0.5 were retained for each TROPOMI product to ensure high-quality retrievals and exclude observations affected by clouds or snow/ice (Van Geffen et al., 2022).

### 2.3.4 ERA5-Land reanalysis hourly dataset

ERA5-Land is a fifth-generation reanalysis of global climate dataset from European Centre for Medium-Range Weather Forecasts (ECMWF), covering the period 1940-present at hourly temporal resolution (Muñoz-Sabater et al., 2021). The dataset is available at 0.1º × 0.1º grid resolution for dewpoint temperature at 2 m above Earth's surface ($T_d$), surface temperature at 2 m above surface (T), total precipitation (TP), and wind velocities at 10 m above the ground in east-west direction (U) and north-south direction (V). These variables have proven to be important meteorological drivers of ambient pollution dynamics (Westervelt et al., 2025). Surface temperatures and relative humidity are derived at 2 m whereas wind speeds at 10 m above ground, following the guidelines from World Meteorological Organization for surface measurements of meteorological variables (World Meteorological Organization (WMO), 2008). Relative humidity (RH, in %) is not inherently available from the ERA5-Land dataset and hence was calculated using the Magnus-Tetens equation (Amooli et al., 2024) as:

$$RH(\%) = 100 \times \exp\left(\frac{17.625 * T_d}{243.12 + T_d} - \frac{17.625 * T_{2m}}{243.12 + T_{2m}}\right) \ldots (1)$$

where *RH* is the relative humidity (in %) at 2 m above ground, $T_d$ and $T_{2m}$ are 2 m ambient and dewpoint temperatures (in ºC) from ERA5-Land dataset.

### 2.3.5 MERRA-2 reanalysis product

MERRA-2 reanalysis dataset, developed by NASA's Global Modeling and Assimilation Office (GMAO), is a global atmospheric reanalysis that integrates the GEOS-5 Earth system model with a three-dimensional variational data assimilation system. MERRA-2 assimilates a comprehensive suite of meteorological observations, including satellite radiances, radiosondes, aircraft, and surface measurements, and uniquely incorporates space-based AOD observations, enabling improved representation of aerosol variability and aerosol–radiation interactions. The reanalysis is produced at a horizontal resolution of 0.5° × 0.625° with 72 vertical levels extending to 0.01 hPa and provides hourly to monthly-averaged meteorological and aerosol diagnostics from 1980 to present. In this study, we used MERRA-2 aerosol mass and optical properties from aerosol diagnostics product, M2T1NXAER, as predictors in the model development framework. The features include hourly total extinction aerosol optical thickness at 550 nm (TOTEXTTAU) and surface concentrations of black carbon (BCSMASS), organic carbon (OCSMASS), sulfate (SO4SMASS), sulfur dioxide (SO2SMASS), fine-mode dust (DUSMASS25) and fine-mode sea salt (SSSMASS25). These variables collectively represent major anthropogenic and natural aerosol components and provide physically consistent, spatially complete information on aerosol loading and composition.

## 2.4 Data preprocessing

### 2.4.1 Regridding input features

The ERA5-Land and MERRA-2 datasets are available in Coordinated Universal Time (UTC), which aligns with the local time in Ghana. Hourly datasets were aggregated to daily resolution as 24-hour averages for each feature retrieved from ERA5-Land and MERRA-2, except the ERA5 total precipitation product, which reports cumulative hourly values since the start of the day. The 00:00 UTC precipitation value was used as the total precipitation for the previous day.

ERA5-Land dataset often suffers from missing parameter retrievals for coastal grids containing even a small ocean fraction. This presents a limitation in deriving $PM_{2.5}$ for coastal locations, particularly for Ghana, where major urban centers, such as Accra, Tema, and Sekondi, are located along the coastline. Missing feature values in these coastal grid cells were imputed using nearest-neighbor spatial interpolation from adjacent land grid cells.

The QA-corrected daily AOD from the MCD19A2 product was transformed from the sinusoidal to the World Geodetic System 1984 (WGS84; EPSG:4326) projection using the tile-specific projection information embedded in each file. The daily AOD fields were further regridded to a spatial resolution of 0.01° × 0.01° over Ghana, covering a rectangular domain bounded by 4.5ºN to 11.5ºN and 3.5ºW to 1.5ºE, using area-weighted averaging.

To harmonize the spatial resolution of all input datasets with the 1 km MODIS MAIAC grid, we performed downscaling of coarser-resolution input features. The ERA5 meteorological variables (0.1º resolution) and MERRA-2 features were downscaled to 0.01º grid resolution (~1 km) using bilinear interpolation, which provides a smooth transition between grid points while preserving spatial gradients. Satellite-derived atmospheric composition variables from OMI and TROPOMI were regridded to a spatial resolution of 0.01° × 0.01° using area-weighted averaging. This method accounts for the varying overlap between original satellite pixels and the target 1 km grid cells, ensuring that spatial integrity is maintained during the resampling process. These approaches enable the integration of diverse atmospheric and environmental data at a common high-resolution scale, suitable for fine-scale air pollution modeling.

### 2.4.2 Data preparation

Since surface monitors provide $PM_{2.5}$ measurements at discrete geographic locations, the training dataset was constructed by spatially matching $PM_{2.5}$ observations from each monitor with predictor values from the 0.01° × 0.01° grid cells containing the monitor. For each sensor-day observation, the corresponding daily values of MODIS AOD, OMI/TROPOMI gas-phase retrievals, ERA5-Land meteorological parameters, and MERRA-2 aerosol diagnostics were extracted from corresponding grid cells. This colocation was performed for each observation date across the full sensor deployment period (August 2018 – October 2024), yielding a tabular dataset with each row representing a unique sensor-day pair and contains the measured $PM_{2.5}$ concentration alongside the corresponding values of all predictor variables. Sensor-day records for which any satellite-derived predictor was unavailable (e.g., due to cloud cover or instrument downtime) were excluded from the training set for the respective model. Collinearity among predictors was not explicitly removed, as the machine learning algorithms used in this study are generally robust to correlated

inputs. Retaining correlated variables allows the models to capture potentially informative relationships among atmospheric and satellite-derived features without imposing arbitrary feature exclusion.

### 2.4.3 Cyclic features

$PM_{2.5}$ concentrations in Ghana exhibit pronounced seasonal variability, particularly during the Harmattan period, when long-range transport of Saharan dust substantially elevates particulate levels. To account for this cyclical behavior and enable the model to capture recurring seasonal patterns in $PM_{2.5}$ variability, the cosine and sine transformation of the day of year (DOY) for a year of N days was computed below and were included as predictor variables.

$$DOY_{COS} = Cosine\left(\frac{2*\pi*DOY}{N}\right) \ldots (2)$$

$$DOY_{SIN} = Sine\left(\frac{2*\pi*DOY}{N}\right) \ldots (3)$$

### 2.4.4 Standardization

Prior to model training, all continuous predictor variables were standardized using z-score normalization by subtracting the training set mean ($\mu$) and dividing by the standard deviation ($\sigma$) as $(x - \mu)/\sigma$, which is required for gradient-based algorithms, including multi-layer perceptron (MLP), least absolute shrinkage and selection operator (LASSO), and support vector machine (SVM), to ensure consistent regularization-based penalties. Tree-based models, including random forest (RF) and XGBoost, are invariant to monotonic feature transformations and thus did not require scaling, but the same preprocessed dataset was used for all algorithms to ensure a consistent comparison. Fill values and physically implausible retrievals were replaced with NaN and excluded from training prior to normalization.

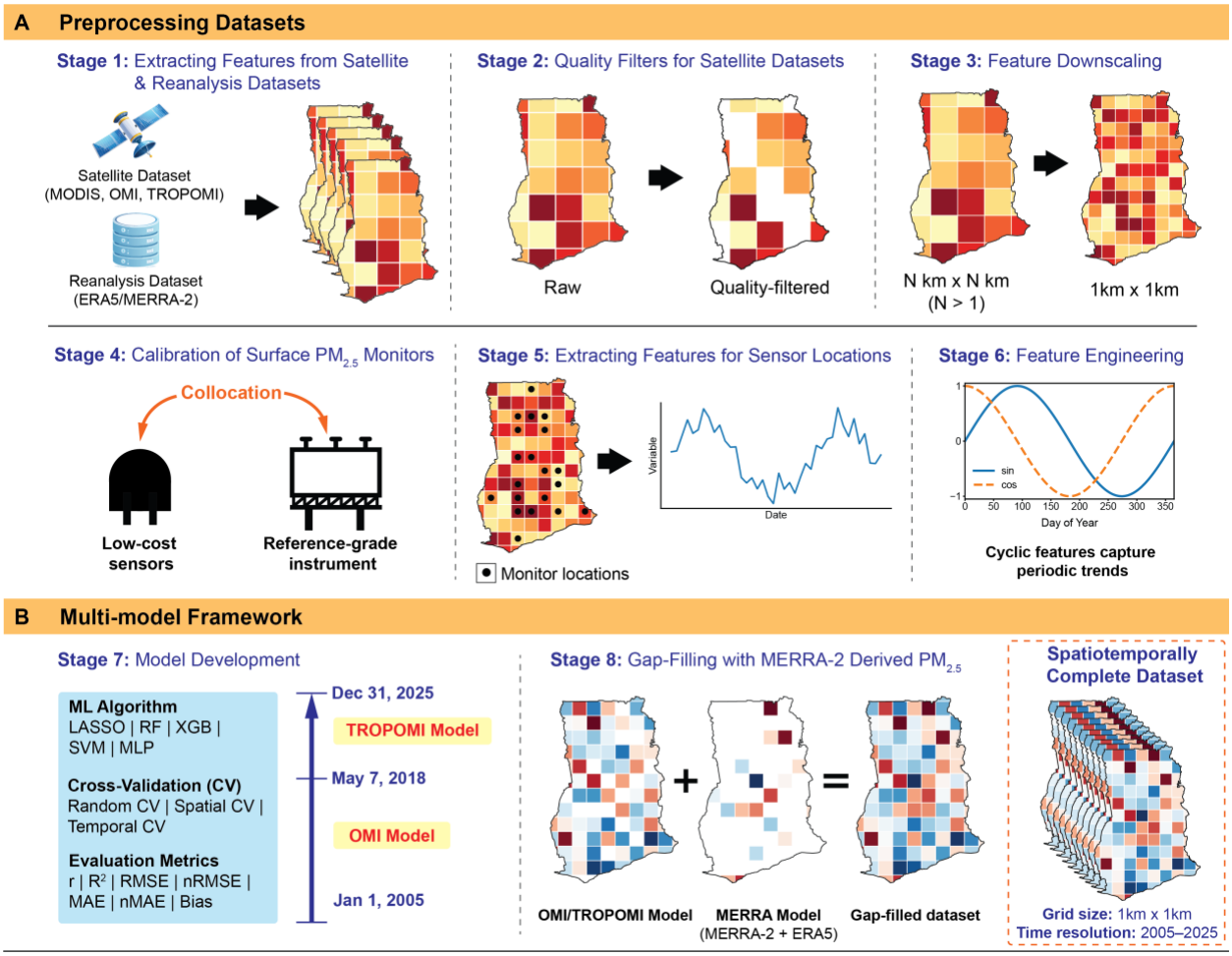


**Fig. 1. Overview of the modeling framework for generating high-resolution $PM_{2.5}$ estimates.** The workflow demonstrates a three-model framework which developed machine learning algorithms by integrating satellite and reanalysis products with ground-based $PM_{2.5}$ measurements through preprocessing, feature engineering, and model training to produce continuous spatiotemporal $PM_{2.5}$ concentrations at 1 km × 1 km spatial resolution from 2005–2025. Air quality input predictors were obtained from satellite instruments, along with meteorological variables from ERA5. Satellite observations were quality screened and spatially harmonized prior to model development. Ground-based $PM_{2.5}$ measurements from reference monitors and calibrated low-cost sensors were used for training and validation of multiple machine learning algorithms under random, spatial, and temporal cross-validation schemes. Two satellite-based models were developed using predictors derived from OMI (OMI Model; January 1, 2005–May 6, 2018) and TROPOMI (TROPOMI Model; May 7, 2018–December 31, 2025). Missing satellite retrievals were supplemented using a gap-filling model (MERRA Model) developed using aerosol diagnostics dataset from MERRA-2 and meteorological variables from ERA5 to produce a spatiotemporally complete daily $PM_{2.5}$ dataset between 2005–2025 across Ghana.

## 2.5 Development of a spatiotemporal $PM_{2.5}$ model

We developed a multi-model framework by integrating satellite retrievals, reanalysis products, and ground-based measurements to ensure complete coverage of $PM_{2.5}$ for the entire geographical

region of Ghana and all days from 2005 to 2025. The framework consists of three complementary machine learning models with varying input features: TROPOMI model, OMI model and MERRA-2 model. All three models incorporate ground-level $PM_{2.5}$ measurements and meteorological variables from ERA5 dataset. TROPOMI model derives $PM_{2.5}$ beginning May 7, 2018 by integrating AOD from MODIS and air quality parameters (UVAI, CO, HCHO, $NO_2$, $O_3$, and $SO_2$) from TROPOMI instrument. OMI model also uses MODIS AOD but utilizes only UVAI, HCHO, $NO_2$, $O_3$, and $SO_2$ retrievals from OMI to estimate $PM_{2.5}$ from January 1, 2005 to May 6, 2018, before TROPOMI measurements became available.

Since both models rely heavily on satellite-derived observations, occasional cloud cover and instrument-specific limitations, including row anomalies in OMI(Torres et al., 2018) and retrieval uncertainties in TROPOMI (Veefkind et al., 2012), make it difficult to obtain high-quality satellite retrievals, leading to missing $PM_{2.5}$ estimates from OMI and TROPOMI models in certain regions and time periods. The MERRA-2-based model was developed to mitigate these $PM_{2.5}$ gaps. It utilizes air quality features from MERRA-2 reanalysis dataset, including BCSMASS, OCSMASS, SO4SMASS, SO2SMASS, DUSMASS25, SSSMASS25, and TOTEXTTAU. Although MERRA-2 also contains meteorological variables, those features were rather extracted from the ERA5-Land reanalysis dataset due to availability of hourly variables at approximately 31 times finer grid sizes ($0.1^o \times 0.1^o$) which is more suitable for developing a high spatial resolution $PM_{2.5}$ model. The MERRA-2-based model therefore serves as a fallback framework for periods or locations where satellite retrievals from OMI or TROPOMI are unavailable, ensuring continuous spatiotemporal $PM_{2.5}$ coverage across Ghana from 2005–2025.

For each model type, geospatial machine learning algorithms, including LASSO, SVM, RF, XGBoost and MLP, were developed and evaluated to determine the optimal modeling approach for estimating daily $PM_{2.5}$ concentrations. Model performance was evaluated using cross-validation to ensure robust assessment and reduce the risk of overfitting. The probability distribution of $PM_{2.5}$ measurements from surface monitors exhibits a right-skewed distribution with a long tail towards higher concentrations (Fig. S4). Therefore, the dataset was first divided into training (80%) and testing (20%) subsets using stratified sampling based on $PM_{2.5}$ concentration ranges. $PM_{2.5}$ values were grouped into discrete bins using thresholds of 35, 60, 100, 150, and 200 $\mu g\ m^{-3}$, to ensure that low, moderate, and high pollution conditions were proportionally represented in both subsets. This stratification improves model robustness by ensuring representation of episodic high-PM events, which is particularly important in geographical regions such as Ghana where the Harmattan season periodically leads to elevated particulate matter levels. Model hyperparameters were optimized using repeated five-fold cross-validation (5 folds repeated 5 times) applied to the training dataset, with the mean root mean square error (RMSE) across validation folds used as the loss function to identify the best-performing model configuration with minimal risk of overfitting. Model performance was assessed using r, $R^2$, RMSE, MAE and mean bias. Mean-normalized RMSE (nRMSE) and MAE (nMAE) were computed by dividing the errors by the mean observed $PM_{2.5}$ concentrations, enabling comparison of model performance across environments with varying pollution levels.

After determining the optimal hyperparameters, the model configuration was fixed and further evaluated using structured cross-validation to assess its ability to generalize across Ghana and time. Spatial and temporal cross-validation were used to reduce the influence of spatial and temporal autocorrelation and provide a more realistic estimate of model generalization.

Spatial cross-validation was conducted using a leave-one-location-out cross-validation approach, where data from one monitoring location were withheld as the test set while the model was trained using data from all remaining locations. This procedure was repeated until each location had served once as the test set. Locations with limited data coverage (Somanya and Sekondi) were excluded from the spatial cross-validation analysis because the sparse observations at these sites were insufficient for robust evaluation of model performance. This approach quantifies the model's ability to generalize to regions of Ghana where surface measurements are not available.

Temporal cross-validation was performed using the leave-one-year-out cross-validation approach, where observations from a single year were excluded from training and used exclusively for testing for each year from 2018 to 2024 of the surface measurement campaign. In each fold, the model was retrained using the fixed hyperparameters and evaluated on the held-out subset. This approach assesses the model's ability to generalize across interannual variability in meteorology, emissions, and episodic pollution events, increasing confidence in the robustness of $PM_{2.5}$ estimates for periods outside the training data. This step is particularly important because model training is primarily based on observations from 2018–2024, while $PM_{2.5}$ concentrations are estimated retrospectively back to 2005, requiring the model to perform reliably during time periods not directly represented in the training dataset.

The optimized model from each model type (TROPOMI, OMI, and MERRA) was subsequently applied to the complete gridded predictor dataset to generate spatially continuous daily $PM_{2.5}$ estimates across the spatiotemporal study domain. For each grid cell $s$ and day $t$, predicted concentrations were obtained as $\widehat{PM_{2.5,s,t}} = f(X_{s,t})$, where $X_{s,t}$ denotes the vector of satellite, meteorological, and cyclic predictors. The final output consisted of daily $PM_{2.5}$ maps at 0.01° × 0.01° spatial resolution ranging from 2005 to 2025, enabling high-resolution spatiotemporal exposure assessment for subsequent analyses.

### 2.6 City-level aggregated $PM_{2.5}$

Daily $PM_{2.5}$ concentrations were estimated for key locations across Ghana using an area-weighted spatial averaging approach applied to gridded satellite-derived air quality data. Geographic coordinates for 20 locations across Ghana were compiled and verified through manual inspection. These locations include the regional capitals: Bolgatanga (Upper East), Nalerigu (North East), Wa (Upper West), Tamale (Northern), Damongo (Savannah), Dambai (Oti), Techiman (Bono East), Sunyani (Bono), Goaso (Ahafo), Kumasi (Ashanti), Ho (Volta), Sefwi Wiawso (Western North), Koforidua (Eastern), Cape Coast (Central), Sekondi-Takoradi (Western), and Accra (Greater Accra). Additional locations of interest include Navrongo (Upper East), Kintampo (Bono East), Somanya (Eastern), and Tema (Greater Accra). To represent urban exposure while accounting for spatial heterogeneity in city size, circular buffers ranging from 1–9 km were defined around each city center based on visual assessment of the urban extent. Buffers were constructed in a projected coordinate system (UTM Zone 30N, EPSG:32630) to ensure accurate distance calculations in meters and subsequently transformed back to geographic coordinates (EPSG:4326) for compatibility with the $PM_{2.5}$ raster grid. For each city, daily $PM_{2.5}$ values were calculated using an area-weighted mean of all grid cells intersecting the buffer. Fractional overlap between each grid cell and the buffer polygon was computed to determine pixel-level weights, allowing partial grid cells along buffer boundaries to contribute proportionally to the average. This approach reduces bias introduced by binary inclusion or exclusion of edge pixels and provides a spatially

representative estimate of population-relevant exposure. The resulting dataset consists of daily $PM_{2.5}$ time series for each city over the study period, enabling consistent comparisons across northern and southern regions of Ghana.

## 2.7 Long-term $PM_{2.5}$ trend detection

To quantify the direction, magnitude, and statistical significance of long-term changes in surface $PM_{2.5}$ over Ghana, we applied the Mann-Kendall (MK) monotonic trend test and Sen's slope estimator to monthly mean $PM_{2.5}$ concentrations derived from the multi-model output between 2005 and 2025.

### 2.7.1 Mann-Kendall test

The MK test is a rank-based, non-parametric statistical procedure for detecting monotonic trends in time series data (Kendall, 1975; Mann, 1945). It makes no assumption about the underlying distribution of the data, making it particularly well-suited for environmental datasets, such as $PM_{2.5}$, which routinely exhibit non-normal distributions, heteroscedasticity, and intermittent extreme values. The test statistic $S$ is computed as:

$$S = \sum_{i=1}^{n-1} \sum_{j=i+1}^{n} \operatorname{sgn}\left(x_j - x_i\right) \ldots (4)$$

Where $x_i$ and $x_j$ are observations at times $i$ and $j$ (with $j > i$), $n$ is the total number of observations, and sgn(·) is the sign function returning +1, 0, or −1 for positive, zero, or negative differences, respectively. Under the null hypothesis of no monotonic trend ($H_0$: the data are independently and identically distributed with no temporal ordering), the standardized test statistic $Z$ is given by:

$$Z = \begin{cases} \dfrac{S-1}{\sqrt{\operatorname{Var}(S)}} & \text{if } S > 0 \\ 0 & \text{if } S = 0 \\ \dfrac{S+1}{\sqrt{\operatorname{Var}(S)}} & \text{if } S < 0 \end{cases} \ldots (5)$$

The variance of $S$ is adjusted for tied ranks in the data. A statistically significant positive (negative) $Z$ indicates a monotonically increasing (decreasing) trend. We adopt a two-tailed significance threshold of $\alpha = 0.05$, corresponding to $|Z| > 1.96$.

### 2.7.2 Seasonal Mann-Kendall Test

Monthly means were computed by averaging daily gridded $PM_{2.5}$ concentrations within each calendar month at every 1 km grid cell, yielding a time series of 252 monthly observations per grid cell. Monthly resolution was preferred compared to annual aggregation because it provides substantially more statistical value for trend detection in Ghana while retaining seasonally resolved trend information, such as elevated concentrations during the Harmattan period.

Since $PM_{2.5}$ in Ghana exhibits strong and recurring seasonal cycles, applying the standard MK test directly to the raw monthly time series can conflate underlying long-term trends with seasonal periodicity, inflating or suppressing the apparent trend signal. To address this, we employ the Seasonal Mann-Kendall (SMK) test from Hirsch and Slack (1984), which is specifically designed for time series with seasonal structure.(Hirsch and Slack, 1984) In the SMK framework, the *S* statistic is computed independently for each of the twelve calendar months, comparing, for example, all January values across 2005-2025, all February values across these years, and so on. The resulting within-season statistics are then summed to yield an overall test statistic:

$$S_{\text{total}} = \sum_{g=1}^{12} S_g \quad \ldots (6)$$

where $S_g$ is the MK statistic computed for calendar month $g$. The variance of $S_{\text{total}}$ accounts for any covariance between months arising from shared seasonal events (e.g., Harmattan onset), and the final *Z* statistic is derived from this pooled estimate.

### 2.7.3 Sen's slope estimator

The magnitude of any statistically significant trend was quantified using Sen's slope estimator, also known as the Theil-Sen estimator (Sen, 1968), which provides a robust, non-parametric measure of the rate of change. Sen's slope $\beta$ is defined as the median of all pairwise slopes between observations:

$$\beta = \text{median}\left(\frac{x_j - x_i}{j - i}\right), \quad \forall\ j > i \quad \ldots (7)$$

where $x_i$ and $x_j$ are the monthly mean $PM_{2.5}$ values for the same calendar month in years $i$ and $j$. The resulting slope $\beta$ is expressed in units of μg $m^{-3}$ $yr^{-1}$ and represents the central tendency of the trend rate, resistant to the influence of outliers or single anomalous events such as exceptional dust episodes.

The SMK test and Sen's slope were applied independently to the monthly mean $PM_{2.5}$ time series at each 1 km grid cell across Ghana to produce spatially resolved maps of trend magnitude and significance. Additionally, spatially averaged time series were computed for the national domain and for distinct sub-regions of Ghana (northern, middle, and southern belts) to characterize large-scale changes in $PM_{2.5}$ burden over the 21-year study period.

## 3 RESULTS AND DISCUSSION

### 3.1 Surface $PM_{2.5}$ measurements

The daily $PM_{2.5}$ concentrations collected by surface monitors during the measurement campaign (2018–2024) exhibit a mean concentration of 31.8 μg $m^{-3}$, indicating consistently elevated pollution levels across Ghana. The distribution of observed daily $PM_{2.5}$ concentrations is strongly right-skewed, characterized by a long tail toward higher concentration values, as shown in Fig. S6

of the Supplementary Materials. The 95th percentile $PM_{2.5}$ levels reached 81.1 µg $m^{-3}$, 2.6 times the mean concentration which highlights the frequent occurrence of episodic high-pollution events. The large proportion of Harmattan-season observations at higher $PM_{2.5}$ concentrations suggests that these extreme values are strongly associated with Harmattan dust transport during the dry season. The skewed distribution indicates that while most observations fall within moderate concentration ranges, a smaller proportion of high-concentration events contributes disproportionately to population exposure.

Fig. S7 shows violin distributions of measured daily $PM_{2.5}$ concentrations across all cities with surface monitoring locations, revealing pronounced spatial heterogeneity in mean daily $PM_{2.5}$. The embedded box plots indicate that median concentrations at all locations range between 15–40 µg $m^{-3}$, consistently exceeding the WHO 24-hour guideline of 15 µg $m^{-3}$.

## 3.2 Model performance

Model performance was rigorously evaluated across five machine learning algorithms, LASSO, RF, SVM, XGBoost and MLP, for three model configurations TROPOMI model, OMI model, and MERRA model, under random, temporal and spatial cross-validation (CV) schemes. MLP, also known as a fully connected neural network, is a neural network. The MLP model architecture used in this study is shown in Fig. S8 in the Supplementary Materials, whereas optimized hyperparameter information for each ML algorithm and mode configuration is summarized in Tables S5 to S7. Model performances metrics, including Pearson correlation coefficient (r), coefficient of determination ($R^2$), root-mean square error (RMSE) and mean-normalized RMSE (nRMSE), for all machine learning algorithms evaluated for the three model configurations are summarized in Table 1. Mean bias, mean absolute error (MAE), and mean-normalized MAE (nMAE) are presented in Tables S8–S10 as additional error metrics.

**Table 1. Performance comparison of machine learning algorithms TROPOMI, OMI, and MERRA models.** Model performance is evaluated under random, temporal, and spatial cross-validation using the coefficient of determination ($R^2$), Pearson correlation coefficient (r), bias, root mean squared error (RMSE), and normalized RMSE (nRMSE). Error metrics (RMSE and bias) are reported in µg $m^{-3}$. Additional error metrics are listed in Tables S8 to S10. Models selected for generating $PM_{2.5}$ concentration maps are indicated with an asterisk (*).

| **Algorithms** | **Random CV** | | | **Temporal CV** | | | **Spatial CV** | | |
|---|---|---|---|---|---|---|---|---|---|
| | $R^2$ (r) | RMSE (nRMSE) | Bias | $R^2$ (r) | RMSE (nRMSE) | Bias | $R^2$ (r) | RMSE (nRMSE) | Bias |
| ***TROPOMI Model*** | | | | | | | | | |
| LASSO | 0.60 (0.78) | 15.0 (0.48) | -0.17 | 0.56 (0.75) | 15.7 (0.50) | 0.33 | 0.45 (0.68) | 19.8 (0.57) | 2.96 |
| SVM | 0.69 (0.83) | 13.2 (0.42) | -1.55 | 0.55 (0.77) | 15.8 (0.50) | -0.36 | 0.52 (0.75) | 19.4 (0.55) | -5.91 |

| | | | | | | | | | |
|---|---|---|---|---|---|---|---|---|---|
| RF | 0.71 (0.85) | 12.7 (0.40) | 0.09 | 0.55 (0.77) | 15.9 (0.50) | 0.77 | 0.56 (0.76) | 18.4 (0.53) | -1.52 |
| **XGB*** | 0.72 (0.86) | 12.5 (0.40) | -0.01 | 0.57 (0.78) | 15.6 (0.49) | 0.66 | 0.57 (0.76) | 17.3 (0.49) | -0.93 |
| MLP | 0.71 (0.84) | 12.8 (0.40) | -0.12 | 0.54 (0.76) | 16.0 (0.51) | -1.56 | 0.42 (0.66) | 18.7 (0.54) | -2.75 |
| ***OMI Model*** | | | | | | | | | |
| LASSO | 0.58 (0.76) | 15.4 (0.49) | -0.19 | 0.53 (0.73) | 16.3 (0.52) | 0.35 | 0.38 (0.64) | 21.7 (0.59) | -4.19 |
| SVM | 0.68 (0.83) | 13.4 (0.42) | -1.79 | 0.52 (0.75) | 16.4 (0.52) | -1.31 | 0.48 (0.73) | 20.2 (0.57) | -5.55 |
| RF | 0.71 (0.84) | 13.0 (0.41) | -0.16 | 0.53 (0.75) | 16.3 (0.52) | 1.46 | 0.48 (0.75) | 19.3 (0.55) | -1.53 |
| **XGB*** | 0.72 (0.85) | 12.8 (0.41) | 0.04 | 0.56 (0.76) | 15.6 (0.50) | 0.75 | 0.54 (0.75) | 18.9 (0.54) | -1.01 |
| MLP | 0.70 (0.83) | 13.3 (0.42) | -1.19 | 0.50 (0.71) | 16.6 (0.53) | 1.78 | 0.46 (0.70) | 19.8 (0.57) | -1.83 |
| ***MERRA Model*** | | | | | | | | | |
| LASSO | 0.63 (0.79) | 14.5 (0.46) | -0.19 | 0.58 (0.75) | 15.2 (0.48) | -0.06 | 0.41 (0.67) | 18.2 (0.57) | -4.63 |
| SVM | 0.70 (0.83) | 12.7 (0.41) | -1.68 | 0.55 (0.76) | 15.9 (0.50) | -1.17 | 0.37 (0.66) | 19.0 (0.60) | 5.60 |
| RF | 0.71 (0.84) | 12.6 (0.40) | 0.38 | 0.51 (0.75) | 16.6 (0.53) | 1.37 | 0.47 (0.70) | 17.2 (0.54) | 2.16 |
| **XGB*** | 0.72 (0.85) | 12.6 (0.40) | -0.18 | 0.59 (0.78) | 15.2 (0.48) | 0.03 | 0.49 (0.73) | 16.8 (0.50) | 0.39 |
| MLP | 0.70 (0.83) | 12.9 (0.42) | 1.03 | 0.55 (0.74) | 16.0 (0.51) | 1.92 | 0.44 (0.69) | 18.0 (0.55) | -1.54 |

Under random cross-validation, XGBoost achieved the best and consistent performance across all three model configurations, with $R^2$ of 0.72 for TROPOMI, OMI, and MERRA models and RMSE

values of 12.5, 12.8, and 12.6 µg $m^{-3}$, respectively. Linear models (LASSO) consistently showed the weakest performance, with $R^2$ approximately 0.09–0.12 lower than XGBoost and substantially higher RMSE across all cross-validation schemes, reflecting their limited ability to capture the non-linear relationships of surface $PM_{2.5}$ with meteorological and satellite-derived aerosol predictors in the heterogeneous emission environments in Ghana. Support vector machines (SVM) showed competitive random-CV performance but degraded substantially under spatial and temporal cross-validation. Among the non-linear approaches, tree-based ensemble methods RF and XGBoost performed comparably under random cross-validation, but XGBoost exhibited consistently lower bias (–0.01, 0.04, and –0.18 µg $m^{-3}$ for TROPOMI, OMI and MERRA models, respectively) and comparable or lower normalized errors across all CV schemes. The regression slopes in Figs. 2A–C (0.72–0.73) further indicate that XGB predictions closely track observed variability in $PM_{2.5}$, with only minor underestimation at higher $PM_{2.5}$ concentrations.

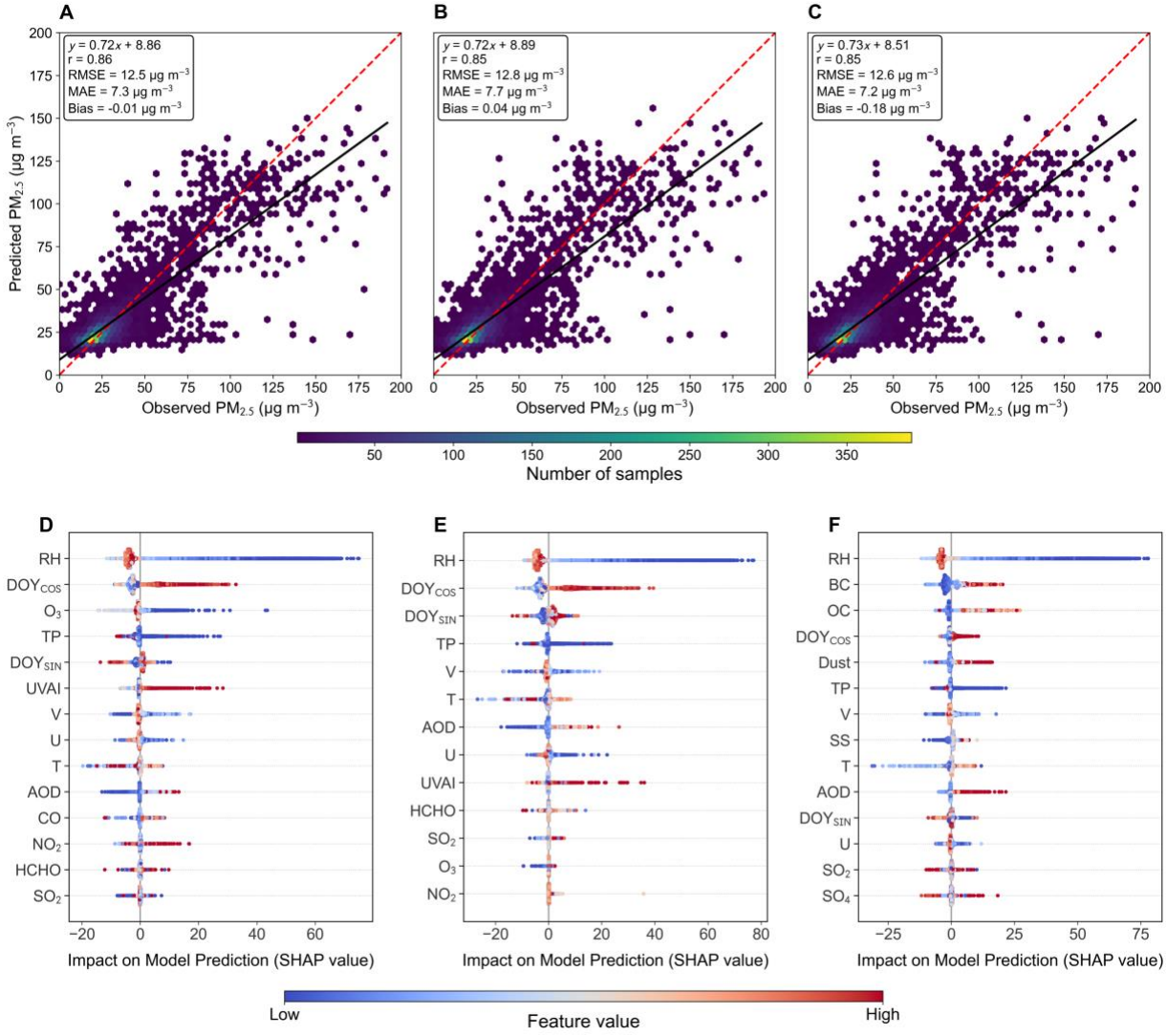


**Fig. 2. Model performance and interpretability of XGBoost $PM_{2.5}$ prediction models. (A–C)** Scatterplots show the relationship between daily observed $PM_{2.5}$ concentrations from surface monitors and corresponding model estimates for TROPOMI, OMI, and MERRA-2 models. Each

point represents paired daily observations from surface monitors and corresponding model estimates. The red dashed line denotes the 1:1 reference line, while the solid black line represents the fitted linear regression. All models demonstrate strong agreement between observations and predictions ($r \approx 0.84–0.85$) with slopes close to unity, indicating good representation of variability and slight underestimation at higher $PM_{2.5}$ concentrations. Color shading indicates the density of samples. **(D–F)** SHAP summary plots show the relative importance and direction of feature contributions to $PM_{2.5}$ predictions for TROPOMI, OMI, and MERRA-2 models. Each point represents an individual sample, colored according to the feature value (blue = low, red = high). The horizontal spread of points indicates the magnitude and direction of each feature's influence on model output, with features ordered by overall importance.

Consistent with performances of spatiotemporal models in other studies, model performance declined under temporal and spatial cross-validation relative to random cross-validation across all algorithm and model types, which reflects additional challenge of generalizing to time periods or geographic locations unfamiliar to the models (Chi et al., 2022). Under temporal cross-validation, XGBoost shows $R^2$ values of 0.57, 0.56, and 0.59 TROPOMI, OMI, and MERRA models, with RMSE increasing to 15.6, 15.6, and 15.2 μg $m^{-3}$, respectively. Under spatial cross-validation, arguably the most operationally relevant metric for applying the model to unmonitored grid cells across Ghana, XGBoost $R^2$ values were 0.57, 0.54, and 0.49 for TROPOMI, OMI, and MERRA models. The MLP model showed the largest degradation under spatial cross-validation, with $R^2$ falling to 0.45, 0.38, and 0.41 for TROPOMI, OMI, and MERRA models, indicating greater susceptibility to overfitting to sensor-specific concentration patterns when the training sample is limited to a sparse monitoring network. In addition to more robust spatial and temporal generalization of XGBoost, better interpretability through SHAP-based analysis provides insight into the relative contributions of meteorological and aerosol predictors, further supporting its suitability for generating spatially continuous daily $PM_{2.5}$ maps across unmonitored regions and time periods of Ghana. Therefore, XGBoost was selected as the final model for further analysis. Figs. 2A–C further illustrates the agreement between observed and predicted $PM_{2.5}$ concentrations for the best-performing model (XGBoost) under random CV, showing strong clustering along the 1:1 line and limited systematic bias across the concentration range.

Among the three model schemes, the MERRA model achieved the lowest spatial and temporal cross-validation RMSE values of 15.2 μg $m^{-3}$ and 16.8 μg $m^{-3}$, respectively. However, spatially cross-validated $R^2$ for the MERRA model (0.49) is slightly lower than that of the other models (0.54-0.57), suggesting that the lower absolute RMSE is partly attributable to the reduced $PM_{2.5}$ dynamic range in this gap-filling dataset due to inherently larger grid sizes of MERRA-2 dataset. The higher temporally cross-validated $R^2$ of 0.59 indicates improved representation of diel variability in aerosol-related predictors from MERRA-2 compared to only once-a-day measurements from TROPOMI and OMI. Nonetheless, the MERRA model provides physically consistent estimates during periods of satellite data unavailability, ensuring complete spatiotemporal coverage in the final merged product.

SHAP analysis plots in Figs. 2D–2F provide insights into the influence of predictor variables on $PM_{2.5}$ concentrations. The results indicate that meteorological and seasonal predictors dominate $PM_{2.5}$ variability in Ghana. Relative humidity exhibited the strongest influence on model predictions, with low-humidity conditions strongly associated with elevated $PM_{2.5}$ concentrations. This asymmetric and wide range of SHAP response under dry conditions suggests that low-RH

acts as a strong indicator of Harmattan season and contributes positively to ambient $PM_{2.5}$ concentrations due to enhanced dust transport and low rainfall during the dry season. In contrast, high-humidity conditions during the wet seasons correspond predominantly to negative SHAP values, consistent with efficient wet scavenging and reduced aerosol loading under increased precipitation and enhanced aerosol removal.

The seasonal cyclic features represented by the sine and cosine transformations of DOY exhibited large absolute SHAP values distributed across both positive and negative directions, indicating that the model successfully captured the strong annual periodicity of $PM_{2.5}$ concentrations in Ghana. Wind speeds (U and V) and precipitation variables from ERA5-Land also contributed through their influence on dust transport intensity and wet deposition of aerosols, respectively. These results are broadly consistent with findings from a recent satellite-based $PM_{2.5}$ study in West Africa by Westervelt et al. (2025), which identified meteorological drivers and dust transport as major determinants of surface aerosol loading.

Satellite-derived aerosol indicators, particularly the ultraviolet aerosol index (UVAI), showed consistently positive SHAP contributions in both the TROPOMI and OMI models, indicating higher predicted $PM_{2.5}$ concentrations under elevated absorbing aerosol conditions. These conditions are commonly associated with mineral dust transport during the Harmattan season and episodic biomass burning, highlighting the importance of absorbing aerosol loading in shaping surface $PM_{2.5}$ variability. For the MERRA-2-based model, PM composition variables, particularly BC, OC, and dust, exhibited increased importance alongside meteorological predictors. The strong contributions from dust-related variables are consistent with the influence of Harmattan-driven mineral dust transport, while BC and OC likely reflect contributions from combustion-related aerosol sources, including biomass burning and other anthropogenic emissions. SHAP values for AOD suggest that the column-integrated aerosol loading represented by AOD in the MERRA-2 reanalysis provides valuable predictive information, particularly during high-$PM_{2.5}$ episodes, similar to the role of UVAI in OMI- and TROPOMI-based models. Despite differences in predictor types among the three model configurations, the overall consistency in dominant drivers provides confidence that the modeling framework captures physically meaningful controls on $PM_{2.5}$ variability across seasons and regions.

### 3.3 Daily $PM_{2.5}$ distribution and long-term spatiotemporal trends

The daily $PM_{2.5}$ concentrations derived at 1 km × 1 km resolution for 2005–2025 were used for assessing spatial and long-term patterns. Daily $PM_{2.5}$ concentration distributions for Harmattan and non-Harmattan periods are illustrated in Fig. 3A. During the non-Harmattan season, the distribution is relatively narrow, with a mode around 20 $\mu g\ m^{-3}$ and limited probability mass extending beyond 60 $\mu g\ m^{-3}$, reflecting more consistent and moderate pollution conditions driven primarily by local and regional anthropogenic sources. In contrast, the Harmattan season distribution is characteristically broader, with a mode ~69 $\mu g\ m^{-3}$ and a pronounced long tail extending to around 150 $\mu g\ m^{-3}$, strongly indicating episodic high-concentration events associated with large amounts of mineral dust transport from the Sahara and Sahel to the West African regions during this season. Notably, both distributions are almost entirely (>99%) situated above the WHO 24-hour air quality guideline of 15 $\mu g\ m^{-3}$ (dashed red line), underscoring that $PM_{2.5}$ exceedances in Ghana are not confined to the dust season but represent a year-round public health concern due to high exposure to ambient particulate matter. The wider spread and heavier tail of the Harmattan-

season distribution imply that $PM_{2.5}$ exposure among the Ghanaian population during this period is not only substantially more variable, but also consistently higher, with extreme pollution episodes frequently reaching concentration 2-10 times higher than the WHO 24-hour guideline.

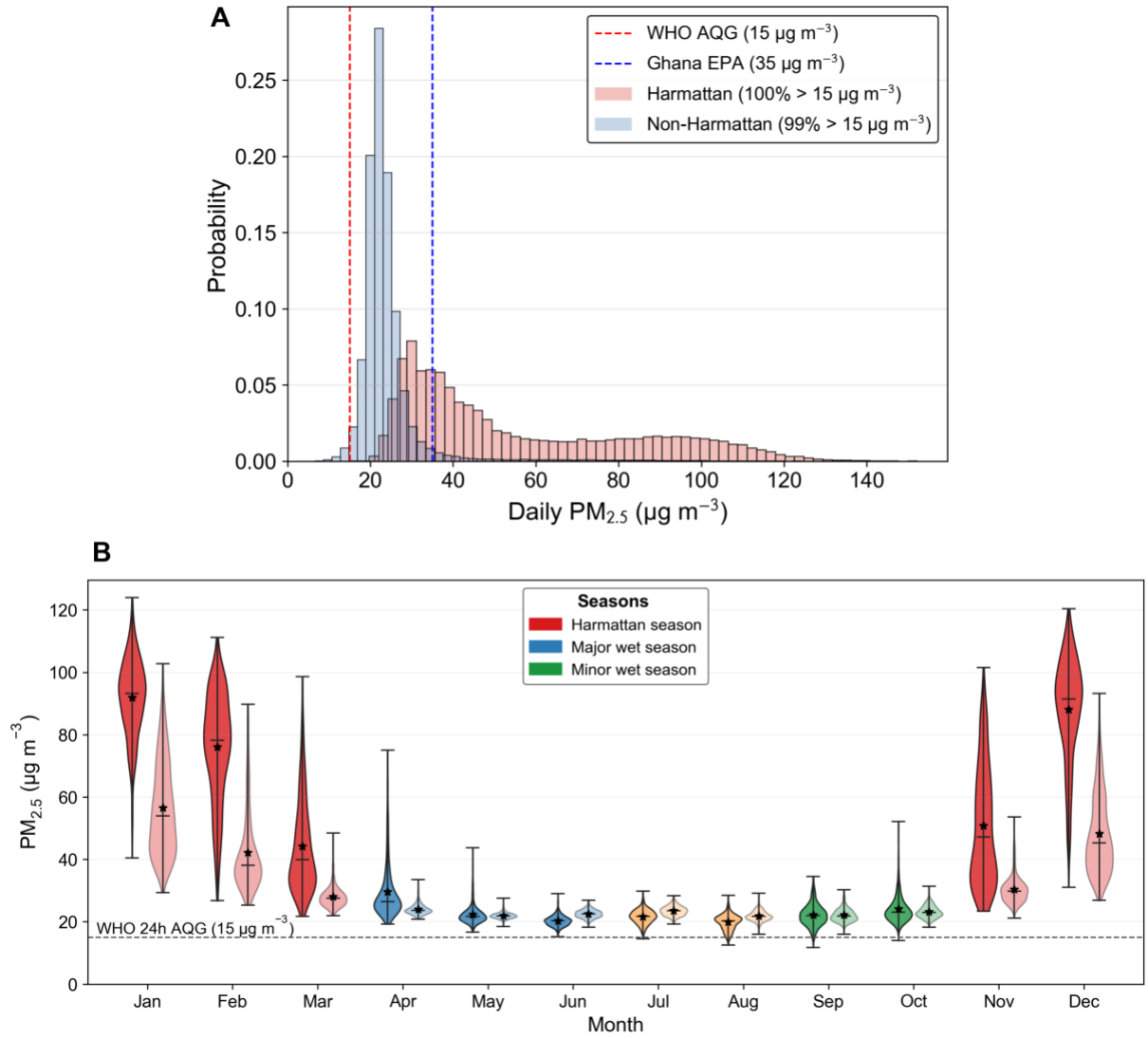


**Fig. 3. Seasonal distribution and monthly variability of daily $PM_{2.5}$ concentrations across Ghana (2005–2025). (a)** Probability distributions of daily $PM_{2.5}$ concentrations during Harmattan (red) and non-Harmattan (blue) periods. Harmattan conditions exhibit a broader distribution and substantially higher concentrations, reflecting the influence of long-range Saharan dust transport. The red and blue dashed vertical lines indicate the 24-hour air quality guidelines from WHO (15 μg $m^{-3}$) and Ghana EPA (35 μg $m^{-3}$), highlighting extremely high number of exceedances, particularly during Harmattan months. **(b)** Monthly climatology of daily $PM_{2.5}$ concentrations for Harmattan, major wet, and minor wet seasons across Northern (dark shading) and Southern (light shading) Ghana. Violin plots illustrate the distribution of daily values for each month. The central horizontal line within each violin denotes the median, and the star marker indicates the monthly mean concentration. The dashed horizontal line represents the WHO 24-hour air quality guideline

(15 $\mu g\ m^{-3}$), showing that exceedances occur predominantly during Harmattan months, particularly in Northern Ghana.

These distributions for 20 locations, including regional capitals, in Ghana are shown in Fig. S9. The northern region shows a strong characteristic normal $PM_{2.5}$ distribution with a wider spread during the Harmattan period, opposed to a narrow distribution and much lower means for southern regions of Ghana. Big cities of Ghana, such as Accra, Cape Coast, Sekondi–Takoradi and Kumasi, are mostly located in the South, and show a much narrower $PM_{2.5}$ distribution with less pronounced seasonal variability during this period. On the other hand, rural or sub-urban locations exhibit relatively broader $PM_{2.5}$ distribution, potentially reflecting greater variability in emission sources, including episodic agricultural burning and savannah fires during the dry season (Ofosu et al., 2013).

Fire activity is an additional important contributor to seasonal $PM_{2.5}$ variability in Ghana, particularly across northern and transitional ecological zones dominated by savanna land cover (Fig. S10). Analysis of the MODIS MCD12Q1 Version 6.1 land cover observations in 2024 indicates that savannas (42%), grasslands (27%), and woody savannas (10%) together account for nearly 80% of Ghana's land area, with these ecosystems concentrated primarily in northern Ghana and the forest–savanna transition belt (Fig. S11). Fire detections derived from MODIS active fire products for 2005–2025 show that fire occurrence is spatially concentrated in these savanna-dominated regions, consistent with widespread seasonal biomass burning associated with agricultural land management, pasture renewal, and accidental wildfires. Annual mean fire frequency and fire radiative power (FRP), a proxy for combustion intensity, both show pronounced seasonal dependence, with substantially higher activity and FRP during the dry Harmattan period (December–February) relative to the wetter non-Harmattan months. The elevated frequency and intensity of fires during the Harmattan season likely enhance regional aerosol loading through increased emissions of carbonaceous particulate matter, contributing to the broader and more right-skewed $PM_{2.5}$ distribution observed during this period. Frequent fire occurrences concentrated predominantly within the savanna regions of Ghana suggest that biomass burning may contribute to seasonal aerosol loading and $PM_{2.5}$ variability in Ghana, complementing the dominant influence of long-range Saharan dust transport during Harmattan conditions (Ofosu et al., 2013).

This north-south difference in $PM_{2.5}$ exposure levels is even more evident from monthly $PM_{2.5}$ climatology averaged over the 21-year study period (2005–2025), disaggregated by northern and southern regions of Ghana shown in Fig. 3B. Ghana is classified into northern and southern subregions, defined as regions above and below 8º N latitude, respectively (Klutse et al., 2020). A pronounced seasonal cycle can be observed for monthly mean $PM_{2.5}$ in Ghana, with peak concentrations occurring from November through March, coinciding with the Harmattan season. Typically, North experiences 1.63 to 1.83 times higher PM exposure compared to the South. $PM_{2.5}$ concentrations decline sharply with the onset of the major wet season in April–June, driven by enhanced wet removal of atmospheric particles and suppressed dust transport. A secondary minimum occurs during the minor wet season (September–October), separated from the major wet season by a brief mid-season dry period in July–August during which $PM_{2.5}$ concentrations exhibit a modest secondary peak. This bimodal wet season structure is more pronounced in southern Ghana, consistent with the bimodal rainfall regime associated with the seasonal northward and southward migration of the Intertropical Convergence Zone (ITCZ) over the coastal and forested zones of West Africa (Nicholson, 2018). In contrast, northern Ghana exhibits a unimodal rainfall

pattern peaking in August and September (Fig. S12), during which monthly mean $PM_{2.5}$ concentrations (19.9 µg $m^{-3}$) are lower than those observed in the south (21.0 µg $m^{-3}$).

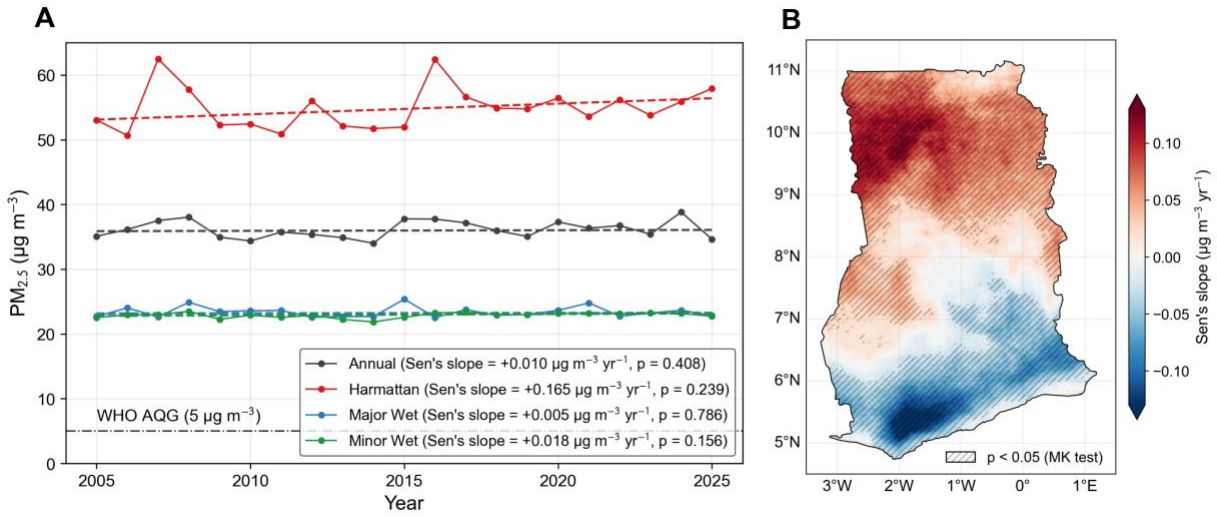


**Fig. 4. Long-term spatiotemporal trends in ambient $PM_{2.5}$ concentrations across Ghana from 2005 to 2025.** (a) Ghana-wide annual and seasonal mean $PM_{2.5}$ concentrations, including Harmattan, Major Wet, and Minor Wet seasons. Dashed lines represent trends estimated using the Theil–Sen slope estimator, with corresponding slope magnitudes and Mann–Kendall test p-values reported in the legend. The horizontal dash–dotted line indicates the WHO annual air quality guideline (AQG) of 5 µg $m^{-3}$. (b) Spatial distribution of pixel-wise $PM_{2.5}$ trends estimated using the Theil–Sen slope estimator. Stippling denotes statistically significant trends ($p<0.05$) based on the Mann–Kendall test. Positive values indicate increasing $PM_{2.5}$ concentrations over time, while negative values indicate decreasing trends.

Fig. 4A shows the seasonal and annual evolution of $PM_{2.5}$ in Ghana over the 21-year period. Annual mean $PM_{2.5}$ has remained relatively stable over the study period with the Sen's slope estimate indicating an average annual increase of only 0.01 µg $m^{-3}$ every year and seasonal slopes varying between 0.005–0.165 µg $m^{-3}$ $yr^{-1}$. Mann-Kendall's test suggests that these seasonal and yearly trends observed in Ghana are not statistically significant ($p\geq0.05$). However, spatial map of Sen's slope estimate for Ghana at 1 km × 1 km grid resolution in Fig. 4B indicates the majority of Ghana has experienced a statistically significant trend. The Sen's slope estimates and $p$ values calculated from Mann–Kendall test is summarized in Table S11.

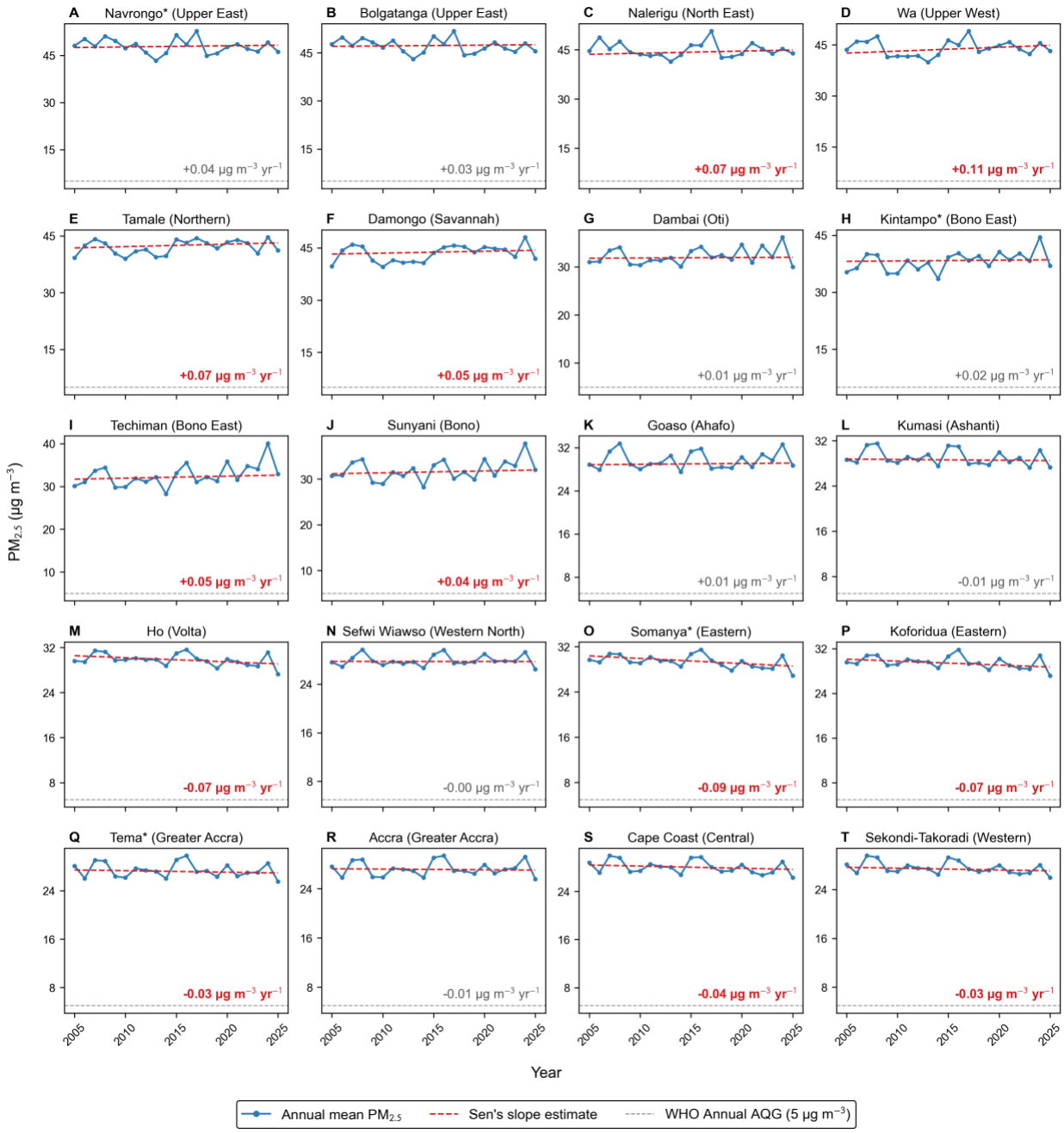


725

726 **Fig. 5. Temporal trends in annual mean $PM_{2.5}$ concentrations across Ghanaian regional**
727 **capitals from 2005–2025.** (A–T) Each panel shows the yearly average $PM_{2.5}$ concentration (blue
728 line with markers), Sen's slope trend (red dashed line), and the WHO annual $PM_{2.5}$ guideline of 5
729 µg $m^{-3}$ (grey dashed line) for regional capitals and non-regional capitals (*). The estimated Sen's
730 slope (µg $m^{-3}$ $yr^{-1}$) is shown in the lower-right corner of each panel. Slope values with statistically
731 significant trends ($p \leq 0.05$) assessed by Mann–Kendall test is indicated in bold red values. Results
732 indicate generally stable or modestly increasing $PM_{2.5}$ levels across most cities, with several
733 statistically significant increasing trends observed, while annual mean concentrations in all cities
734 consistently exceed the WHO AQG threshold throughout the study period.

City scale trend plots in Fig. 5 show, increasing $PM_{2.5}$ trends (0.05–0.11 μg $m^{-3}$ $yr^{-1}$) over the 21-year study period in some suburban and rural regions such as Nalerigu, Wa, and Damongo in northern Ghana. Another region exhibiting increasing $PM_{2.5}$ trends is Bono and Bono East, where cities such as Sunyani and Techiman may reflect increasing emissions associated with anthropogenic activities in these rapidly developing urban centers in addition to contributions from Harmattan-related $PM_{2.5}$ episodes. In contrast, several southern cities exhibit statistically significant declining trends, with the strongest decreases observed in Somanya (−0.090 μg $m^{-3}$ $yr^{-1}$, $p < 0.001$), Ho (−0.073 μg $m^{-3}$ $yr^{-1}$, $p < 0.001$), and Koforidua (−0.070 μg $m^{-3}$ $yr^{-1}$, $p < 0.001$), followed by Cape Coast (−0.036 μg $m^{-3}$ $yr^{-1}$), Sekondi-Takoradi (−0.029 μg $m^{-3}$ $yr^{-1}$), and Tema (−0.025 μg $m^{-3}$ $yr^{-1}$), which may be associated with improvements in vehicular fuel quality (Ayetor et al., 2025) and gradual adoption of cleaner household energy sources, potentially reflecting more effective policy implementation in the urbanized southern coastal regions of Ghana. Although these trends are statistically significant, their cumulative magnitudes over the 21-year period (approximately 0.5–1.9 μg $m^{-3}$) are modest relative to the model's daily spatial prediction uncertainty, which ranges from approximately 7–21 μg $m^{-3}$ RMSE across southern monitoring sites (Fig. S13). However, the trend detection analysis was performed on annual means, for which unsystematic daily errors are largely attenuated through temporal averaging, reducing the effective uncertainty to only a fraction of the daily RMSE. Thus, the Mann-Kendall test can reliably identify these directional changes. A map of leave-one-site-out cross-validation RMSE at the monitoring locations is provided in Fig. S13 to contextualize model uncertainty in estimating daily $PM_{2.5}$ across Ghana.

Although long-term changes in $PM_{2.5}$ across Ghanaian suburban and urban locations are modest, typically ranging between -0.2 μg $m^{-3}$ $yr^{-1}$ to 0.2 μg $m^{-3}$ $yr^{-1}$, these trends reveal a clear and widening north-south divergence in $PM_{2.5}$ exposure over the 21-year record. Positive trends in northern Ghana contrast with stable or declining trends in the south, reflecting differences in dominant drivers of $PM_{2.5}$ variability across regions. In northern Ghana, increases are consistent with the continued influence of Harmattan dust, regionally transported aerosols, and Savannah fires, whereas several southern urban centers show stable or declining concentrations indicative of gradual changes in local emission patterns. At the national scale, the strong influence of interannual variability in Harmattan dust loading limits the detectability of statistically significant Ghana-wide trends, making it challenging to isolate long-term emission-driven changes from meteorological variability.

Trends during the non-Harmattan season are broadly consistent with the Seasonal Mann–Kendall results (Table S11) and provide additional insight into long-term $PM_{2.5}$ variability after accounting for the dominant seasonal dust cycle. Several southern cities, including Somanya, Ho, Koforidua, Tema, Cape Coast, and Sekondi-Takoradi, exhibit statistically significant declines in non-Harmattan $PM_{2.5}$ concentrations, suggesting gradual improvements in baseline air quality conditions outside the dust season. In contrast, northern cities such as Wa and Tamale show persistent positive non-Harmattan trends, indicating that factors beyond long-range dust transport, including local emissions and biomass burning, contribute to sustained $PM_{2.5}$ exposure levels throughout the year. The spatial heterogeneity in non-Harmattan trends reinforces the north-south divergence observed in annual trends and highlights the combined influence of regional atmospheric processes and evolving local emission sources on long-term $PM_{2.5}$ variability across Ghana.

### 3.4 Exceedances for air quality guidelines

The spatial distribution of exceedance frequency relative to Ghana EPA 24-hour guideline (35 μg $m^{-3}$) is shown in Fig. 6. During 2005–2025 (Fig. 6A), exceedances occur on approximately 15–20% of days across southern Ghana and 35–42% of days in northern regions. Restricting the analysis to non-Harmattan periods (Fig. 6B) substantially lowers exceedance frequency, with little to no exceedance in the south and fewer than 10% of days exceeding the guideline in northern Ghana. In contrast, exceedance frequencies relative to the WHO 24-hour guideline (15 μg $m^{-3}$), shown in Fig. S14, remain above 90% across entire Ghana, including the southern coastal zone, reflecting the widespread and year-round burden of ambient $PM_{2.5}$ across Ghana in both Harmattan and non-Harmattan periods. Persistently high exceedance frequencies in major urban centers such as Accra, Kumasi, and Tema indicate that anthropogenic emissions contribute to sustained $PM_{2.5}$ exposure beyond the Harmattan season, highlighting the year-round burden of ambient air pollution across Ghana.

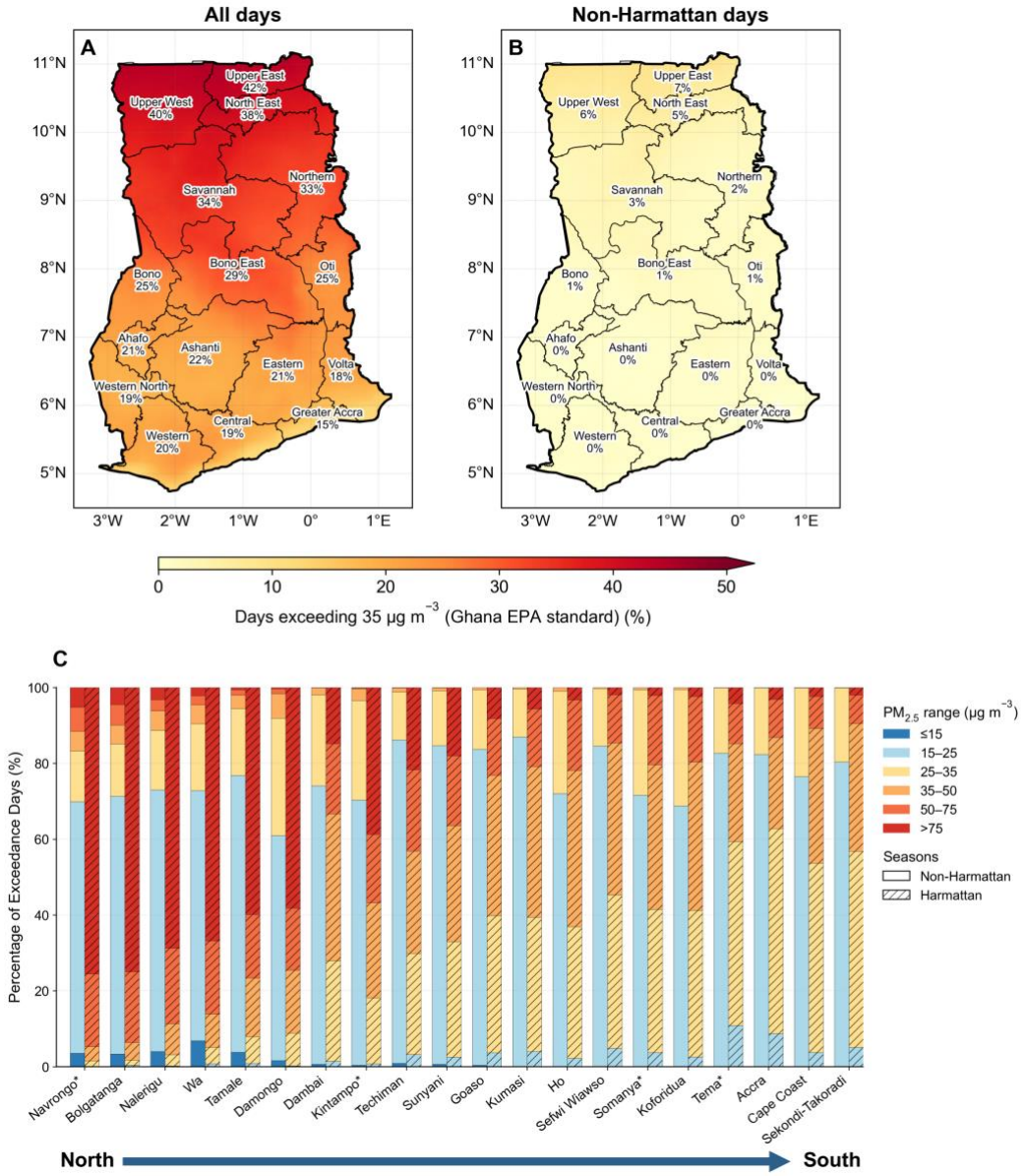


792

793 **Fig. 6. Ghana-wide exceedance frequency of daily $PM_{2.5}$ air quality guidelines.** Spatial
794 distribution of the percentage of days exceeding the Ghana EPA $PM_{2.5}$ guideline (35 µg $m^{-3}$) across
795 Ghana during 2005–2025. Panels show exceedance frequency calculated using (A) all available
796 days and (B) non-Harmattan days. Values represent the proportion of days (%) at each grid cell
797 where daily $PM_{2.5}$ concentrations exceeded 35 µg $m^{-3}$. Plot C shows the percentage of days
798 exceeding daily $PM_{2.5}$ for each concentration range (≤15, 15–25, 25–35, 35–50, 50–75, and >75
799 µg $m^{-3}$) across WHO and Ghana EPA air quality guideline categories during non-Harmattan and
800 Harmattan seasons for locations across Ghana (2005–2025). Cities are ordered geographically
801 from north (left) to south (right) with non-regional capitals indicated by an asterisk (*).

802 The city-level frequency distribution of daily $PM_{2.5}$ concentration ranges, shown in the bar plot in
803 Fig. 6C, further quantifies the north-south contrast. The bars are categorized using 24-hour

804 thresholds of the WHO Air Quality Guideline (15 μg $m^{-3}$), WHO Interim Target 4 (25 μg $m^{-3}$),
805 Ghana EPA standard (35 μg $m^{-3}$), WHO Interim Target 2 (50 μg $m^{-3}$), and WHO Interim Target 1
806 (75 μg $m^{-3}$). During the Harmattan season, northern cities record substantially higher proportions
807 of days exceeding 50 and 75 μg $m^{-3}$ compared to southern cities, while even during non-Harmattan
808 conditions, fewer than 10% of days in any Ghanaian city fall below the WHO 24-hour guideline
809 of 15 μg $m^{-3}$. The annual frequency corresponding to each concentration range for these cities is
810 shown in Fig. S15. Collectively, these exceedance patterns demonstrate that ambient $PM_{2.5}$ in
811 Ghana constitutes a pervasive and chronic public health threat that cannot be attributed solely to
812 episodic Harmattan dust events, underscoring the need for sustained emission reduction efforts
813 across all seasons.

## 3.5 Long-term mean $PM_{2.5}$ in Ghana

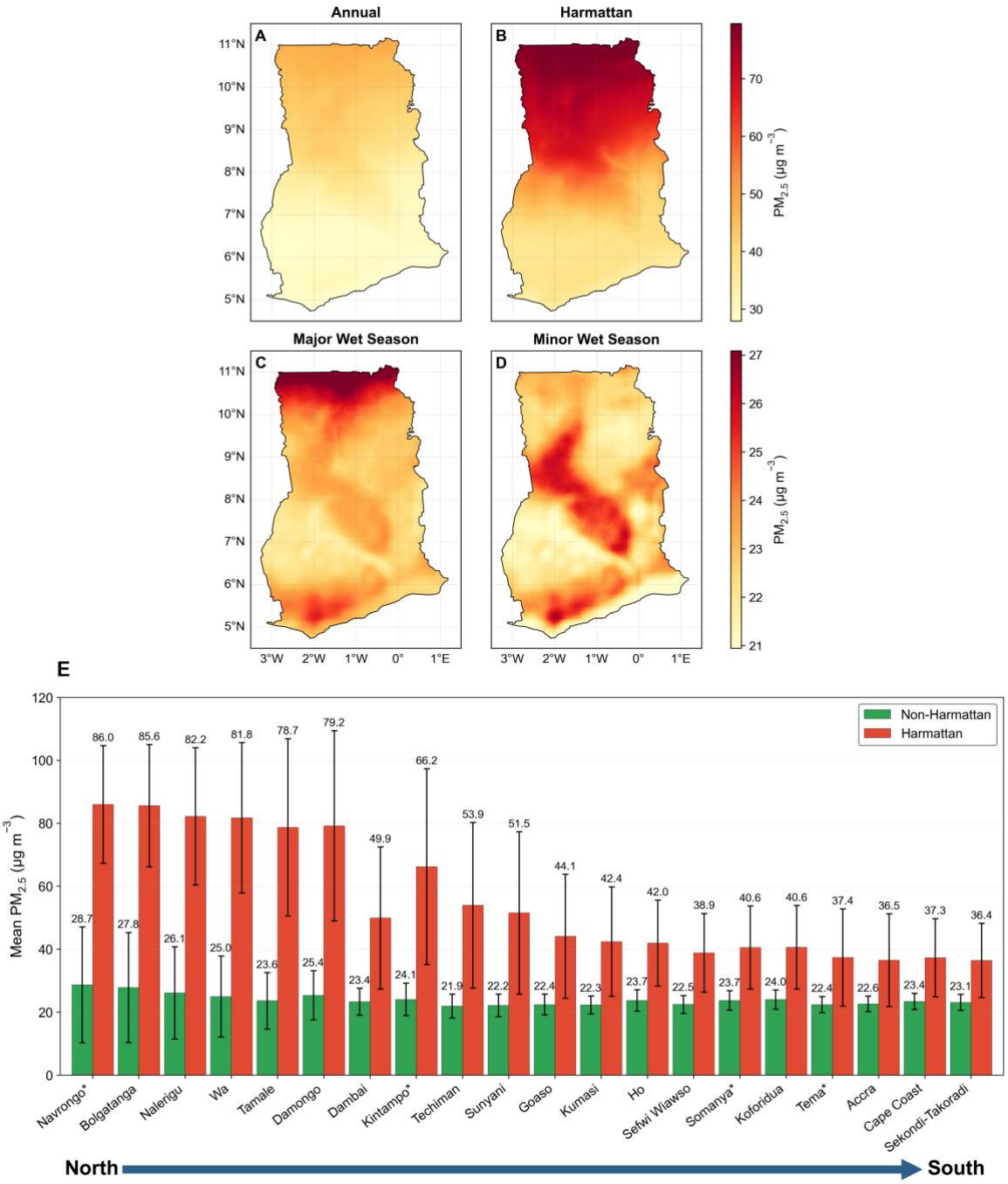


**Fig. 7. Spatial distribution of long-term means of $PM_{2.5}$ concentrations across Ghana.** Maps A–D show average $PM_{2.5}$ concentrations during 2005–2025 for annual conditions, Harmattan season, major wet season, and minor wet season, respectively. Color scales are adjusted separately for each row to highlight spatial variability with high (annual and Harmattan) and low $PM_{2.5}$ concentrations (wet seasons). E shows the mean daily $PM_{2.5}$ for regional capitals and additional

821 locations (indicated with *) in Ghana during Non-Harmattan and Harmattan seasons between
822 2005–2025. The mean $PM_{2.5}$ concentrations (in $\mu g\ m^{-3}$) are shown above the error bars.

823 The 21-year mean spatial distribution of $PM_{2.5}$ across Ghana (Fig. 7) reveals a pronounced north–
824 south gradient that is most extreme during the Harmattan season (Fig. 7B) and attenuates
825 substantially during the wet seasons (Figs 7C–D). The 21-year annual mean (Fig. 7A) shows
826 consistently elevated concentrations in the Upper East, Upper West, and Northern/Savanna regions
827 compared to the forested south, reflecting the dominant influence of Harmattan-transported
828 mineral dust from Saharan and Sahelian regions that disproportionately affects northern Ghana
829 due to its open savanna landscape and exposure to dry northeasterly winds. During the major wet
830 season (Fig. 7C), $PM_{2.5}$ concentrations are markedly reduced nationally and the north-south
831 gradient attenuates substantially, driven by enhanced wet deposition and suppressed dust transport,
832 while southern coastal cities retain discernible $PM_{2.5}$ elevations relative to the rural background,
833 reflecting persistent contributions from traffic, open waste burning, and industrial activity. The
834 minor wet season (Fig. 7D) shows intermediate concentrations with partial recovery of the north–
835 south gradient. The city-level seasonal comparison (Fig. 7E) directly quantifies these contrasts:
836 northern and central cities consistently experience substantially higher Harmattan-season $PM_{2.5}$
837 than their non-Harmattan levels, while southern coastal cities show comparatively muted
838 seasonality, consistent with the dominance of year-round anthropogenic rather than dust-driven
839 sources at those locations.

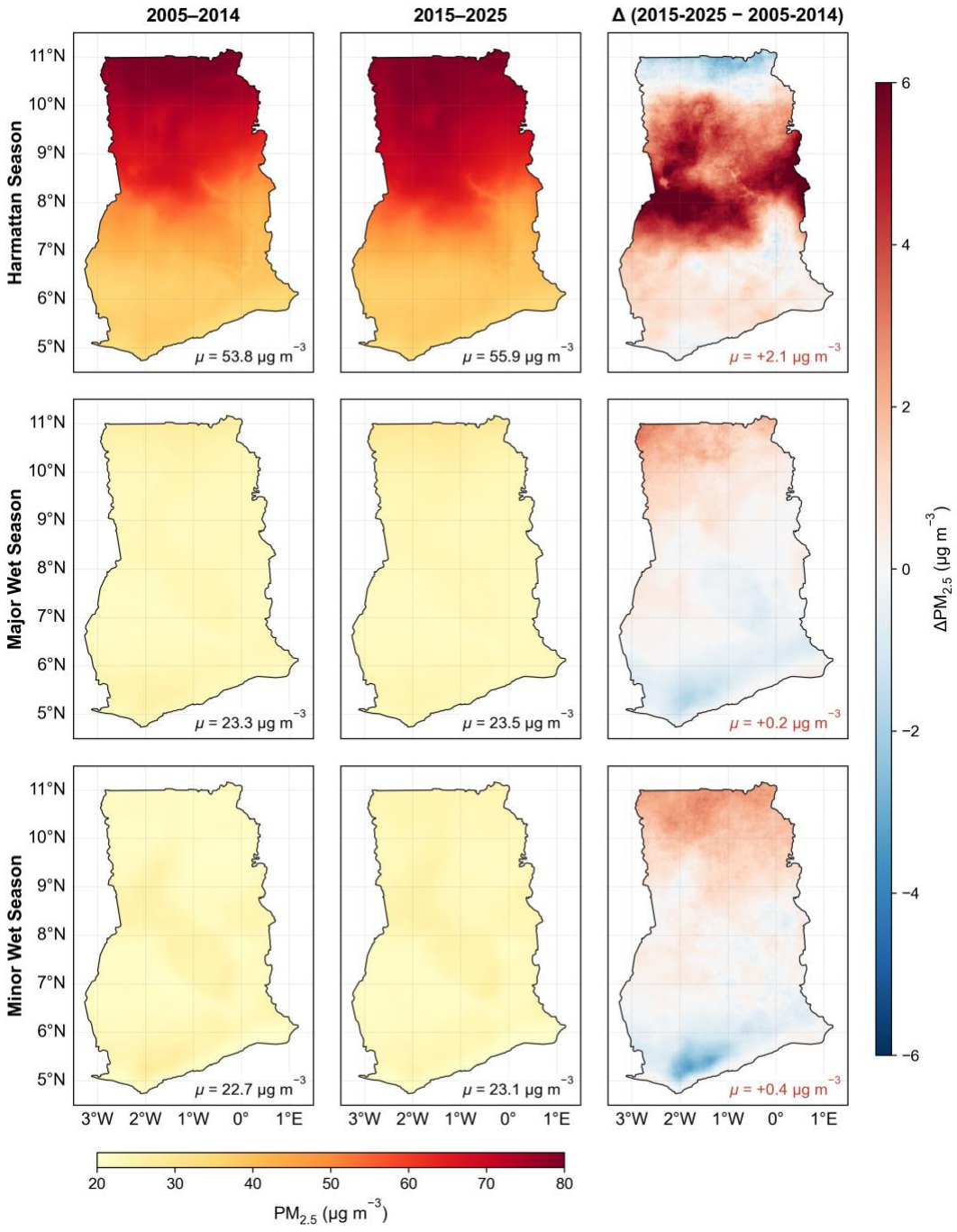


**Fig. 8. Multi-year changes in seasonal mean $PM_{2.5}$ concentrations across Ghana.** Maps show spatial patterns of mean $PM_{2.5}$ concentrations for the Harmattan, major wet, and minor wet seasons for two multi-year periods (2005–2014 and 2015–2025), along with the corresponding differences (Δ = 2015–2025 minus 2005–2014). μ denotes the spatial mean concentration for each panel. The color scale for the mean concentration levels is in the bottom, while the diverging color scale on the right highlights the magnitude of change.

Decadal-scale changes in seasonal $PM_{2.5}$ concentrations, comparing the first (2005–2014) and second (2015–2025) halves of the study period, are shown in Fig. 8. During the Harmattan season, difference maps reveal a net increase in $PM_{2.5}$ across much of northern Ghana in the more recent decade, consistent with the upward Sen's slope estimates for Wa, Tamale, Nalerigu, and Damongo (Table S11) and potentially reflecting intensified dust mobilization from Sahelian source regions under changing land use and climate conditions. In contrast, wet season $PM_{2.5}$ shows modest decreases in parts of southern Ghana between the two periods, particularly in and around major urban centers, corroborating the declining trends observed in Fig. 5 and Table S11 for cities such as Somanya, Ho, and Koforidua. Spatially, the most notable inter-decadal increases are concentrated along the northern belt, while decreases are evident in the southeastern coastal zone. Period-by-period comparisons at finer temporal resolution, comparing 2005–2009 with 2010–2014, 2010–2014 with 2015–2019, and 2015–2019 with 2020–2025, are provided in Figs. S16–S18. Together, these analyses document a diverging trajectory of $PM_{2.5}$ exposure in Ghana over the 21-year record, with a widening disparity between a dust-burdened north experiencing increasing concentrations and a south showing modest but measurable improvements.

# 4 CONCLUSIONS

In this study, we developed three complementary XGBoost models to achieve complete spatiotemporal coverage, with OMI-based (2005–May 6, 2018) and TROPOMI-based (May 7, 2018 to 2025) models as the primary sources of $PM_{2.5}$ estimates, while a MERRA-2-based XGBoost model fills gaps observed in TROPOMI- and OMI-based models arising from unavailability of satellite-derived predictors due to low-quality retrievals. Spatial cross-validation performance ($r \approx 0.73$–$0.76$) indicates that the XGBoost models capture dominant spatial patterns across Ghana, though prediction uncertainty may be higher in areas far from monitoring sites and have distinct emission environment, particularly in the sparsely monitored northern and central regions (Fig. S13). SHAP analysis revealed that meteorological features (primarily relative humidity), seasonal cyclic encoding, and aerosol optical indicators (UVAI and AOD) are the dominant predictors of $PM_{2.5}$ in Ghana, consistent with its $PM_{2.5}$ climatology being strongly influenced by Harmattan dust transport and wet-season aerosol scavenging.

The 21-year $PM_{2.5}$ record reveals a persistent north–south exposure disparity, with Northern Ghana consistently experiencing substantially higher $PM_{2.5}$ concentrations than the south, where mean exposure levels are typically 1.6–1.8 times greater during peak Harmattan months. This disparity is further reinforced by contrasting long-term trends. Several northern cities, including Wa, Tamale, and Nalerigu, exhibit statistically significant increases in $PM_{2.5}$ (0.05–0.11 $\mu g\ m^{-3}\ yr^{-1}$), while multiple southern urban centers, such as Somanya, Ho, and Koforidua, show measurable declines ($-0.025$ to $-0.090\ \mu g\ m^{-3}\ yr^{-1}$). These opposing trajectories suggest that national averages obtained using measurements from a few point locations obscure important regional dynamics, with air quality improving modestly in parts of the south while deteriorating in the north.

These findings carry direct implications for public-health and air-quality policy in Ghana. WHO 24-hour guideline suggests that the mean daily $PM_{2.5}$ concentrations should not exceed 15 $\mu g\ m^{-3}$ for more than 3-4 days in a year. With mean observed concentrations of 31.8 $\mu g\ m^{-3}$, and more than 99% of days during the 21-year period consistently exceeding the WHO guideline, ambient $PM_{2.5}$ in Ghana constitutes a pervasive and chronic exposure burden that extends well beyond the Harmattan season. Even during non-Harmattan months, major urban centers such as Accra,

Kumasi, and Tema exceed the higher $PM_{2.5}$ threshold from Ghana EPA 24-hour guideline (35 μg $m^{-3}$) on more than half of days during 2005–2025, indicating that combustion-driven sources contribute substantially to year-round high $PM_{2.5}$ exposure in these urban areas. The statistically significant declines detected in several southern urban centers are broadly consistent with phased improvements in vehicle fuel standards, evolving industrial emission controls, and incremental adoption of cleaner household energy, demonstrating that targeted policy levers can yield improvements in local air quality. However, these observed changes remain modest, suggesting the need for more effective policy implementation. In contrast, rising concentrations across parts of northern Ghana, where long-range mineral dust interacts with expanding biomass burning, agricultural activity, and urbanization, highlight the limits of local-only mitigation when transboundary and regional drivers dominate, and underscore the need for coordinated West African strategies and adaptive measures to reduce dry-season exposure.

Although the multi-model framework provides the most spatially and temporally complete high-resolution daily $PM_{2.5}$ dataset currently available for Ghana, characterization of diel variability is constrained by the scarcity of sub-daily observations needed to better constrain emission sources. Current satellite retrievals over Africa rely primarily on polar-orbiting instruments with once-daily overpasses. The absence of geostationary atmospheric composition satellites over the African continent, such as TEMPO, Sentinel-4, and GEMS in North America, Europe, and East Asia limits the ability to capture short-term pollution dynamics and separate anthropogenic signals from meteorological variability.

Translating this dataset into public-health and environmental-management outcomes will require several further steps. Linking the 1 km × 1 km daily $PM_{2.5}$ fields with Ghanaian health surveillance, hospitalization, and demographic and health survey data can quantify the mortality and morbidity burden attributable to long- and short-term exposures to $PM_{2.5}$, and support policy evaluation for more effective implementation and monitoring. Extending the modeling framework from Ghana to other African countries, where calibrated low-cost sensor networks are increasingly available, can be extended to generate a continental-scale high-resolution $PM_{2.5}$ record that helps close the data gaps currently constraining African representation in global air-quality and climate–health assessments. Together, these steps would transform the retrospective dataset presented here into a sustained decision-support resource for air-quality governance across data-sparse regions.

## CRediT authorship contribution statement

Conceptualization: AA, DMW. Investigation: AA, DMW. Methodology: AA, JAA, DMW. Software: DMW. Formal analysis: AA. Data curation: AA, DMW. Validation: AA, DMW. Visualization: AA. Supervision: AA, DMW. Project administration: AA, DMW. Funding acquisition: DMW. Writing—original draft: AA. Writing—review & editing: AA, JAA, SA, ENT, NABK, CA, BE, MKA, DMW.

## Declaration of competing interest

The authors declare that they have no known competing financial interests or personal relationships that could have appeared to influence the work reported in this paper.

## Acknowledgements

This work is supported by the Clean Air Fund (Grant #PG013625).

## Data and materials availability

The daily $PM_{2.5}$ gridded dataset generated from this study is publicly available on the Zenodo repository at: https://zenodo.org/records/19636051. Additional data produced and used during analysis can be found in the main text and supporting materials.

## References


Amooli, J.A., Hackman, K.O., Nana, B., Westervelt, D.M., 2024. Fine particulate air pollution estimation in Ouagadougou using satellite aerosol optical depth and meteorological parameters. Environmental Science: Atmospheres 4, 1012–1025. https://doi.org/10.1039/D4EA00057A

Amooli, J.A., Lund, M.T., Chowdhury, S., Myhre, G., Johansen, A.N., Samset, B.H., Westervelt, D.M., 2025. An uncertain future for the climate and health impacts of anthropogenic aerosols in Africa. Atmos. Chem. Phys. 25, 11611–11632. https://doi.org/10.5194/ACP-25-11611-2025

Anand, A., Touré, N.E., Bahino, J., Gnamien, S., Hughes, A.F., Arku, R.E., Tawiah, V.O., Asfaw, A., Mamo, T., Hasheminassab, S., Bililign, S., Moschos, V., Westervelt, D.M., Presto, A.A., 2024. Low-Cost Hourly Ambient Black Carbon Measurements at Multiple Cities in Africa. Environ. Sci. Technol. 58, 12575–12584. https://doi.org/10.1021/ACS.EST.4C02297/ASSET/IMAGES/LARGE/ES4C02297_0005.JPEG

Ayazpour, Z., González Abad, G., Nowlan, C.R., Sun, K., Kwon, H.A., Chan Miller, C., Chong, H., Wang, H., Liu, X., Chance, K., O'Sullivan, E., Zhu, L., Vigouroux, C., De Smedt, I., Stremme, W., Hannigan, J.W., Notholt, J., Sun, X., Palm, M., Petri, C., Strong, K., Röhling, A.N., Mahieu, E., Smale, D., Yao, T., Morino, I., Murata, I., Nagahama, T., Kivi, R., Makarova, M., Jones, N., Sussmann, R., Zhou, M., 2025. Aura Ozone Monitoring Instrument (OMI) Collection 4 Formaldehyde Products. Earth and Space Science 12, e2024EA003792. https://doi.org/10.1029/2024EA003792

Ayetor, G.K., Dugbenu, J., Duah, A.A., Adewe, C., Agyei, E.A., Affenyi, E., Peasah, G.M., Nartey, T.T., 2025. Assessing fuel economy and tailpipe emissions of road vehicles in Ghana. African Transport Studies 3, 100040. https://doi.org/10.1016/J.AFTRAN.2025.100040

Bachwenkizi, J., Liu, C., Meng, X., Zhang, L., Wang, W., van Donkelaar, A., Martin, R. V., Hammer, M.S., Chen, R., Kan, H., 2021. Fine particulate matter constituents and infant mortality in Africa: A multicountry study. Environ. Int. 156, 106739. https://doi.org/10.1016/J.ENVINT.2021.106739

Chi, G., Fang, H., Chatterjee, S., Blumenstock, J.E., 2022. Microestimates of wealth for all low- and middle-income countries. Proc. Natl. Acad. Sci. U. S. A. 119. https://doi.org/10.1073/PNAS.2113658119

De Smedt, I., Müller, J.F., Stavrakou, T., Van Der A, R., Eskes, H., Van Roozendael, M., 2008. Twelve years of global observations of formaldehyde in the troposphere using GOME and SCIAMACHY sensors. Atmos. Chem. Phys. 8, 4947–4963. https://doi.org/10.5194/ACP-8-4947-2008

Di, Q., Koutrakis, P., Schwartz, J., 2016. A hybrid prediction model for PM2.5 mass and components using a chemical transport model and land use regression. Atmos. Environ. 131, 390–399. https://doi.org/10.1016/J.ATMOSENV.2016.02.002

978 Fisher, S., Bellinger, D.C., Cropper, M.L., Kumar, P., Binagwaho, A., Koudenoukpo, J.B., Park,
979 Y., Taghian, G., Landrigan, P.J., 2021. Air pollution and development in Africa: impacts on
980 health, the economy, and human capital. Lancet Planet. Health 5, e681–e688.
981 https://doi.org/10.1016/S2542-5196(21)00201-1

982 Griffin, D., Chen, J., Anderson, K., Makar, P., McLinden, C.A., Dammers, E., Fogal, A., 2024.
983 Biomass burning CO emissions: exploring insights through TROPOMI-derived emissions
984 and emission coefficients. Atmos. Chem. Phys. 24, 10159–10186.
985 https://doi.org/10.5194/ACP-24-10159-2024

986 Gualtieri, G., Ahbil, K., Brilli, L., Carotenuto, F., Cavaliere, A., Gioli, B., Giordano, T., Katiellou,
987 G.L., Mouhaimini, M., Tarchiani, V., Vagnoli, C., Zaldei, A., Bacci, M., 2024. Potential of
988 low-cost PM monitoring sensors to fill monitoring gaps in areas of Sub-Saharan Africa.
989 Atmos. Pollut. Res. 15, 102158. https://doi.org/10.1016/J.APR.2024.102158

990 Hammer, M.S., Van Donkelaar, A., Li, C., Lyapustin, A., Sayer, A.M., Hsu, N.C., Levy, R.C.,
991 Garay, M.J., Kalashnikova, O. V., Kahn, R.A., Brauer, M., Apte, J.S., Henze, D.K., Zhang,
992 L., Zhang, Q., Ford, B., Pierce, J.R., Martin, R. V., 2020. Global Estimates and Long-Term
993 Trends of Fine Particulate Matter Concentrations (1998-2018). Environ. Sci. Technol. 54,
994 7879–7890. https://doi.org/10.1021/ACS.EST.0C01764

995 Hayes, R.B., Lim, C., Zhang, Y., Cromar, K., Shao, Y., Reynolds, H.R., Silverman, D.T., Jones,
996 R.R., Park, Y., Jerrett, M., Ahn, J., Thurston, G.D., 2020. PM2.5 air pollution and cause-
997 specific cardiovascular disease mortality. Int. J. Epidemiol. 49, 25–35.
998 https://doi.org/10.1093/IJE/DYZ114

999 Hirsch, R.M., Slack, J.R., 1984. A Nonparametric Trend Test for Seasonal Data With Serial
1000 Dependence. Water Resour. Res. 20, 727–732. https://doi.org/10.1029/WR020I006P00727

1001 Kendall, M.G., 1975. Rank Correlation Methods (4th ed.).

1002 Klutse, N.A.B., Owusu, K., Boafo, Y.A., 2020. Projected temperature increases over northern
1003 Ghana. SN Appl. Sci. 2, 1339-. https://doi.org/10.1007/S42452-020-3095-3/FIGURES/8

1004 Lebakula, V., Sims, K., Reith, A., Rose, A., McKee, J., Coleman, P., Kaufman, J., Urban, M.,
1005 Jochem, C., Whitlock, C., Ogden, M., Pyle, J., Roddy, D., Epting, J., Bright, E., 2025.
1006 LandScan Global 30 Arcsecond Annual Global Gridded Population Datasets from 2000 to
1007 2022. Scientific Data 2025 12:1 12, 495-. https://doi.org/10.1038/s41597-025-04817-z

1008 Li, C., Joiner, J., Krotkov, N.A., Bhartia, P.K., 2013. A fast and sensitive new satellite SO2
1009 retrieval algorithm based on principal component analysis: Application to the ozone
1010 monitoring instrument. Geophys. Res. Lett. 40, 6314–6318.
1011 https://doi.org/10.1002/2013GL058134

1012 Li, C., Wang, J., Zhang, H., Diner, D.J., Hasheminassab, S., Janechek, N., 2024. Improvement of
1013 Surface PM 2.5 Diurnal Variation Simulations in East Africa for the MAIA Satellite Mission
1014 . ACS ES&T Air 1, 223–233.

https://doi.org/10.1021/ACSESTAIR.3C00008/ASSET/IMAGES/LARGE/EA3C00008_0005.JPEG

Liu, Y., Park, Rokjin J, Jacob, Daniel J, Li, Qinbin, Kilaru, Vasu, Sarnat, Jeremy A, Liu, C.:, Park, R J, Jacob, D J, Li, Q, Kilaru, V, Sarnat, J A, 2004. Mapping annual mean ground-level PM2.5 concentrations using Multiangle Imaging Spectroradiometer aerosol optical thickness over the contiguous United States. Journal of Geophysical Research: Atmospheres 109, 1–10. https://doi.org/10.1029/2004JD005025

Lyapustin, A., Wang, Y., Korkin, S., Huang, D., 2018. MODIS Collection 6 MAIAC algorithm. Atmos. Meas. Tech. 11, 5741–5765. https://doi.org/10.5194/AMT-11-5741-2018

Mann, H.B., 1945. Nonparametric Tests Against Trend. Econometrica 13, 245. https://doi.org/10.2307/1907187

Muñoz-Sabater, J., Dutra, E., Agustí-Panareda, A., Albergel, C., Arduini, G., Balsamo, G., Boussetta, S., Choulga, M., Harrigan, S., Hersbach, H., Martens, B., Miralles, D.G., Piles, M., Rodríguez-Fernández, N.J., Zsoter, E., Buontempo, C., Thépaut, J.N., 2021. ERA5-Land: A state-of-the-art global reanalysis dataset for land applications. Earth Syst. Sci. Data 13, 4349–4383. https://doi.org/10.5194/ESSD-13-4349-2021

Nicholson, S.E., 2018. The ITCZ and the Seasonal Cycle over Equatorial Africa. Bull. Am. Meteorol. Soc. 99, 337–348. https://doi.org/10.1175/BAMS-D-16-0287.1

Ofosu, F.G., Hopke, P.K., Aboh, I.J.K., Bamford, S.A., 2013. Biomass burning contribution to ambient air particulate levels at Navrongo in the Savannah zone of Ghana. J. Air Waste Manage. Assoc. 63, 1036–1045. https://doi.org/10.1080/10962247.2013.783888

Owusu-Tawiah, V., Annor, T., Yamba, E.I., Nimo, J., Wemegah, C.S., Hodoli, C.G., Osei-Tutu, D., Amponsah, D., Hughes, A.F., Westervelt, D.M., 2025. Spatiotemporal Assessment of PM2.5 in Senior High Schools in Kumasi, Ghana using Low-Cost Sensors. Aerosol Air Qual. Res. 25, 66-. https://doi.org/10.1007/S44408-025-00066-2/FIGURES/9

Philip, S., Martin, R. V., Van Donkelaar, A., Lo, J.W.H., Wang, Y., Chen, D., Zhang, L., Kasibhatla, P.S., Wang, S., Zhang, Q., Lu, Z., Streets, D.G., Bittman, S., Macdonald, D.J., 2014. Global chemical composition of ambient fine particulate matter for exposure assessment. Environ. Sci. Technol. 48, 13060–13068. https://doi.org/10.1021/ES502965B

Pye, H.O.T., Appel, K.W., Seltzer, K.M., Ward-Caviness, C.K., Murphy, B.N., 2022. Human-Health Impacts of Controlling Secondary Air Pollution Precursors. Environ. Sci. Technol. Lett. 9, 96–101. https://doi.org/10.1021/ACS.ESTLETT.1C00798/ASSET/IMAGES/LARGE/EZ1C00798_0003.JPEG

Raheja, G., Sabi, K., Sonla, H., Gbedjangni, E.K., McFarlane, C.M., Hodoli, C.G., Westervelt, D.M., 2022. A Network of Field-Calibrated Low-Cost Sensor Measurements of PM2.5in Lomé, Togo, Over One to Two Years. ACS Earth Space Chem. 6, 1011–1021.

https://doi.org/10.1021/ACSEARTHSPACECHEM.1C00391/ASSET/IMAGES/LARGE/SP1C00391_0008.JPEG

Sayeed, A., Lin, P., Gupta, P., Tran, N.N.M., Buchard, V., Christopher, S., 2022. Hourly and Daily PM2.5 Estimations Using MERRA-2: A Machine Learning Approach. Earth and Space Science 9, e2022EA002375. https://doi.org/10.1029/2022EA002375

Sen, P.K., 1968. Estimates of the Regression Coefficient Based on Kendall's Tau. J. Am. Stat. Assoc. 63, 1379–1389. https://doi.org/10.1080/01621459.1968.10480934

Shi, L., Wu, X., Danesh Yazdi, M., Braun, D., Abu Awad, Y., Wei, Y., Liu, P., Di, Q., Wang, Y., Schwartz, J., Dominici, F., Kioumourtzoglou, M.A., Zanobetti, A., 2020. Long-term effects of PM2·5 on neurological disorders in the American Medicare population: a longitudinal cohort study. Lancet Planet. Health 4, e557–e565. https://doi.org/10.1016/S2542-5196(20)30227-8

Health Effects Institute, 2024. State of Global Air Report 2024 | State of Global Air [WWW Document]. URL https://www.stateofglobalair.org/resources/report/state-global-air-report-2024 (accessed 6.29.25).

Torres, O., Bhartia, P.K., Jethva, H., Ahn, C., 2018. Impact of the ozone monitoring instrument row anomaly on the long-term record of aerosol products. Atmos. Meas. Tech. 11, 2701–2715. https://doi.org/10.5194/AMT-11-2701-2018

Torres, O., Jethva, H., Ahn, C., Jaross, G., Loyola, D.G., 2020. TROPOMI aerosol products: Evaluation and observations of synoptic-scale carbonaceous aerosol plumes during 2018-2020. Atmos. Meas. Tech. 13, 6789–6806. https://doi.org/10.5194/AMT-13-6789-2020

Van Donkelaar, A., Hammer, M.S., Bindle, L., Brauer, M., Brook, J.R., Garay, M.J., Hsu, N.C., Kalashnikova, O. V., Kahn, R.A., Lee, C., Levy, R.C., Lyapustin, A., Sayer, A.M., Martin, R. V., 2021. Monthly Global Estimates of Fine Particulate Matter and Their Uncertainty. Environ. Sci. Technol. 55, 15287–15300. https://doi.org/10.1021/ACS.EST.1C05309/ASSET/IMAGES/LARGE/ES1C05309_0007.JPEG

Van Donkelaar, A., Martin, R. V, Brauer, M., Hsu, N.C., Kahn, R.A., Levy, R.C., Lyapustin, A., Sayer, A.M., Winker, D.M., 2016. Global Estimates of Fine Particulate Matter using a Combined Geophysical-Statistical Method with Information from Satellites, Models, and Monitors. Environ. Sci. Technol. https://doi.org/10.1021/acs.est.5b05833

Van Donkelaar, A., Martin, R. V., Park, R.J., 2006. Estimating ground-level PM2.5 using aerosol optical depth determined from satellite remote sensing. Journal of Geophysical Research: Atmospheres 111, 21201. https://doi.org/10.1029/2005JD006996

Van Geffen, J., Eskes, H., Compernolle, S., Pinardi, G., Verhoelst, T., Lambert, J.C., Sneep, M., Linden, M. Ter, Ludewig, A., Folkert Boersma, K., Pepijn Veefkind, J., 2022. Sentinel-5P TROPOMI NO2retrieval: impact of version v2.2 improvements and comparisons with OMI

and ground-based data. Atmos. Meas. Tech. 15, 2037–2060. https://doi.org/10.5194/AMT-15-2037-2022

Veefkind, J.P., Aben, I., McMullan, K., Förster, H., de Vries, J., Otter, G., Claas, J., Eskes, H.J., de Haan, J.F., Kleipool, Q., van Weele, M., Hasekamp, O., Hoogeveen, R., Landgraf, J., Snel, R., Tol, P., Ingmann, P., Voors, R., Kruizinga, B., Vink, R., Visser, H., Levelt, P.F., 2012. TROPOMI on the ESA Sentinel-5 Precursor: A GMES mission for global observations of the atmospheric composition for climate, air quality and ozone layer applications. Remote Sens. Environ. 120, 70–83. https://doi.org/10.1016/J.RSE.2011.09.027

Vohra, K., Vodonos, A., Schwartz, J., Marais, E.A., Sulprizio, M.P., Mickley, L.J., 2021. Global mortality from outdoor fine particle pollution generated by fossil fuel combustion: Results from GEOS-Chem. Environ. Res. 195, 110754. https://doi.org/10.1016/J.ENVRES.2021.110754

Weagle, C.L., Snider, G., Li, C., Van Donkelaar, A., Philip, S., Bissonnette, P., Burke, J., Jackson, J., Latimer, R., Stone, E., Abboud, I., Akoshile, C., Anh, N.X., Brook, J.R., Cohen, A., Dong, J., Gibson, M.D., Griffith, D., He, K.B., Holben, B.N., Kahn, R., Keller, C.A., Kim, J.S., Lagrosas, N., Lestari, P., Khian, Y.L., Liu, Y., Marais, E.A., Martins, J.V., Misra, A., Muliane, U., Pratiwi, R., Quel, E.J., Salam, A., Segev, L., Tripathi, S.N., Wang, C., Zhang, Q., Brauer, M., Rudich, Y., Martin, R. V., 2018. Global Sources of Fine Particulate Matter: Interpretation of PM 2.5 Chemical Composition Observed by SPARTAN using a Global Chemical Transport Model. Environ. Sci. Technol. 52, 11670–11681. https://doi.org/10.1021/ACS.EST.8B01658

Westervelt, D.M., Amooli, J.A., Anand, A., 2025. Twenty Years of High Spatiotemporal Resolution Estimates of Daily PM2.5 in West Africa Using Satellite Data, Surface Monitors, and Machine Learning. ACS ES&T Air 2, 1468–1477. https://doi.org/10.1021/ACSESTAIR.4C00366

Westervelt, D.M., Isevulambire, P.K., Phaka, R.Y., Yang, L.H., Raheja, G., Milly, G., Selenge, J.-L.B., Mulumba, J.P.M., Bousiotis, D., Djibi, B.L., McNeill, V.F., Ng, N.L., Pope, F., Mbela, G.K., Konde, J.N., 2023. Low-Cost Investigation into Sources of PM2.5 in Kinshasa, Democratic Republic of the Congo. ACS ES&T Air 1, 43–51. https://doi.org/10.1021/ACSESTAIR.3C00024

World Meteorological Organization (WMO), 2008. Guide to Instruments and Methods of Observation (WMO-No. 8), Seventh Edition. ed.

Zhang, D., Du, L., Wang, W., Zhu, Q., Bi, J., Scovronick, N., Naidoo, M., Garland, R.M., Liu, Y., 2021. A machine learning model to estimate ambient PM2.5 concentrations in industrialized highveld region of South Africa. Remote Sens. Environ. 266, 112713. https://doi.org/10.1016/J.RSE.2021.112713

Zheng, Z., Fiore, A.M., Westervelt, D.M., Milly, G.P., Goldsmith, J., Karambelas, A., Curci, G., Randles, C.A., Paiva, A.R., Wang, C., Wu, Q., Dey, S., 2023. Automated Machine Learning to Evaluate the Information Content of Tropospheric Trace Gas Columns for Fine Particle

Estimates Over India: A Modeling Testbed. J. Adv. Model. Earth Syst. 15, e2022MS003099. https://doi.org/10.1029/2022MS003099

**Supplementary Materials**

This PDF file includes:

Supplementary Text S1 to S2

Figures S1 to S18

Tables S1 to S11

**Supplementary Materials**

# Two decades of kilometer-scale daily $PM_{2.5}$ from satellite observations and machine learning reveal geographically diverging exposure in Ghana

Abhishek Anand[a*], Joe A. Amooli[a,b], Selina Amoah[c], Esi Nerquaye Tetteh[c], Nana Ama Browne Klutse[c], Clement Ackaah[c], Benjamin Essien[c], Kingsley Mawuli Amegah[c], Daniel M. Westervelt[a,b]

[a]Lamont-Doherty Earth Observatory, Columbia University, Palisades, NY, USA

[b]Department of Earth and Environmental Sciences, Columbia University, New York, NY, USA

[c]Ghana Environmental Protection Authority, Accra, Ghana

*Corresponding author: abhishek.anand@columbia.edu

**Summary of the Supplementary Materials**

Number of pages: 34

Figures: S1 – S18

Tables: S1 – S11

**Table S1.** Technical specifications of particulate monitors deployed in Ghana.

| **Sensor type** | **Relevant measurement variables** | **Measurement frequency** | **Operating $PM_{2.5}$ range ($\mu g\ m^{-3}$)** |
|---|---|---|---|
| Airnote v2.0 | $PM_{2.5}$, T, RH | 1 min | 0–1000 |
| BAM | $PM_{2.5}$, T, RH | 1 hr | 0–10,000 |
| Clarity Node-S (Generation II) | $PM_{2.5}$, T, RH | 1 min | 0–1000 |
| PA-II SD | $PM_{2.5}$, T, RH | 2 min | 0–1000 |
| MODULAIR-PM | $PM_{2.5}$, T, RH | 1 min | 0–2000 |

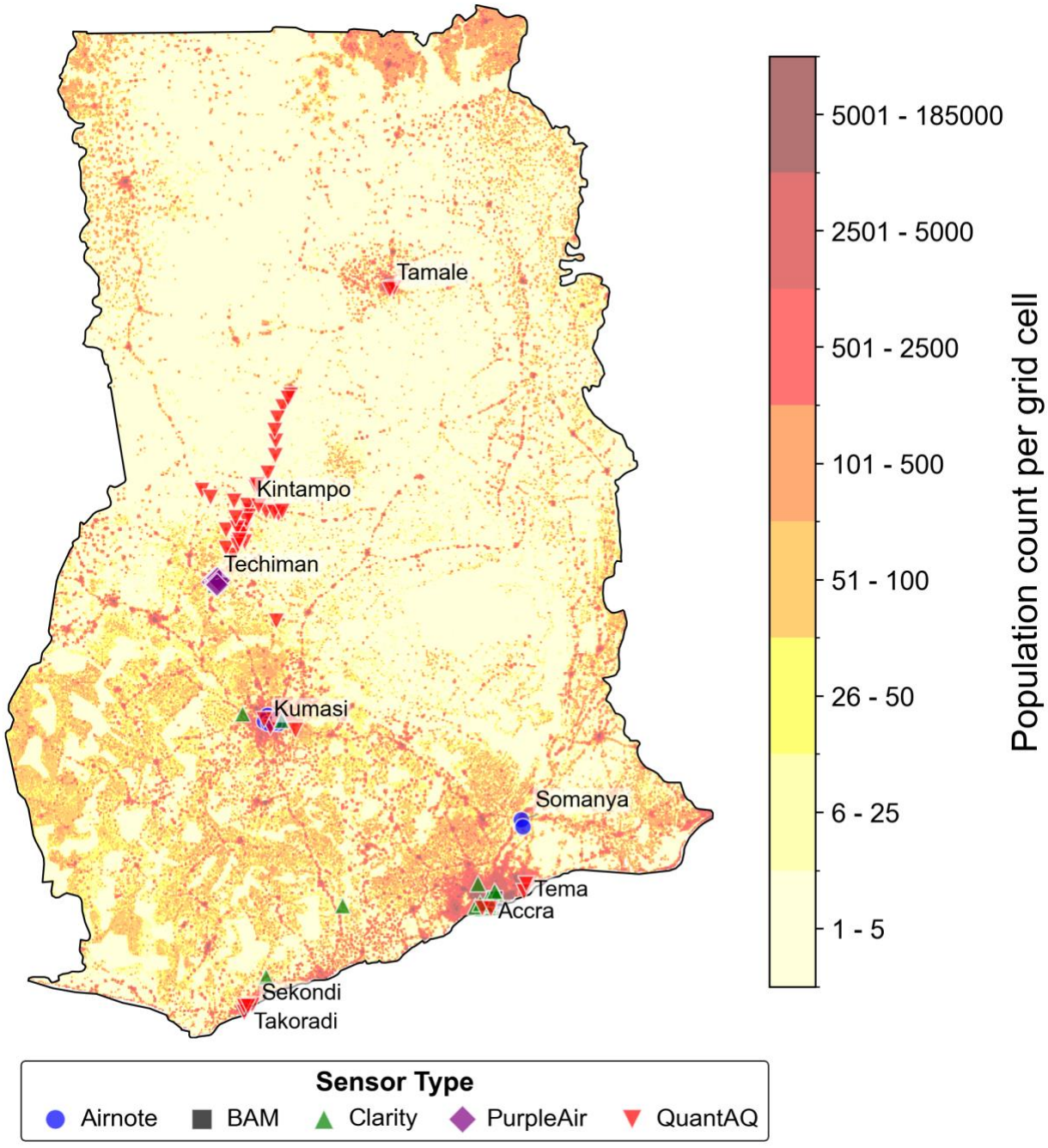


**Fig. S1.** Map of sensor locations. A map of Ghana showing the locations and counts of all surface $PM_{2.5}$ monitors and the population density for 2024 from the LandScan Program at Oak Ridge National Lab (Lebakula et al., 2025). The darker regions indicate higher population density.

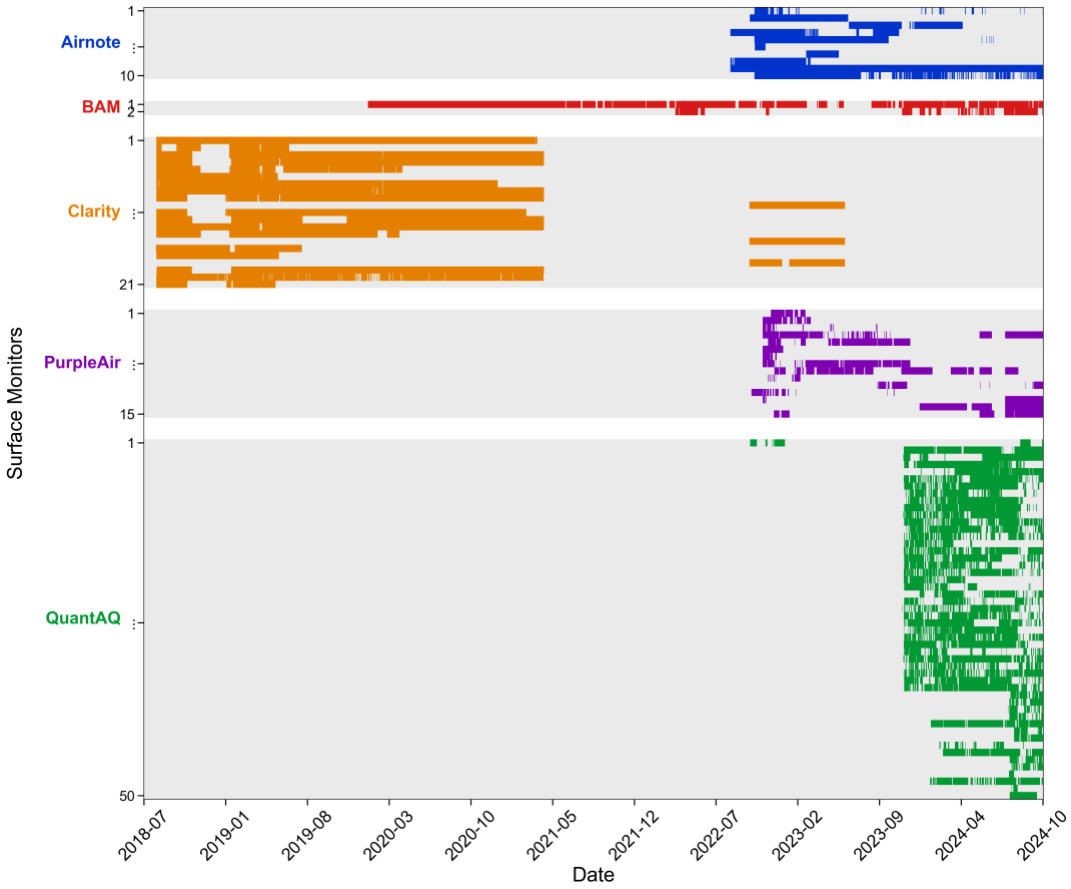


**Fig. S2.** Availability of $PM_{2.5}$ measurements from 98 surface monitors used as ground truth for building the GRASP model. Y-axis represents different sensor types and their corresponding numbers.

**Table S2.** Summary of sensor locations, location types and corresponding counts in Ghana.

| **Location** | **Location type** | **Sensor count** |
|---|---|---|
| Accra | Urban | 20 |
| Kintampo | Rural | 35 |
| Kumasi | Urban | 13 |
| Nyamibechire | Peri-urban | 1 |
| Sekondi | Urban | 1 |
| Somanya | Peri-urban | 3 |
| Supomu Dunkwa | Peri-urban | 1 |
| Takoradi | Urban | 3 |
| Tamale | Urban | 3 |
| Techiman | Peri-urban | 16 |
| Tema | Urban | 2 |

**Table S3.** Summary of total and location-aggregated counts for each sensor types used in Ghana.

| **Sensor types** | **Count** | **Locations** |
|---|---|---|
| Airnote | 10 | Kumasi (7)<br>Somanya (3) |
| BAM | 2 | Accra (1)<br>Techiman (1) |
| Clarity | 21 | Accra (17)<br>Kumasi (2)<br>Nyamibechire (1)<br>Supomu Dunkwa (1) |
| PurpleAir | 15 | Techiman (15) |
| QuantAQ | 50 | Accra (2)<br>Kintampo (35)<br>Kumasi (4)<br>Sekondi (1)<br>Takoradi (3)<br>Tamale (3)<br>Tema (2) |

**Text S1. Calibration of $PM_{2.5}$ measurements from low-cost sensors**

Each of the low-cost sensors (Airnote, Clarity, PurpleAir and QuantAQ) in the surface monitoring network were calibrated collocating either with a BAM or other BAM-corrected low-cost monitors in the network. The corrected $PM_{2.5}$ concentrations were calculated as follow.

$$PM_{2.5,\ corrected} = f(PM_{2.5,\ raw}, T, RH) \ldots (S1)$$

where $PM_{2.5,\ raw}$, T and RH denote raw measurements of $PM_{2.5}$, temperature (in ºC) and relative humidity (in %) collected by a low-cost sensor. $PM_{2.5,}$ corrected represents the quality-assured/quality-controlled (QA/QC) $PM_{2.5}$ concentrations retrieved from calibration algorithms.

***Airnote***

Airnote sensors were mainly deployed in Kumasi (urban) and Somanya (peri-urban). The raw $PM_{2.5}$ concentrations, temperature and relative humidity measured by Airnote sensors were used to develop a multiple linear regression (MLR) model to estimate corrected $PM_{2.5}$ levels (Owusu-Tawiah et al., 2025).

$$PM_{2.5,\ corrected} = -6.6 + 0.57*PM_{2.5,\ raw} + 0.28*T + 0.03*RH \ldots (S2)$$

***Clarity***

Majority of Clarity sensors are located in Accra and a few in Kumasi, Supomu Dunkwa and Nyamibechire. A MLR algorithm was developed using BAM located at Accra US Embassy as reference monitor (Raheja et al., 2023).

$$PM_{2.5,\ corrected} = 54.60 + 0.4*PM_{2.5,\ raw} - 0.76*T - 0.35*RH \ldots (S3)$$

***PurpleAir***

All PA-II SD sensors were deployed in Techiman. Each PurpleAir sensor consists of two identical Laser Particle Counters (PMS-5003, PlanTower, Beijing, China) to measure $PM_{2.5}$, named channel A and B. A BME280 sensor (Bosch, Gerlingen, Germany) measures pressure, temperature and humidity sensor which can be used for calibrating the raw $PM_{2.5}$ measurements. We applied three filtering criteria to include only valid data points in the analysis: (1) a $PM_{2.5}$ threshold for both channels to 1000 $\mu g\ m^3$ and discarded datapoints with $PM_{2.5}$ higher than the threshold to comply with the manufacturer recommendation, (2) keep only rows with valid entry in temperature, humidity and $PM_{2.5}$ concentrations from the two channels, and (3) retains rows where relative percentage difference in $PM_{2.5}$, defined as $2*100*|PM_{2.5,\ A} - PM_{2.5,B}|/(PM_{2.5,\ A} + PM_{2.5,B})$, is $\leq 25\%$ , which neglects datapoints with large differences in $PM_{2.5}$ readings from the two channels mostly attributed to ageing of either or both laser particle counters or their clogging due to accumulation of dust or insects.

The $PM_{2.5}$ measurements from Techiman BAM was used as ground-truth for calibrating PurpleAir-based $PM_{2.5}$ concentrations. A PurpleAir sensor within the Techiman network located at ~500m to the BAM was selected for model development due to its closest proximity to the BAM. An eXtreme Gradient Boosting (XGB) model was developed to derive corrected $PM_{2.5}$.

$$PM_{2.5,\ XGB\text{-}corrected} = f(\text{Mean } PM_{2.5,\ raw}, T, RH) \quad \ldots(S4)$$

where, Mean $PM_{2.5,\ raw}$, is the average of raw $PM_{2.5}$ measurements from channels A and B. $PM_{2.5,XGB\text{-}corrected}$ represents model corrected $PM_{2.5}$. This model is further used to corrected $PM_{2.5}$ outputs from the rest of the PurpleAir sensors in the Techiman network.

***QuantAQ***

MODULAIR-PM reports manufacturer-built correction applied $PM_{2.5}$ that accounts for particle density, aspiration efficiency, and hygroscopic growth. These measurements have shown strong correlation to reference measurements and perform comparable to regression and machine learning algorithms developed for operating in specifically for deployed environment (Raheja et al., 2023). Therefore, the $PM_{2.5}$ measurements reported by the MODULAIR monitors in the network were directly used for model development.

**Table S4.** Quality screening of satellite-derived products. A summary of satellite-derived products and corresponding QA criteria to generate high-quality retrievals.

| **Parameters** | **Satellite product (*ID*)** | **QA layers and criteria** |
|---|---|---|
| AOD at 550 nm (MODIS MAIAC) | AOD (*MCD19A2*) | *AOD_QA* ϵ {0000, 0011, 1011} (*AOD_QA* is a 16-bit unsigned integer.) |
| OMI (Level 2, Collection 3) | UVAI (*OMAERUV v003*) | *CloudFraction* ≤ 0.3<br>*SolarZenithAngle* ≤ 75º<br>*XTrackQualityFlags* = 0 |
| | HCHO (*OMHCHO v003*) | *AMFCloudFraction* ≤ 0.3<br>*SolarZenithAngle* ≤ 75º<br>*XTrackQualityFlags* = 0<br>*MainDataQualityFlag* = 0 |
| | $O_3$ (*OMTO3 v003*) | *RadiativeCloudFraction* ≤ 0.3<br>*SolarZenithAngle* ≤ 85º<br>*QualityFlags* ≤ 1 |
| | $NO_2$ (*OMNO2 v003*) | *CloudFraction* ≤ 0.3<br>*SolarZenithAngle* ≤ 75º<br>*VcdQualityFlags* = 0 |
| | $SO_2$ (*OMSO2 v003*) | *CloudRadiationFraction* ≤ 0.3<br>*SolarZenithAngle* ≤ 65º<br>*Flag_RowAnomaly* ≠ 1<br>*Flag_SAA* ≠ 1<br>*AlgorithmFlag_SnowIce* ≠ 2 |
| TROPOMI (Level 2, Collection 2) | UVAI *(S5P_L2__AER_AI_HiR v2)* | *qa_value* ≥ 0.5 |
| | HCHO *(S5P_L2__HCHO___HiR v2)* | |
| | $O_3$ *(S5P_L2__O3_TOT_HiR v2)* | |
| | $NO_2$ *(S5P_L2__NO2____HiR v2)* | |
| | $SO_2$ *(S5P_L2__SO2____HiR v2)* | |

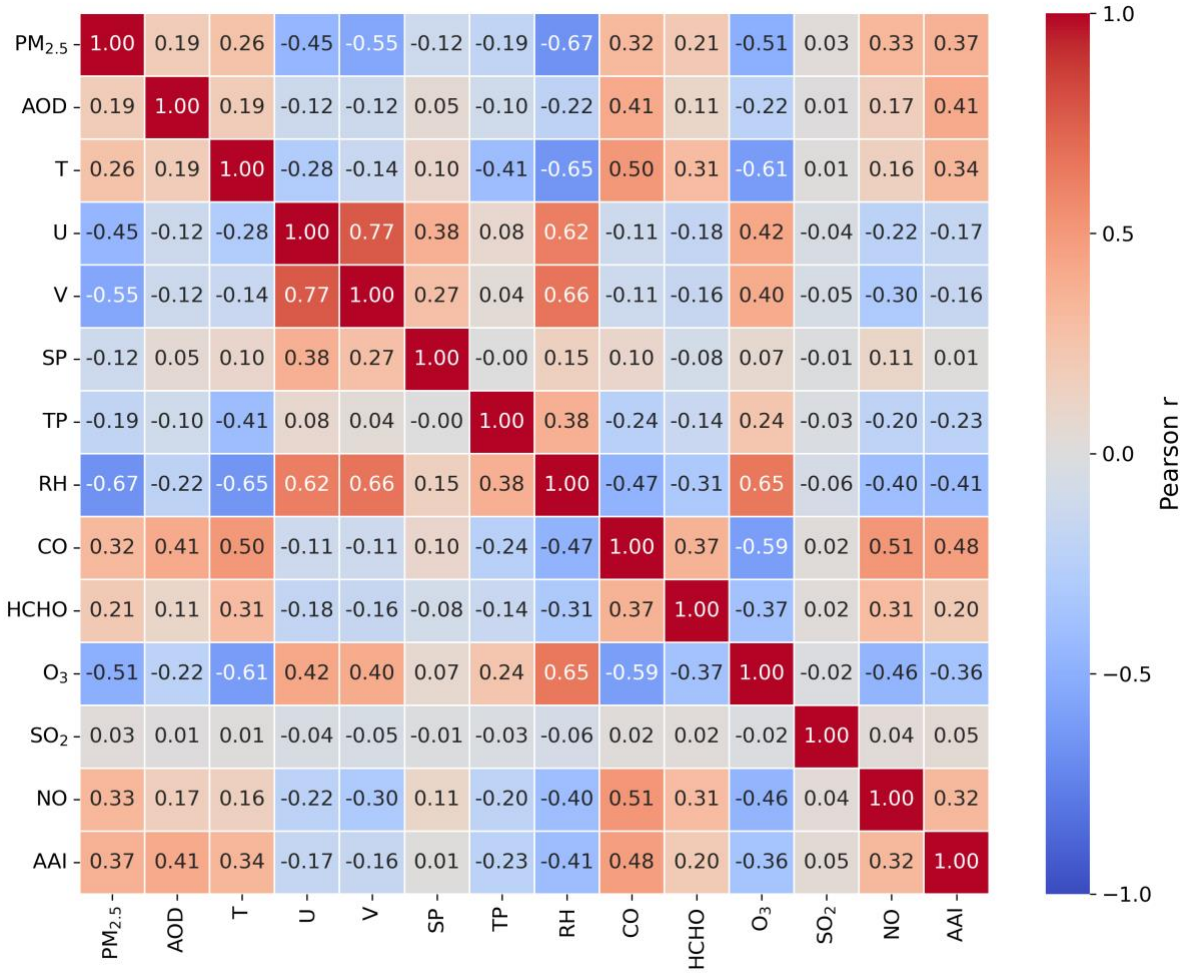


**Fig. S3.** Correlation between training features used in TROPOMI model. Pearson correlation matrix of $PM_{2.5}$, meteorological (ERA5), and satellite-derived (MODIS and TROPOMI) variables used in the modeling framework. Color intensity represents the strength and direction of linear correlations, ranging from −1 (strong negative correlation) to +1 (strong positive correlation).

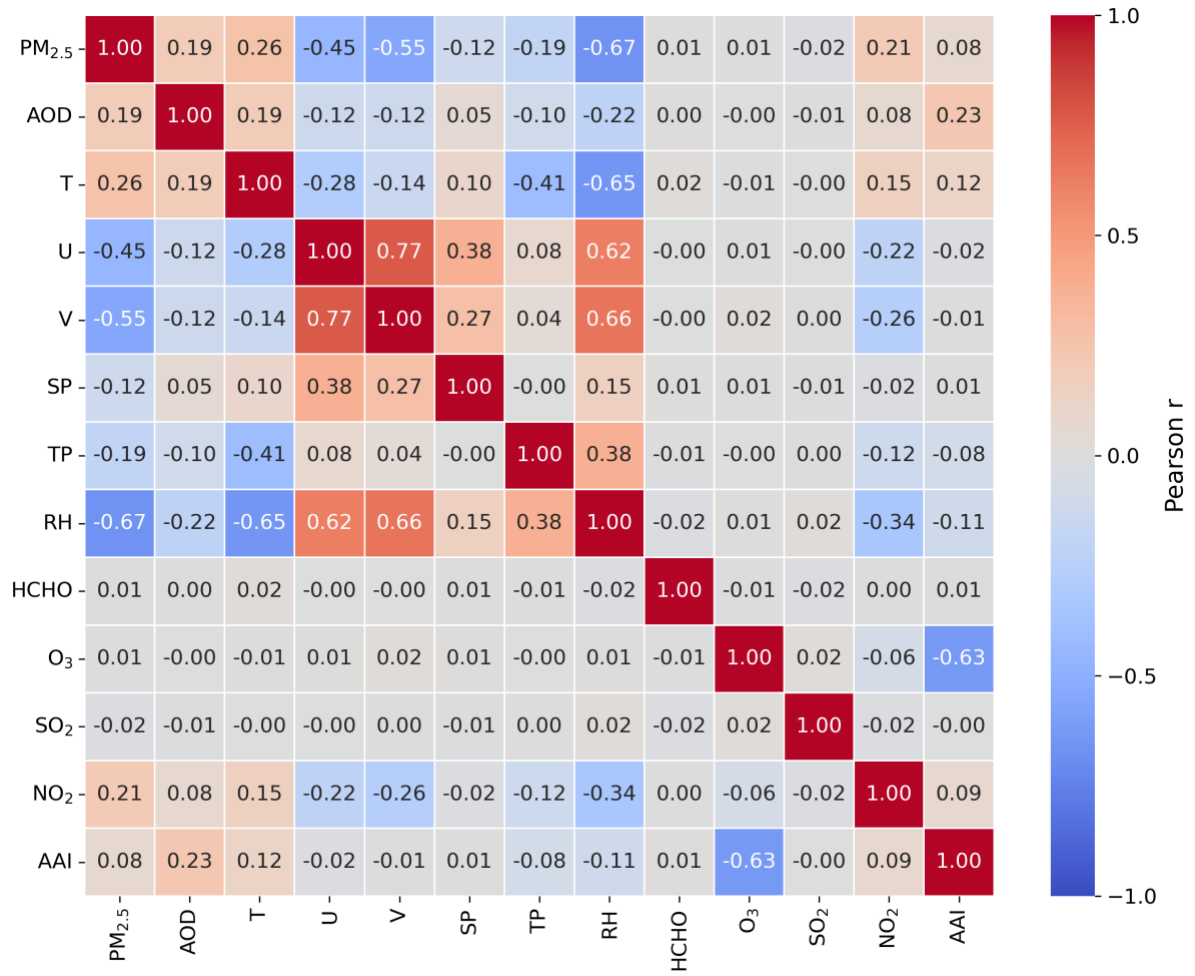


**Fig. S4.** Correlation between training features used in OMI model. Pearson correlation matrix of $PM_{2.5}$, meteorological (ERA5), and satellite-derived (MODIS and OMI) variables used in the modeling framework. Color intensity represents the strength and direction of linear correlations, ranging from −1 (strong negative correlation) to +1 (strong positive correlation).

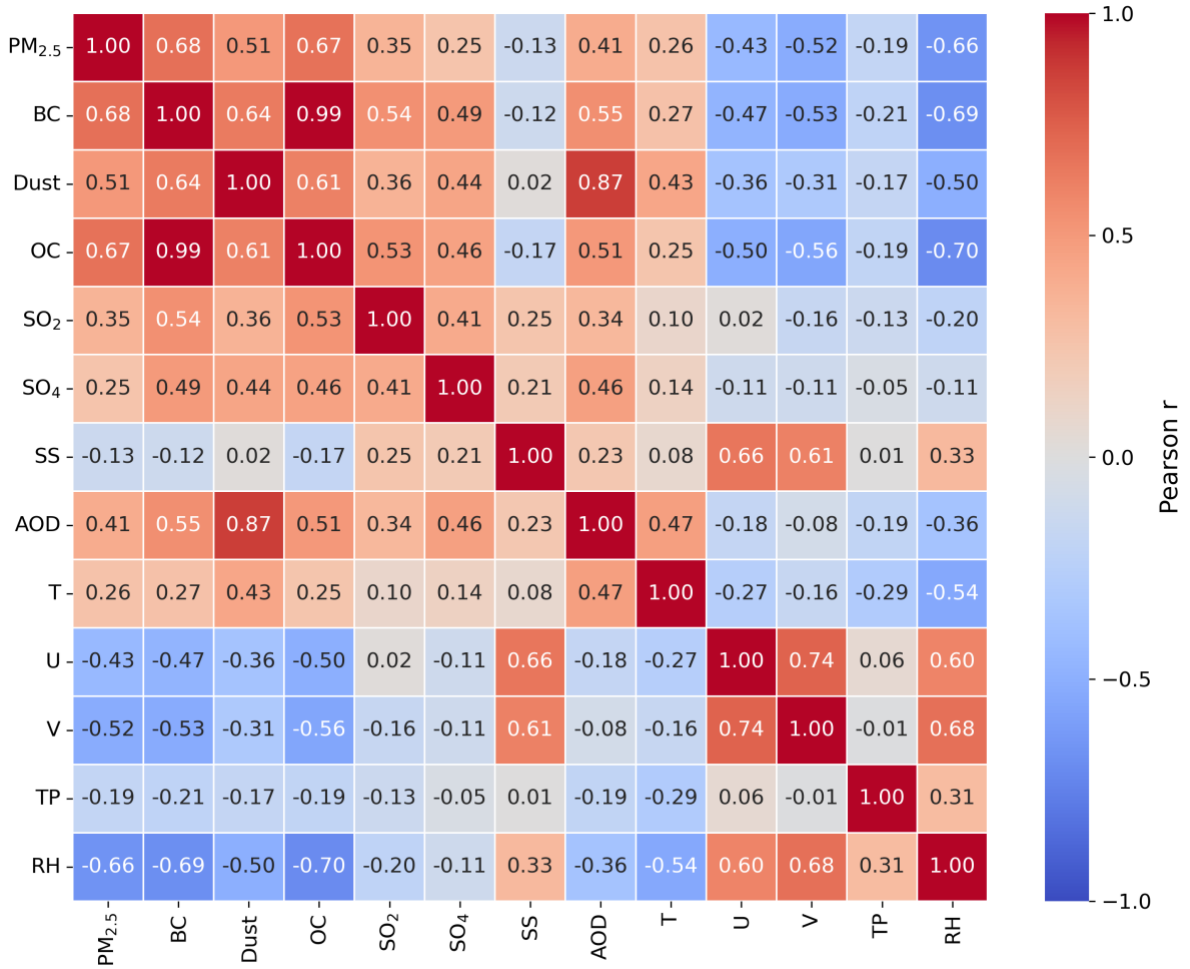


**Fig. S5.** Correlation between training features used in MERRA2-based model. Pearson correlation matrix of $PM_{2.5}$, meteorological (ERA5), and MERRA-2 reanalysis variables used in the modeling framework. Color intensity represents the strength and direction of linear correlations, ranging from −1 (strong negative correlation) to +1 (strong positive correlation).

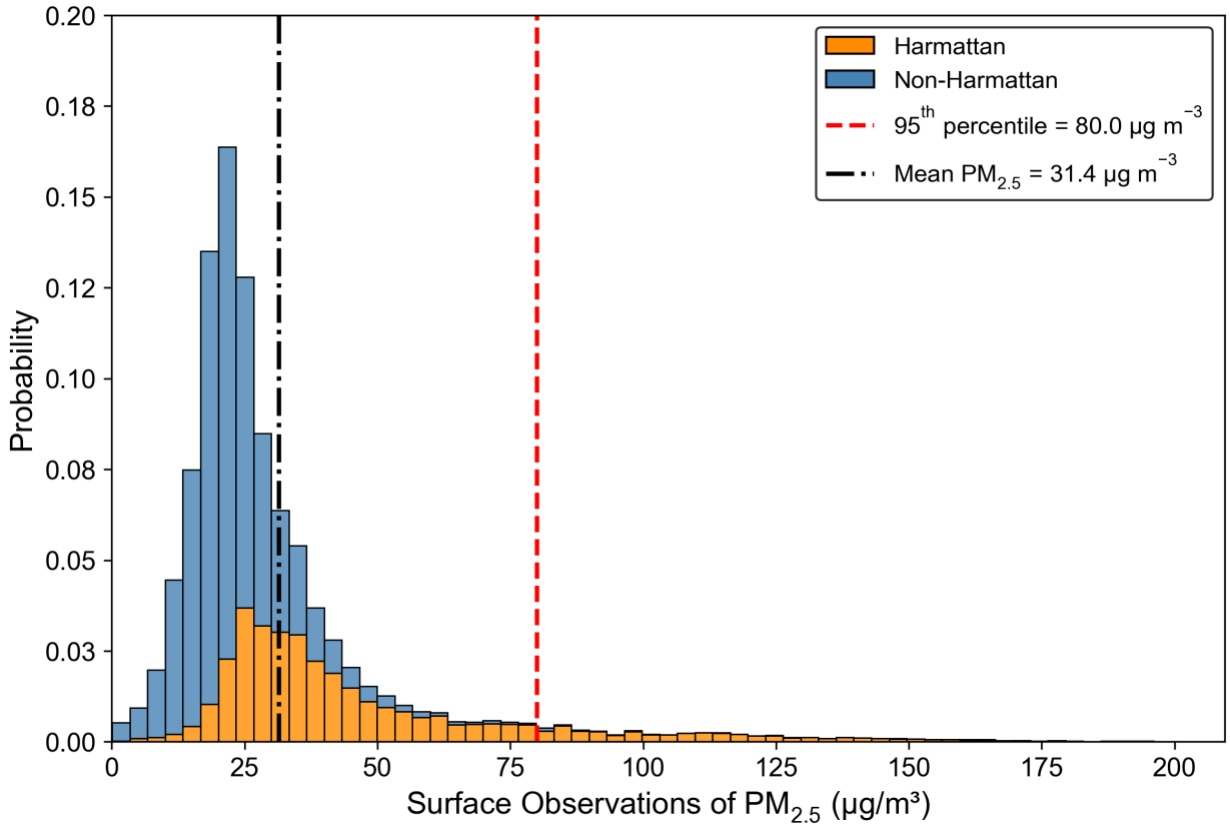


**Fig. S6.** Surface $PM_{2.5}$ measurements from ground monitors. Probability distribution of surface-observed $PM_{2.5}$ concentrations (µg $m^{-3}$) stratified into Harmattan (orange) and non-Harmattan (blue) periods. The histogram represents the relative frequency of observations, where the red dashed vertical line indicates the 95$^{th}$ percentile (80 µg $m^{-3}$) and black dash-dotted line denotes the mean concentration (31.4 µg $m^{-3}$). The distribution is positively skewed, with most observations concentrated at lower concentrations and a long tail toward higher pollution events.

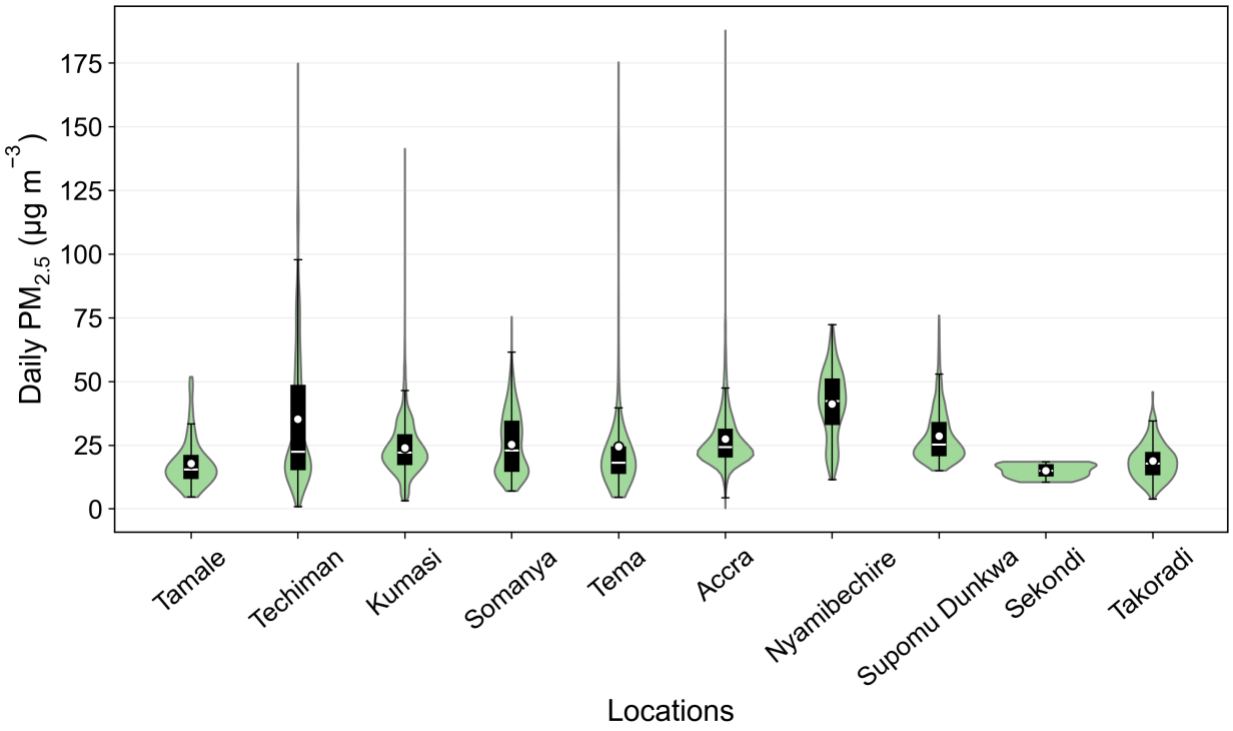


**Fig. S7.** Violin plots of mean daily $PM_{2.5}$ concentrations measured by ground-based sensors across all study locations in Ghana. Each violin represents the kernel density of daily $PM_{2.5}$ for a location. Embedded boxplots display the median (white horizontal line), mean (white solid circle), and interquartile range (IQR). Whiskers extend to 1.5 × IQR, and values beyond the whiskers are considered outliers.

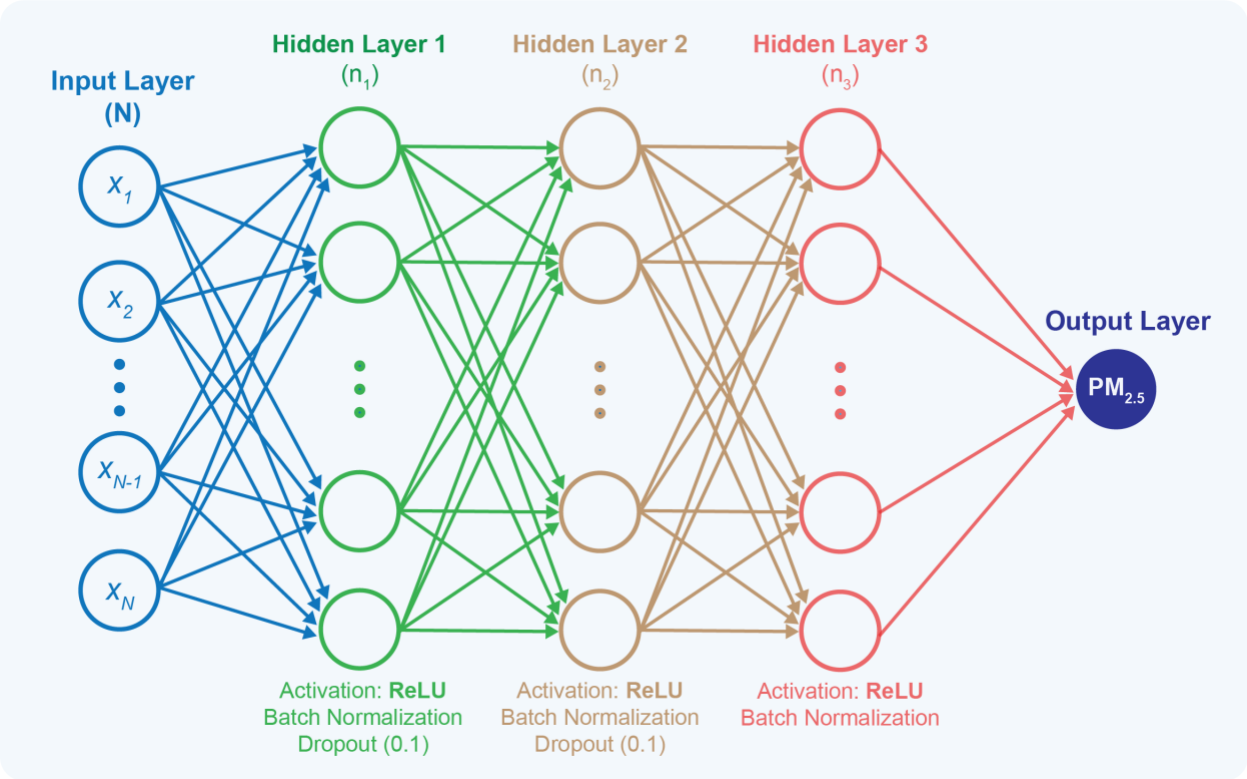


**Fig. S8.** Architecture of the multilayer perceptron (MLP) model used for $PM_{2.5}$ prediction. The MLP consists of an input layer with $N$ predictor variables ($X_1, X_2, \ldots, X_N$). The input layer is followed by three fully connected hidden layers containing $n_1$, $n_2$, and $n_3$ nodes, respectively. Each hidden layer applies a ReLU activation function and batch normalization, while dropout (0.1) is applied to the first two hidden layers to reduce overfitting. The output layer contains a single neuron that produces continuous $PM_{2.5}$ concentrations using a linear activation function. The number of nodes in each hidden layer varies across tested model configurations and is summarized in Tables S5 to S7.

**Table S5.** Optimized hyperparameters for TROPOMI model. Final tuned hyperparameter values for each machine learning model trained for TROPOMI model of the multi-model framework.

| **Model** | **Optimized hyperparameters** |
|---|---|
| LASSO | *{'regressor__alpha': 0.01}* |
| SVM | *{'regressor__C': 100,*<br>*'regressor__epsilon': 0.2,*<br>*'regressor__gamma': 'scale'}* |
| XGBoost | *{'regressor__learning_rate': 0.1,*<br>*'regressor__max_depth': 7,*<br>*'regressor__n_estimators': 50,*<br>*'regressor__subsample': 1.0}* |
| RF | *{'regressor__max_depth': 20,*<br>*'regressor__min_samples_split': 5,*<br>*'regressor__n_estimators': 500}* |
| MLP | *{'layers': [input (N=14) → 256 ($n_1$) → 128 ($n_2$) → 64 ($n_3$) → 1],*<br>*'activation': ReLU,*<br>*'batch_norm': True,*<br>*'dropout': 0.1,*<br>*'optimizer': AdamW,*<br>*'learning_rate': 0.0005,*<br>*'weight_decay': 1e-4,*<br>*'loss': Huber(delta=10),*<br>*'batch_size': 64,*<br>*'epochs': 150}* |

**Table S6.** Optimized hyperparameters for OMI Model. Final tuned hyperparameter values for each machine learning model trained for OMI model of the multi-model framework.

| **Model** | **Optimized hyperparameters** |
|---|---|
| LASSO | *{'regressor__alpha': 0.01}* |
| SVM | *{'regressor__C': 100,*<br>*'regressor__epsilon': 0.2,*<br>*'regressor__gamma': 0.1}* |
| XGBoost | *{'regressor__learning_rate': 0.1,*<br>*'regressor__max_depth': 7,*<br>*'regressor__n_estimators': 50,*<br>*'regressor__subsample': 1.0}* |
| RF | *{'regressor__max_depth': 20,*<br>*'regressor__min_samples_split': 5,*<br>*'regressor__n_estimators': 500}* |
| MLP | *{'layers': [input (N=14) → 256 ($n_1$) → 128 ($n_2$) → 64 ($n_3$) → 1],*<br>*'activation': ReLU,*<br>*'batch_norm': True,*<br>*'dropout': 0.1,*<br>*'optimizer': AdamW,*<br>*'learning_rate': 0.0005,*<br>*'weight_decay': 1e-4,*<br>*'loss': Huber(delta=10),*<br>*'batch_size': 64,*<br>*'epochs': 150}* |

**Table S7.** Optimized hyperparameters for MERRA model. Final tuned hyperparameter values for each machine learning model trained for MERRA model of the multi-model framework.

| **Model** | **Optimized hyperparameters** |
|---|---|
| LASSO | *{'regressor__alpha': 0.001}* |
| SVM | *{'regressor__C': 100,*<br>*'regressor__epsilon': 0.2,*<br>*'regressor__gamma': 0.1}* |
| XGBoost | *{'regressor__learning_rate': 0.1,*<br>*'regressor__max_depth': 7,*<br>*'regressor__n_estimators': 50,*<br>*'regressor__subsample': 1.0}* |
| RF | *{'regressor__max_depth': 20,*<br>*'regressor__min_samples_split': 5,*<br>*'regressor__n_estimators': 500}* |
| MLP | *{'layers': [input (N=14) → 256 ($n_1$) → 128 ($n_2$) → 64 ($n_3$) → 1],*<br>*'activation': ReLU,*<br>*'batch_norm': True,*<br>*'dropout': 0.1,*<br>*'optimizer': AdamW,*<br>*'learning_rate': 0.0005,*<br>*'weight_decay': 1e-4,*<br>*'loss': Huber(delta=10),*<br>*'batch_size': 64,*<br>*'epochs': 150}* |

**Table S8.** Performance metrics for TROPOMI Model. Performance comparison of machine learning models for $PM_{2.5}$ prediction under random, temporal, and spatial cross-validation schemes. Model performance is evaluated using coefficient of determination ($R^2$), Pearson correlation (r), bias, root mean squared error (RMSE), and mean absolute error (MAE). Normalized RMSE (nRMSE) and normalized MAE (nMAE) are reported in parentheses. Temporal cross-validation evaluates model generalization across years, while spatial cross-validation assesses transferability across locations. RMSE, MAE and bias are expressed in $\mu g\ m^{-3}$.

| Model | Random CV | | | | Temporal CV | | | | Spatial CV | | | |
|---|---|---|---|---|---|---|---|---|---|---|---|---|
| | $R^2$ (r) | Bias | RMSE (nRMSE) | MAE (nMAE) | $R^2$ (r) | Bias | RMSE (nRMSE) | MAE (nMAE) | $R^2$ (r) | Bias | RMSE (nRMSE) | MAE (nMAE) |
| LASSO | 0.60 (0.78) | -0.17 | 15.0 (0.48) | 9.7 (0.31) | 0.56 (0.75) | 0.33 | 15.7 (0.50) | 10.3 (0.33) | 0.45 (0.68) | 2.96 | 19.8 (0.57) | 13.8 (0.39) |
| SVM | 0.69 (0.83) | -1.55 | 13.2 (0.42) | 7.8 (0.25) | 0.55 (0.77) | -0.36 | 15.8 (0.50) | 9.8 (0.31) | 0.52 (0.75) | -5.91 | 19.4 (0.55) | 13.3 (0.38) |
| RF | 0.71 (0.85) | 0.09 | 12.7 (0.40) | 7.6 (0.24) | 0.55 (0.77) | 0.77 | 15.9 (0.50) | 10.1 (0.32) | 0.56 (0.76) | -1.52 | 18.4 (0.53) | 13.1 (0.37) |
| **XGB*** | 0.72 (0.86) | -0.01 | 12.5 (0.40) | 7.3 (0.23) | 0.57 (0.78) | 0.66 | 15.6 (0.49) | 9.6 (0.30) | 0.57 (0.76) | -0.93 | 17.3 (0.49) | 10.4 (0.33) |
| MLP | 0.71 (0.84) | -0.12 | 12.8 (0.40) | 7.8 (0.25) | 0.54 (0.76) | -1.56 | 16.0 (0.51) | 10.4 (0.33) | 0.42 (0.66) | -2.75 | 18.7 (0.54) | 13.5 (0.38) |

**Table S9.** Performance metrics for OMI Model. Performance comparison of machine learning models for $PM_{2.5}$ prediction under random, temporal, and spatial cross-validation schemes. Model performance is evaluated using coefficient of determination ($R^2$), Pearson correlation (r), bias, root mean squared error (RMSE), and mean absolute error (MAE). Normalized RMSE (nRMSE) and normalized MAE (nMAE) are reported in parentheses. Temporal cross-validation evaluates model generalization across years, while spatial cross-validation assesses transferability across locations. RMSE, MAE and bias are expressed in $\mu g\ m^{-3}$.

| Model | Random CV | | | | Temporal CV | | | | Spatial CV | | | |
|---|---|---|---|---|---|---|---|---|---|---|---|---|
| | $R^2$ (r) | Bias | RMSE (nRMSE) | MAE (nMAE) | $R^2$ (r) | Bias | RMSE (nRMSE) | MAE (nMAE) | $R^2$ (r) | Bias | RMSE (nRMSE) | MAE (nMAE) |
| LASSO | 0.58 (0.76) | -0.19 | 15.4 (0.49) | 10.2 (0.32) | 0.53 (0.73) | 0.35 | 16.3 (0.52) | 10.9 (0.35) | 0.38 (0.64) | -4.19 | 21.7 (0.59) | 14.1 (0.41) |
| SVM | 0.68 (0.83) | -1.79 | 13.4 (0.42) | 7.8 (0.25) | 0.52 (0.75) | -1.31 | 16.4 (0.52) | 10.0 (0.32) | 0.48 (0.73) | -5.55 | 20.2 (0.57) | 13.9 (0.40) |
| RF | 0.71 (0.84) | -0.16 | 13.0 (0.41) | 7.9 (0.25) | 0.53 (0.75) | 1.46 | 16.3 (0.52) | 10.3 (0.33) | 0.48 (0.75) | -1.53 | 19.3 (0.55) | 13.6 (0.39) |
| **XGB*** | 0.72 (0.85) | .04 | 12.8 (0.41) | 7.7 (0.24) | 0.56 (0.76) | 0.75 | 15.6 (0.50) | 9.6 (0.31) | 0.54 (0.75) | -1.01 | 18.9 (0.54) | 13.5 (0.38) |
| MLP | 0.70 (0.83) | -1.19 | 13.3 (0.42) | 8.1 (0.26) | 0.50 (0.71) | 1.78 | 16.6 (0.53) | 10.6 (0.34) | 0.46 (0.70) | -1.83 | 19.8 (0.57) | 15.5 (0.48) |

**Table S10.** Performance metrics for MERRA-2 model. Performance comparison of machine learning models for $PM_{2.5}$ prediction under random, temporal, and spatial cross-validation schemes. Model performance is evaluated using coefficient of determination ($R^2$), Pearson correlation (r), bias, root mean squared error (RMSE), and mean absolute error (MAE). Normalized RMSE (nRMSE) and normalized MAE (nMAE) are reported in parentheses. Temporal cross-validation evaluates model generalization across years, while spatial cross-validation assesses transferability across locations. RMSE, MAE and bias are expressed in $\mu g\ m^{-3}$.

| Model | Random CV | | | | Temporal CV | | | | Spatial CV | | | |
|---|---|---|---|---|---|---|---|---|---|---|---|---|
| | $R^2$ (r) | Bias | RMSE (nRMSE) | MAE (nMAE) | $R^2$ (r) | Bias | RMSE (nRMSE) | MAE (nMAE) | $R^2$ (r) | Bias | RMSE (nRMSE) | MAE (nMAE) |
| LASSO | 0.63 (0.79) | -0.19 | 14.5 (0.46) | 9.1 (0.29) | 0.58 (0.75) | -0.06 | 15.2 (0.48) | 9.6 (0.30) | 0.41 (0.67) | -4.63 | 18.2 (0.57) | 12.0 (0.38) |
| SVM | 0.70 (0.83) | -1.68 | 12.7 (0.41) | 7.6 (0.25) | 0.55 (0.76) | -1.17 | 15.9 (0.50) | 9.6 (0.30) | 0.37 (0.66) | 5.60 | 19.0 (0.60) | 11.9 (0.37) |
| RF | 0.71 (0.84) | 0.38 | 12.6 (0.40) | 7.5 (0.24) | 0.51 (0.75) | 1.37 | 16.6 (0.53) | 10.4 (0.33) | 0.47 (0.70) | 2.16 | 17.2 (0.54) | 10.8 (0.34) |
| **XGB*** | 0.72 (0.85) | -0.18 | 12.6 (0.40) | 7.2 (0.23) | 0.59 (0.78) | 0.03 | 15.2 (0.48) | 9.2 (0.29) | 0.49 (0.73) | 0.39 | 16.8 (0.50) | 10.1 (0.32) |
| MLP | 0.70 (0.83) | 1.03 | 12.9 (0.42) | 7.8 (0.26) | 0.55 (0.74) | 1.92 | 16.0 (0.51) | 9.8 (0.31) | 0.44 (0.69) | -1.54 | 18.0 (0.55) | 11.2 (0.35) |

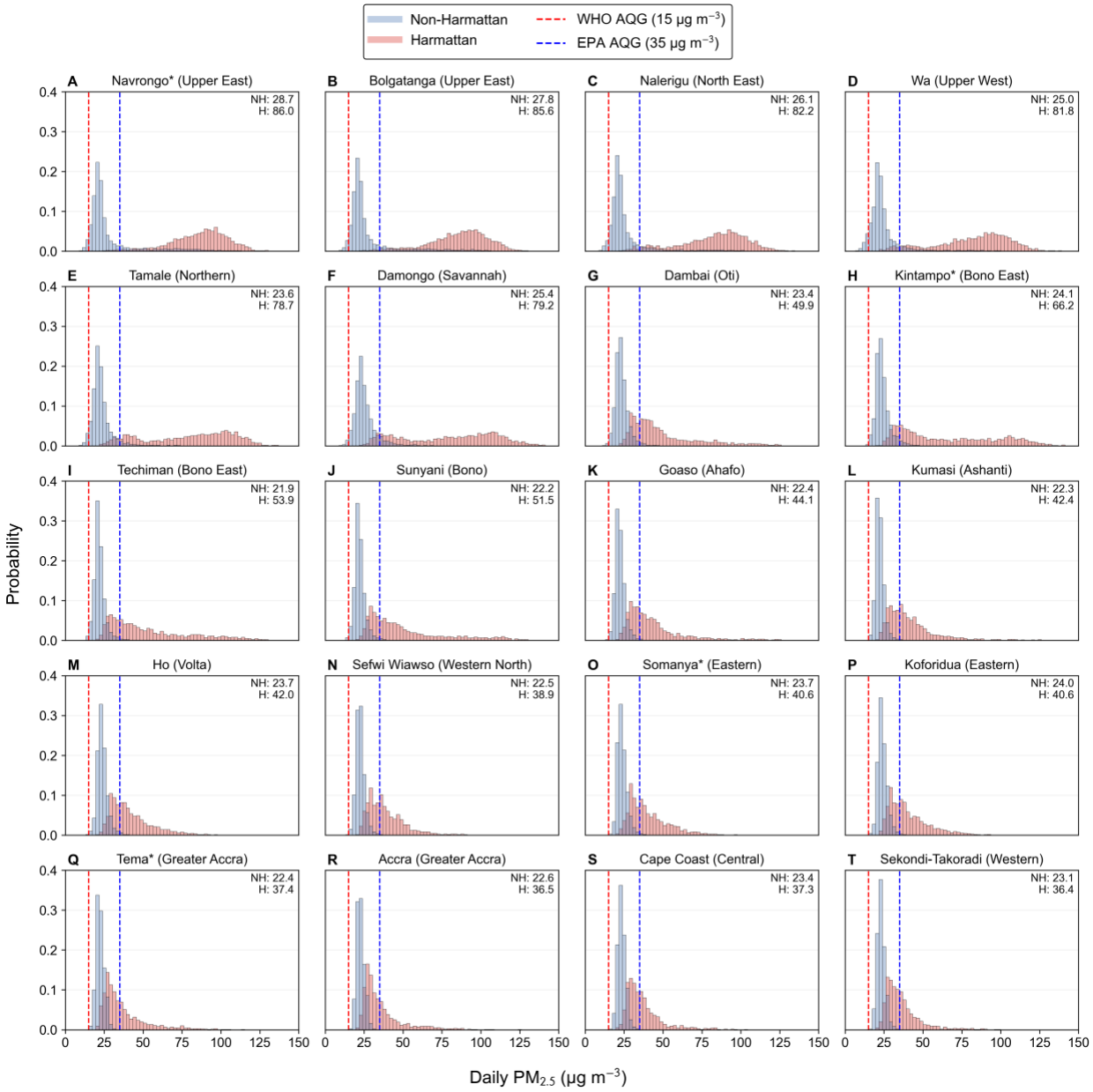


**Fig. S9.** Distribution of $PM_{2.5}$ concentrations between 2005–2025. (A–T) City-level probability distributions of daily $PM_{2.5}$ concentrations across Ghana during Harmattan and non-Harmattan periods (2005–2025). Panels show histograms of daily mean $PM_{2.5}$ concentrations for each regional capital, arranged geographically from north (top-left) to south (bottom-right). Blue bars represent non-Harmattan conditions, while red bars represent Harmattan conditions (mid-November to mid-March). Average $PM_{2.5}$ (in μg $m^{-3}$) for both periods are denoted as NH and H for non-Harmattan and Harmattan periods. The red and blue dashed vertical lines indicate the 24-hour air quality guidelines from WHO (15 μg $m^{-3}$) and Ghana EPA (35 μg $m^{-3}$), highlighting extremely high number of exceedances, particularly during Harmattan months. Overall, the figure highlights a pronounced north–south gradient in particulate pollution and demonstrates the dominant role of Harmattan dust in shaping seasonal air quality patterns across Ghana.

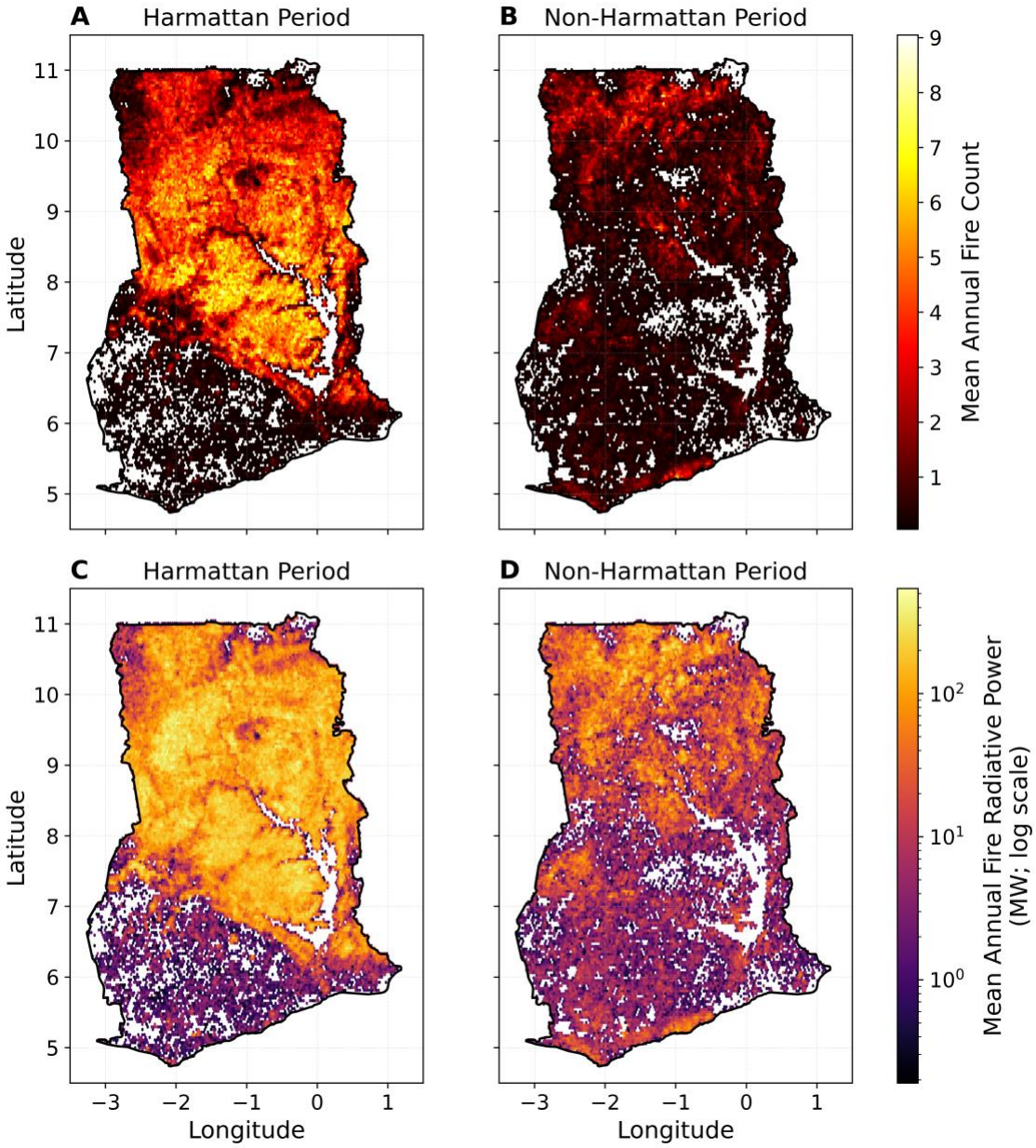


**Fig. S10.** Spatial distribution of fire activity across Ghana during Harmattan and non-Harmattan seasons (2005–2025). (A–B) Fire detection counts derived from MODIS MCD14ML active fire daily observations aggregated over a 21-year period. (C–D) Corresponding cumulative fire radiative power (FRP), indicating the spatial distribution of fire intensity in megawatts. Harmattan-season fires (December–February; A, C) are concentrated across the northern and middle savanna regions of Ghana, reflecting widespread biomass burning associated with seasonal land management practices and dry atmospheric conditions. In contrast, non-Harmattan fires (March–November; B, D) occur less frequently and are more spatially heterogeneous, with localized hotspots observed across both northern and southern regions. Log-transformed cumulative FRP highlights persistently higher fire intensity across northern Ghana relative to southern forested and coastal zones. All maps include only fire detections with confidence ≥30%.

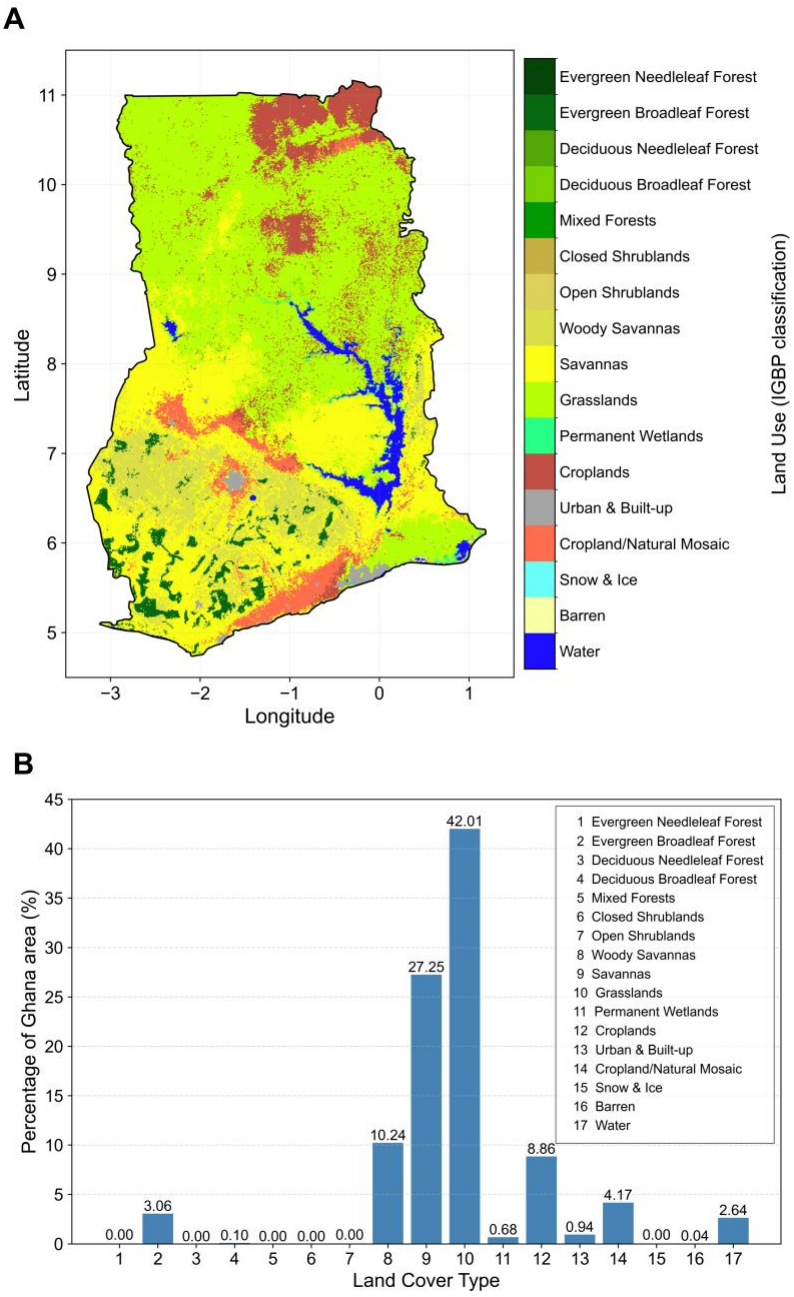


**Fig. S11.** Land cover distribution across Ghana in 2024. (A) Annual spatial distribution of land cover classes derived from the MCD12Q1 Version 6.1 MODIS Land Cover Type product (International Geosphere–Biosphere Programme, IGBP classification). The original 500 m sinusoidal grid product was regridded to 1 km resolution for Ghana. Savannas and grasslands dominate northern and central Ghana, while croplands and cropland–natural vegetation mosaics are prevalent in southern and transitional zones. Water bodies correspond primarily to Lake Volta and major river systems. (B) Fractional area coverage of each IGBP land cover class within Ghana. Grasslands (42.01%), Savannas (27.25%), woody savannas (10.24%), and croplands (8.86%) represent the dominant land cover types, together accounting for more than 85% of national land area. Only 0.94% of Ghana's land is classified as urban.

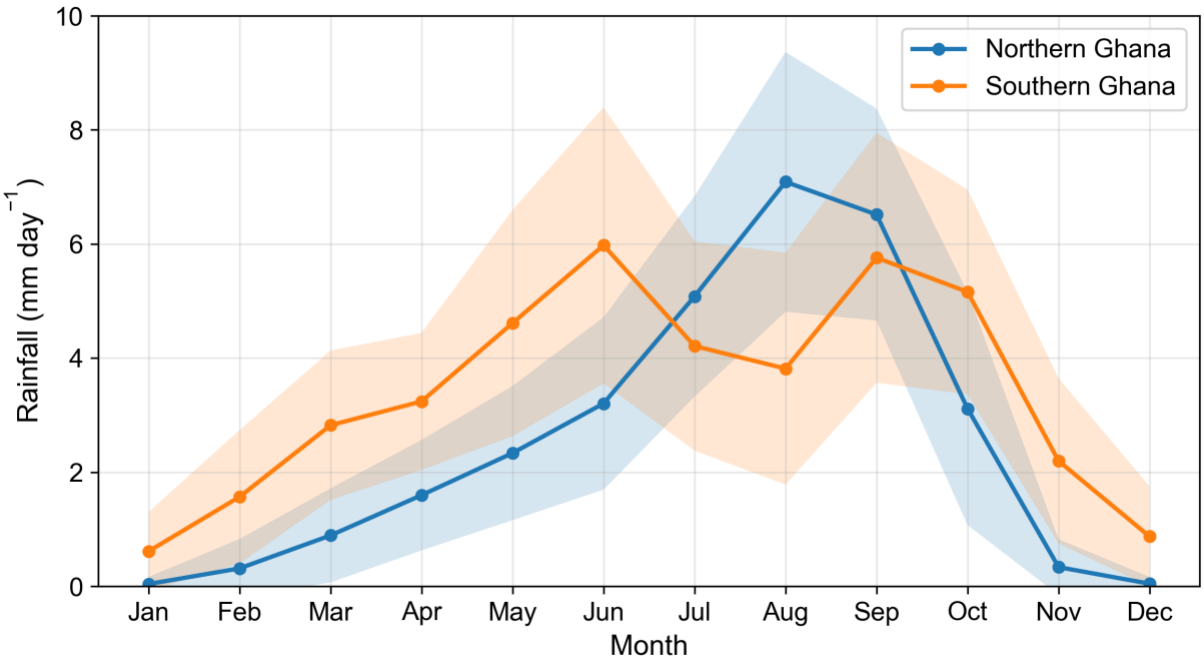


**Fig. S12.** Monthly rainfall climatology for Northern and Southern Ghana (2005–2025). Lines show the long-term mean daily rainfall for each calendar month derived from ERA5 data, averaged over 2005–2025. Shaded regions represent ±1 standard deviation, indicating interannual variability. Southern Ghana exhibits a bimodal rainfall regime with peaks in May–June (major wet season) and September–October (minor wet season). In contrast, Northern Ghana shows a unimodal rainfall pattern peaking during August–September, a typical characteristic of the West African monsoon.

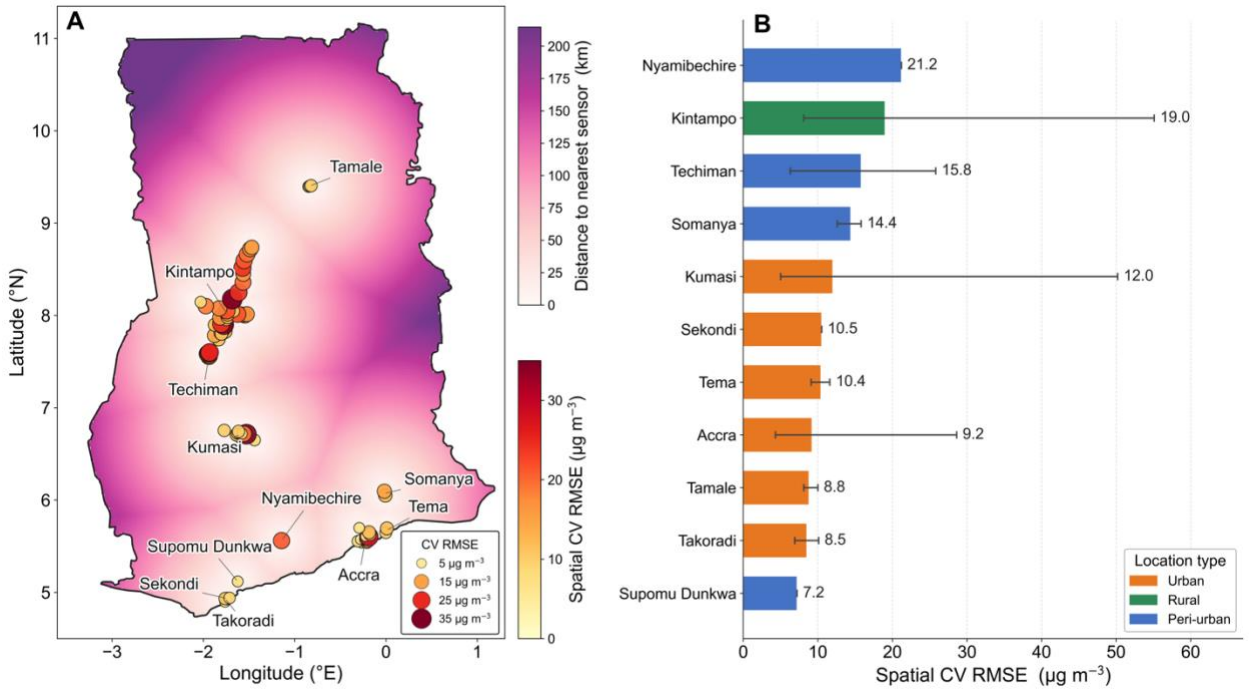


**Fig. S13.** Spatial uncertainty assessment of the $PM_{2.5}$ model across Ghana. (A) Background color shows the distance to the nearest ground monitoring site, where darker regions indicate areas farther from sensor locations. Circles represent leave-one-site-out cross-validation (CV) RMSE at individual sensor locations, with circle size and color intensity proportional to RMSE magnitude. (B) Mean spatial CV RMSE by city, with horizontal whiskers indicating the full range across monitoring sites within each location. Bar colors denote site classification (urban, peri-urban, and rural). Overall, most monitoring locations exhibit CV RMSE values below 20 µg $m^{-3}$.

**Text S2. Estimation of long-term $PM_{2.5}$ Trends**

Long-term trends in $PM_{2.5}$ concentrations were estimated at each grid cell using a non-parametric trend analysis approach applied to the annual mean $PM_{2.5}$ time series for the period 2005–2025. First, annual mean $PM_{2.5}$ concentrations were calculated from the gridded daily $PM_{2.5}$ dataset for each year. The magnitude of the temporal trend was then quantified using Sen's slope estimator, which computes the median of all pairwise slopes between observations in the time series and is robust to outliers and non-normal data distributions. Statistical significance of the monotonic trend was evaluated using the Mann–Kendall test, a rank-based method commonly used for environmental time series that does not assume linearity or normality. Grid cells with a Mann–Kendall *p*-value less than 0.05 were considered to exhibit statistically significant trends and are highlighted in the figure using stippling. This approach provides a robust assessment of spatial patterns in long-term changes in $PM_{2.5}$ concentrations across Ghana over the study period.

**Table S11.** Annual and seasonal long-term trends in $PM_{2.5}$ concentrations across Ghanaian locations. *Slope* is the Sen's slope estimates ($\mu g\ m^{-3}\ yr^{-1}$), representing the magnitude and direction of monotonic trends derived using monthly $PM_{2.5}$ data (2005–2025). *p–value* is derived from the non-parametric Mann–Kendall significance test. Trends with p-values < 0.05 are considered statistically significant and are indicated with an asterisk (*). Non-regional capitals are denoted with a hash (#).

| Location | Annual | | Harmattan | | Non-Harmattan | |
|---|---|---|---|---|---|---|
| | Slope | p–value | Slope | p–value | Slope | p–value |
| Navrongo# | 0.003 | 0.206 | -0.057 | 0.007* | 0.011 | 0* |
| Bolgatanga | 0.001 | 0.308 | -0.051 | 0.026* | 0.007 | 0.001* |
| Nalerigu | 0.004 | 0.003* | -0.031 | 0.474 | 0.011 | 0* |
| Wa | 0.008 | 0* | -0.028 | 0.903 | 0.018 | 0* |
| Tamale | 0.006 | 0.001* | 0.008 | 0.395 | 0.01 | 0* |
| Damongo | 0.004 | 0.002* | 0.037 | 0.061 | 0.006 | 0.013* |
| Dambai | 0.001 | 0.469 | 0.016 | 0.262 | 0.001 | 1 |
| Kintampo# | 0.002 | 0.127 | 0.038 | 0.173 | 0.003 | 0.405 |
| Techiman | 0.003 | 0.001* | 0.05 | 0.039* | 0.004 | 0.008* |
| Sunyani | 0.002 | 0.002* | 0.033 | 0.05* | 0.003 | 0.021* |
| Goaso | 0 | 0.166 | 0.017 | 0.19 | 0.001 | 0.486 |
| Kumasi | -0.002 | 0.253 | -0.008 | 0.925 | -0.003 | 0.16 |
| Ho | -0.007 | 0* | -0.01 | 0.251 | -0.011 | 0* |
| Sefwi Wiawso | -0.001 | 0.841 | 0.007 | 0.338 | -0.002 | 0.278 |
| Somanya# | -0.009 | 0* | -0.018 | 0.047* | -0.014 | 0* |
| Koforidua | -0.007 | 0* | -0.003 | 0.636 | -0.013 | 0* |
| Tema# | -0.003 | 0.003* | -0.004 | 0.24 | -0.004 | 0.004* |
| Accra | -0.002 | 0.16 | 0.004 | 0.925 | -0.003 | 0.054 |
| Cape Coast | -0.003 | 0.001* | -0.011 | 0.077 | -0.005 | 0.004* |
| Sekondi-Takoradi | -0.003 | 0.003* | -0.011 | 0.148 | -0.005 | 0.008* |

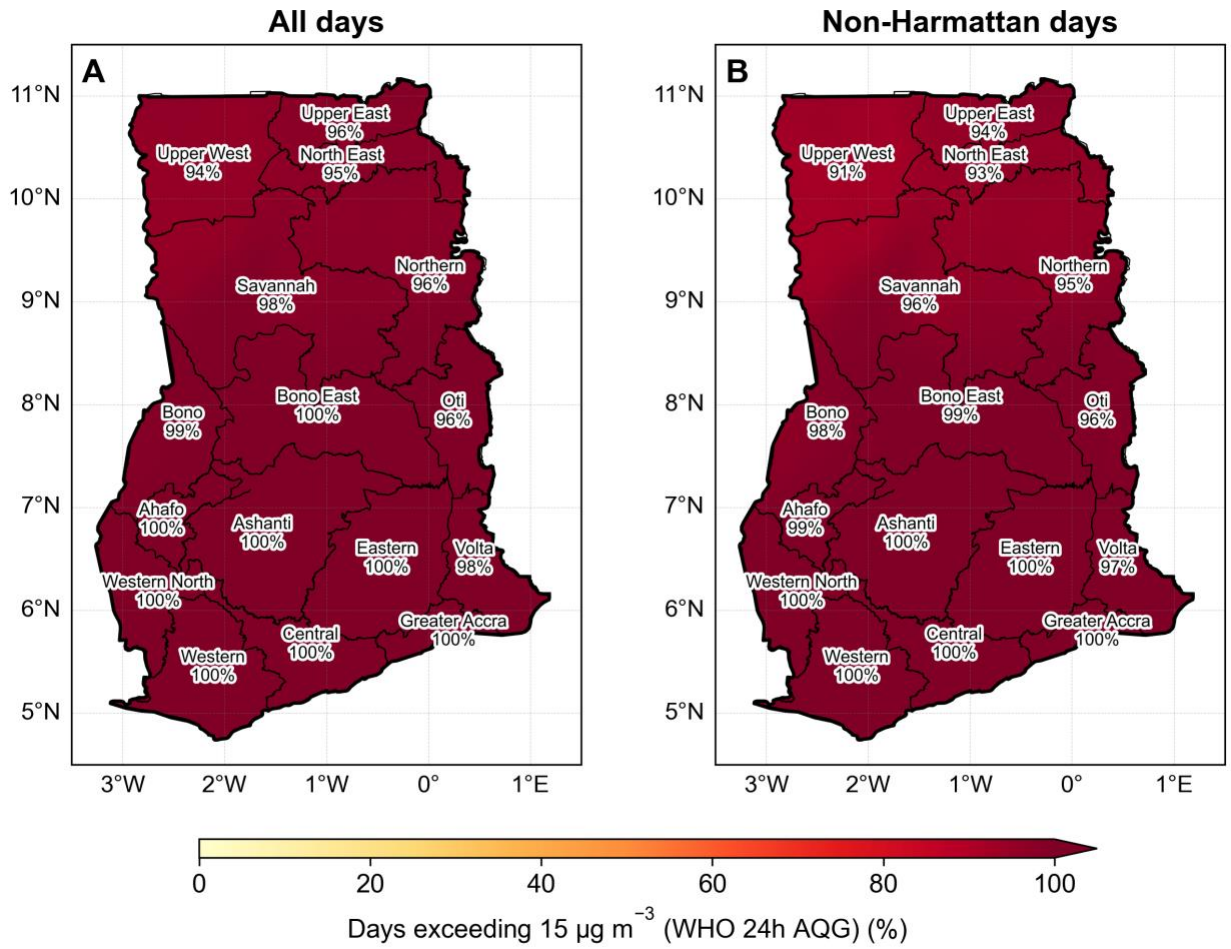


**Fig. S14.** Spatial distribution of the percentage of days exceeding the WHO 24-hour $PM_{2.5}$ guideline. Maps show the percentage of days during 2005–2025 in which daily $PM_{2.5}$ concentrations exceeded the WHO 24-hour air quality guideline (15 µg $m^{-3}$) across Ghana, calculated using (a) all available days and (b) non-Harmattan days. Values represent the proportion of days (%) at each grid cell exceeding the guideline threshold.

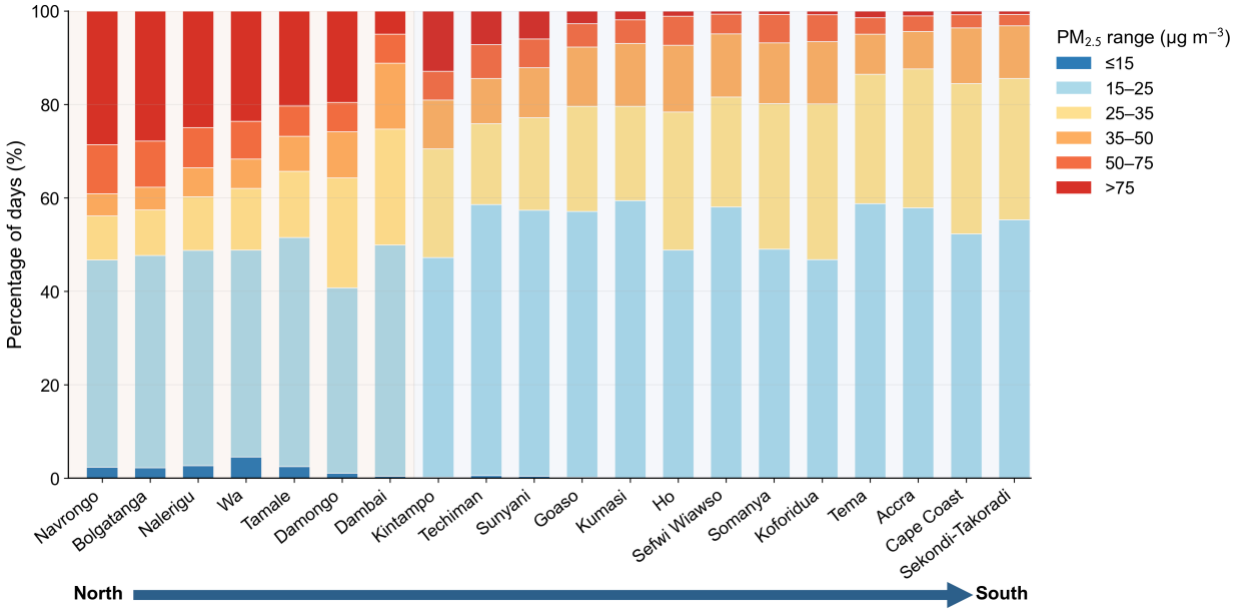


**Fig. S15.** Distribution of daily $PM_{2.5}$ concentrations across WHO air quality guideline (AQG) categories. Stacked bars show the percentage of days within each concentration range (≤15, 15–25, 25–35, 35–50, 50–75, and >75 µg $m^{-3}$) for locations across Ghana (2005–2025). Cities are ordered geographically from north (left) to south (right) to highlight spatial gradients in air quality.

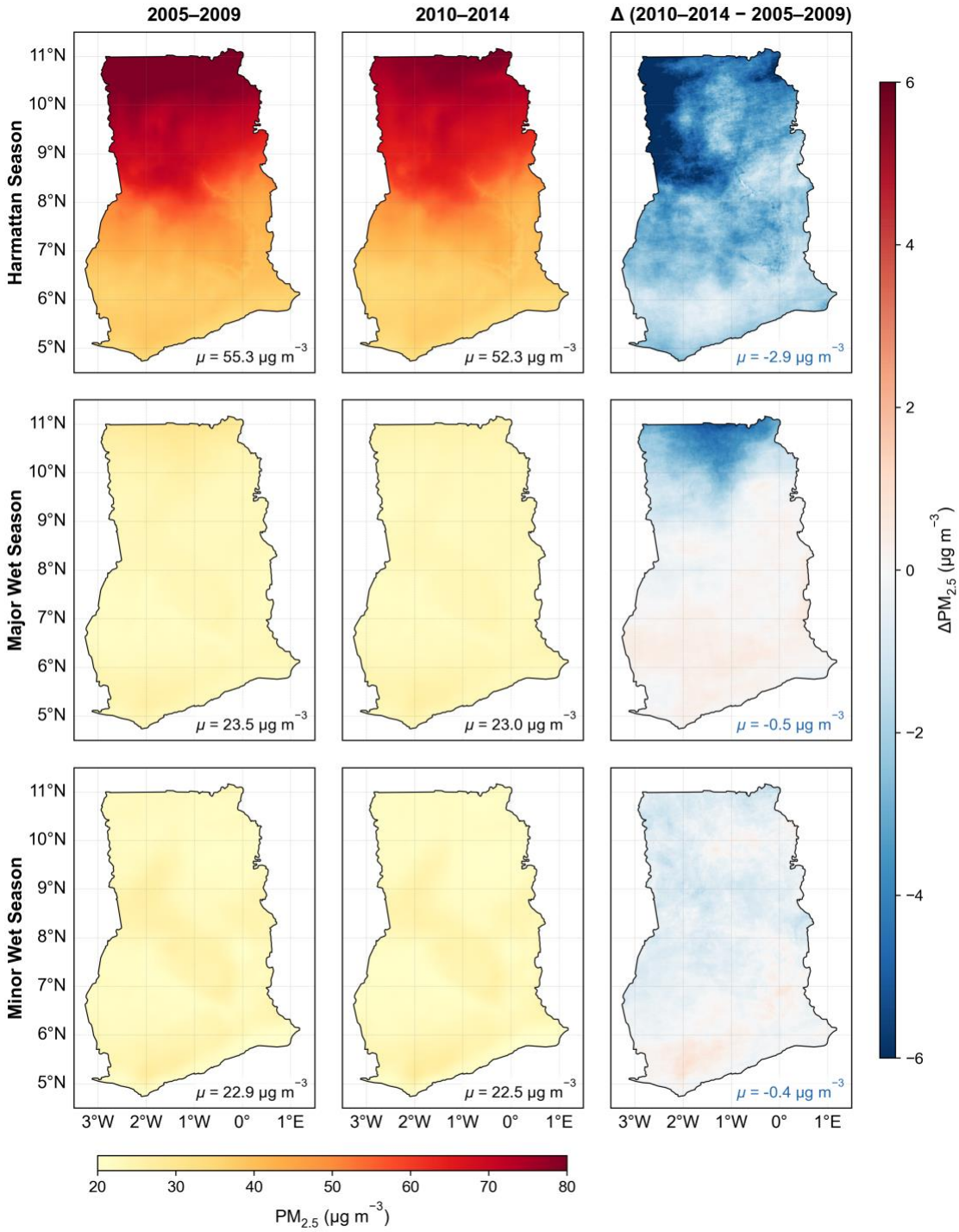


**Fig. S16.** Multi-year changes in seasonal mean $PM_{2.5}$ concentrations across Ghana (2005-2014). Maps show spatial patterns of mean $PM_{2.5}$ concentrations for the Harmattan, major wet, and minor wet seasons for two multi-year periods (2005–2009 and 2010–2014), along with the corresponding differences (Δ = 2010–2014 minus 2005–2009). μ denotes the spatial mean concentration for each panel. The color scale for mean concentration levels is shown at the bottom, while the diverging color scale on the right indicates the difference.

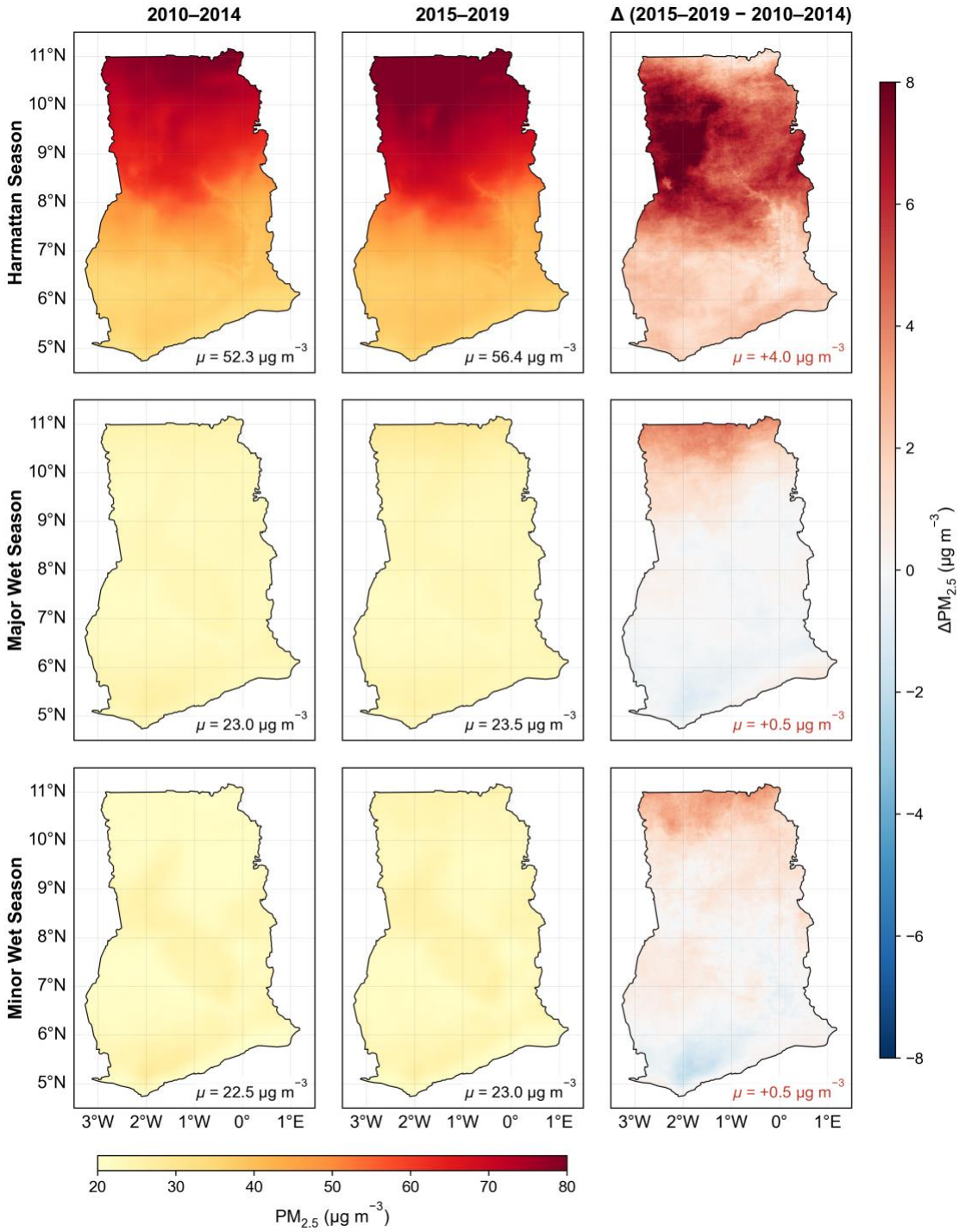


**Fig. S17.** Multi-year changes in seasonal mean $PM_{2.5}$ concentrations across Ghana (2010-2019). Maps show spatial patterns of mean $PM_{2.5}$ concentrations for the Harmattan, major wet, and minor wet seasons for two multi-year periods (2010–2014 and 2015–2019), along with the corresponding differences (Δ = 2015-2019 minus 2010–2014). μ denotes the spatial mean concentration for each panel. The color scale for mean concentration levels is shown at the bottom, while the diverging color scale on the right indicates the difference.

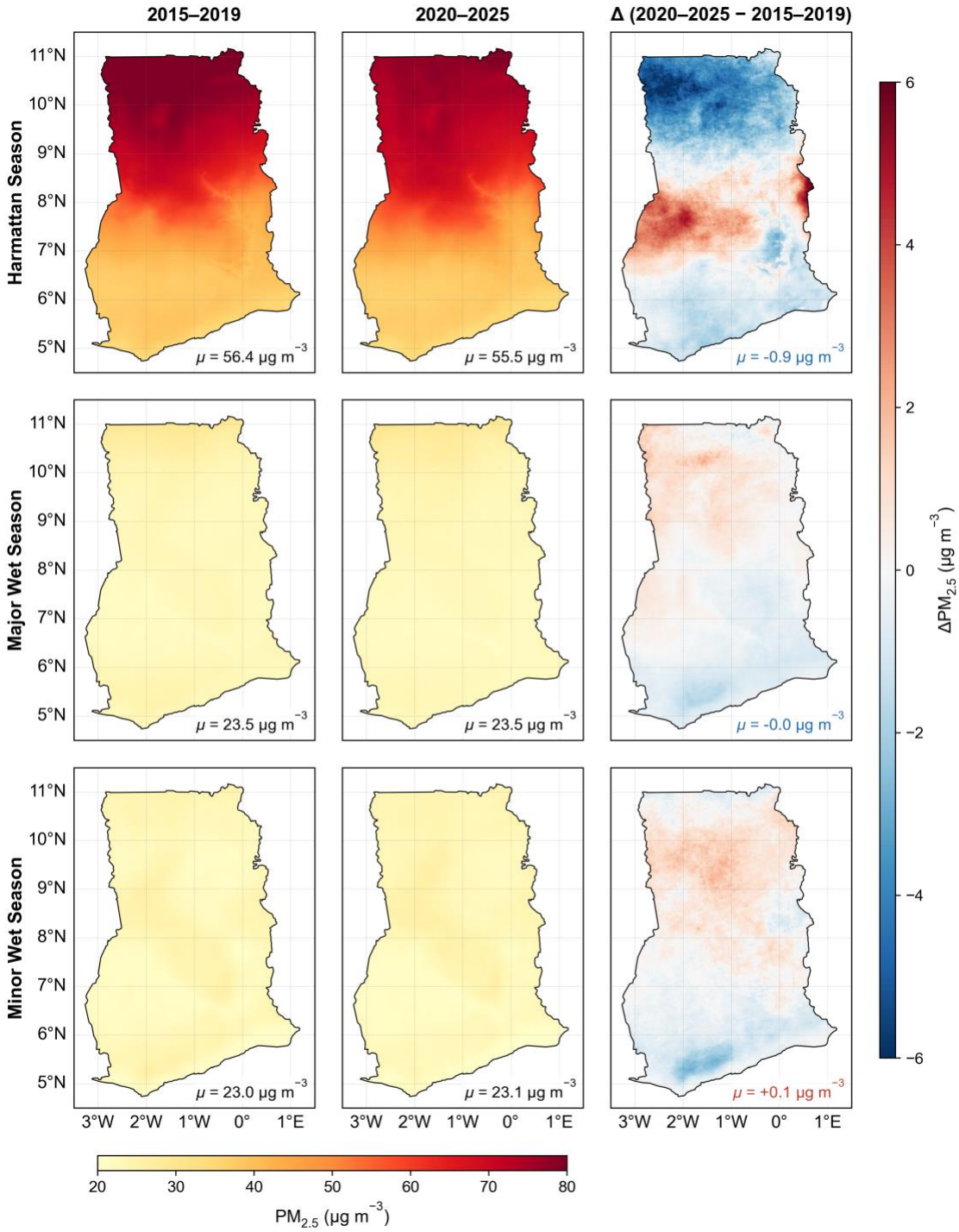


**Fig. S18.** Multi-year changes in seasonal mean $PM_{2.5}$ concentrations across Ghana (2015-2025). Maps show spatial patterns of mean $PM_{2.5}$ concentrations for the Harmattan, major wet, and minor wet seasons for two multi-year periods (2015–2019 and 2020–2025), along with the corresponding differences (Δ = 2020-2025 minus 2015–2019). μ denotes the spatial mean concentration for each panel. The color scale for mean concentration levels is shown at the bottom, while the diverging color scale on the right indicates the difference.

## References

Lebakula, V., Sims, K., Reith, A., Rose, A., McKee, J., Coleman, P., Kaufman, J., Urban, M., Jochem, C., Whitlock, C., Ogden, M., Pyle, J., Roddy, D., Epting, J., Bright, E., 2025. LandScan Global 30 Arcsecond Annual Global Gridded Population Datasets from 2000 to 2022. Scientific Data 2025 12:1 12, 495-. https://doi.org/10.1038/s41597-025-04817-z

Owusu-Tawiah, V., Annor, T., Yamba, E.I., Nimo, J., Wemegah, C.S., Hodoli, C.G., Osei-Tutu, D., Amponsah, D., Hughes, A.F., Westervelt, D.M., 2025. Spatiotemporal Assessment of PM2.5 in Senior High Schools in Kumasi, Ghana using Low-Cost Sensors. Aerosol Air Qual. Res. 25, 66-. https://doi.org/10.1007/S44408-025-00066-2/FIGURES/9

Raheja, G., Nimo, J., Appoh, E.K.E., Essien, B., Sunu, M., Nyante, J., Amegah, M., Quansah, R., Arku, R.E., Penn, S.L., Giordano, M.R., Zheng, Z., Jack, D., Chillrud, S., Amegah, K., Subramanian, R., Pinder, R., Appah-Sampong, E., Tetteh, E.N., Borketey, M.A., Hughes, A.F., Westervelt, D.M., 2023. Low-Cost Sensor Performance Intercomparison, Correction Factor Development, and 2+ Years of Ambient PM2.5 Monitoring in Accra, Ghana. Environ. Sci. Technol. 57, 10708–10720. https://doi.org/10.1021/ACS.EST.2C09264